

INTEGRATING COPPER NANOWIRE ELECTRODES FOR LOW TEMPERATURE  
PEROVSKITE PHOTOVOLTAIC CELLS

By

Trent Mankowski

---

Copyright © Trent Mankowski

A Thesis Submitted to the Faculty of the

COLLEGE OF OPTICAL SCIENCES

In Partial Fulfillment of the Requirements

For the Degree of

MASTER OF SCIENCE

In the Graduate College

THE UNIVERSITY OF ARIZONA

2017

## STATEMENT BY THE AUTHOR

The thesis titled *Integrating Copper Nanowire Electrodes for Low Temperature Perovskite Photovoltaic Cells* has been submitted in partial fulfillment of requirements for a master's degree at the University of Arizona and is deposited in the University Library to be made available to borrowers under rules of the Library.

Brief quotations from this thesis are allowable without special permission, provided that an accurate acknowledgement of the source is made. Requests for permission for extended quotation from or reproduction of this manuscript in whole or in part may be granted by the head of the major department or Dean of the Graduate College when in his or her judgement the proposed use of the material is in the interests of the scholarship. In all other instances, however, permission must be obtained from the author.

Chapters 2-4 are direct extracts from collaborative publications with Zhaozhao Zhu and are also reported in his PhD dissertation titled *Emerging Materials for Transparent Conductive Electrodes and their Applications in Photovoltaics*.

SIGNED: Trent Mankowski

### APPROVAL BY THESIS DIRECTOR

This thesis has been approved on the date shown below:

050217

---

*Masud Mansuripur*  
*Professor of Optical Sciences*

*Date*

## ACKNOWLEDGEMENT

This work was made possible by the grant #5-546-2-222 from the Qatar National Research Fund (a member of the Qatar Foundation). I would like to thank Dr. Peyghambarian, Dr. Norwood and Dr. Fallahi for access to their facilities and instruments necessary to this research. Many thanks to the past and present researcher professors, post-docs and grad students of the Norwood research group for dialogues and training on tools and assistance with materials. Special thanks to Zhaozhao Zhu for his friendship, instruction and patience with me over the years which resulted in this work. Finally, this work would not be possible without the dedication, support, love and patience shown by my wife, Ashley.

# TABLE OF CONTENTS

STATEMENT BY THE AUTHOR.....	2
ACKNOWLEDGEMENT .....	3
TABLE OF CONTENTS.....	4
LIST OF FIGURES .....	8
LIST OF TABLES.....	12
ACRONYMS AND TERMINOLOGIES.....	13
ABSTRACT.....	14
Chapter 1 .....	16
INTRODUCTION .....	16
1.1 Industry Standard Transparent Conducting Electrodes .....	16
1.2 Alternative Transparent Conducting Electrodes.....	17
1.3 Dye Sensitized Solar Cells.....	19
1.4 Thin film photovoltaic technology.....	21
Chapter 2.....	24
Ultra-high aspect ratio copper-nanowire-based hybrid transparent conductive electrodes with PEDOT:PSS and reduced Graphene Oxide exhibiting reduced surface roughness and improved stability.....	24
2.1 INTRODUCTION .....	24
2.2 EXPERIMENTS .....	27

2.2.1 Nanowire synthesis .....	27
2.2.2 Fabrication of CuNW TCEs.....	28
2.3 RESULTS AND DISCUSSION.....	30
2.4 CONCLUSIONS.....	41
Chapter 3.....	42
Sol-gel deposited aluminum-doped and gallium-doped zinc oxide thin-film transparent conductive electrodes with a protective coating of reduced graphene oxide.....	42
3.1 Introduction.....	42
3.2 Methods.....	43
3.3 Results.....	44
3.4 Conclusion .....	49
Chapter 4.....	50
Hybrid transparent conductive electrodes with copper nanowires embedded in a zinc oxide matrix and protected by reduced graphene oxide platelets.....	50
4.1 Introduction.....	50
4.2 Methods.....	52
4.2.1 Fabrication of CuNW TCE.....	52
4.2.2 Sol-gel deposition of zinc oxide thin film.....	52
4.2.3 Deposition and reduction of graphene oxide (GO) platelets .....	53
4.2.4 Characterizations.....	53

4.3. Results and Discussions.....	53
4.3 Conclusion .....	59
Chapter 5.....	60
Perovskite Solar Cells.....	60
Perovskite Solar Cell synthesis and deposition .....	60
High temperature Perovskite Solar Cells for benchmark testing and troubleshooting.....	60
Low Temperature TiO <sub>2</sub> Perovskite Solar Cells .....	68
Low Temperature PEDOT:PSS Perovskite Solar Cells.....	68
Electron Transport Layer Free Perovskite Solar Cells .....	69
Low temperature ZnO electron transport layer.....	70
Chapter 6.....	72
INTEGRATING COPPER NANOWIRES INTO DEVICES.....	72
6.1 Introduction.....	72
6.2 Methodology.....	72
Copper Nanowires as the front electrode.....	72
Temperature Requirements.....	72
Mechanical Stability .....	73
Chemical Stability.....	73
Surface Roughness.....	75
Copper Nanowires as the Back Electrode.....	75

6.3 Results and Discussion .....	76
Appendix A: Material Synthesis.....	87
A.1 Ni-coated CuNW thin Films .....	87
A.2 Two-Step PbI <sub>2</sub> Perovskite Precursor in DMF .....	87
A.3 PbI <sub>2</sub> :MAI Hybrid Perovskite Precursor in DMF.....	87
A.4 PbCl <sub>2</sub> :MAI One-Step Perovskite Precursor in DMF .....	88
A.5 TiO <sub>2</sub> electron transport layer synthesis .....	88
Appendix B: Solar Cell FABRICATION.....	89
B.1 High and Low Temperature Two-Step Planar Heterojunction Perovskite Solar Cell Deposition.....	89
B.2 Low temperature Inverted Planar Heterojunction Perovskite Solar Cell Deposition ....	90
B.3 Mesoporous Perovskite Solar Cell Deposition.....	90
B.4 Sandwiching back electrode configuration and why it doesn't work .....	91
Appendix C: Characterization Tools and Methods.....	92
C.1 Sheet Resistance Measurements.....	92
C.2 Absorption and optical transmittance measurements.....	92
C.3 X-Ray Diffraction .....	93
C.4 Scanning Electron Microscopy and Atomic Force Microscopy .....	93
C.5 Surface Roughness Measurements.....	93
References.....	94

## LIST OF FIGURES

Figure 1.1. Diagram of a basic DSSC (not to scale) illustrating the buildup of each layer sandwiched between two ITO electrodes. In a cell without spacers, the electrolyte is held in the cell by capillary action. .... 20

Figure 1.2. Research Cell Record Efficiency Chart provided by National Renewable Energy Laboratory (NREL).[45] Note the quick increase in emerging PV technologies compared to crystalline Si cells. .... 21

Figure 1.3. (from left) Evolution of perovskite solar cell from DSSC architecture. The mesoporous scaffolding layer is eventually removed in favor of a much thinner scaffold-free perovskite layer. .... 22

Figure 2.1. (a) Photograph of synthesized CuNWs in IPA suspension. (b) SEM image of synthesized CuNWs spray-coated onto a glass substrate; the nanowires are seen to be homogeneously distributed. (c) SEM image of a nanowire bundle shows the wires' fairly uniform diameter..... 30

Figure 2.2. 3D reconstructed AFM image showing the smoothness of the nanowire surface. .... 32

Figure 2.3. (a) Sheet resistance  $R_s$  versus annealing temperature in a forming-gas atmosphere for one hour. (b) Optical transmittance  $T_{550}$  versus sheet resistance  $R_s$  for thermal annealing in forming-gas (red), and for plasma cleaning (black). (c-f) AFM images and line height profiles of un-annealed and annealed nanowire junctions. .... 32

Figure 2.4. Schematic depiction of the transfer process for spray-coated CuNWs to a spin-coated PEDOT:PSS film using the “flip and press” method. The photographs below the diagram show, from left to right, (i) CuNWs on a glass substrate, (ii) PEDOT:PSS film on a PET substrate, and (iii) hybrid TCE on a PET substrate. In each case, the OSC and QU logos are placed beneath the substrate in order to allow visual comparison of the samples' transparencies. .... 34

Figure 2.5. (a) Cross sectional SEM view of CuNWs transferred to a bare PET substrate, showing numerous nanowires sticking out of the plane of the substrate; (b) Cross sectional SEM view of CuNWs transferred to a spin-coated PEDOT:PSS film atop a PET substrate; hardly any nanowires are seen to be sticking out of the plane in this case. (c) Angled SEM image of spray-coated CuNWs on a glass substrate; (d) Angled SEM image of CuNWs transferred onto a thin film of PEDOT:PSS atop a PET substrate. (e) Surface profiles of spray-coated CuNWs on a glass substrate; and (f) Surface profiles of PEDOT:PSS/CuNW thin film exhibiting substantially reduced roughness. Different colors represent different scans. .... 36

Figure 2.6. (a) Optical transmittance spectrum and haze of a PEDOT:PSS/CuNW sample on a PET substrate. The inset shows a photograph of the corresponding sample placed over OSC and QU logos. (b) Sheet resistance versus the number of bending cycles of a typical PEDOT:PSS/CuNW film on PET substrate (bending radius ~5 cm). .... 36

Figure 2.7. (a) Raman spectroscopy of GO and rGO thin films. (b) SEM image of CuNWs buried under homogeneous rGO overcoating. Small cracks are observed in the marked red circle. (c) Optical transmittance at 550 nm versus the sheet resistance of samples of bare CuNW (red) and rGO-covered CuNW (blue), both on glass substrates. (d) SEM image of CuNWs spray-coated over one or more layers of rGO platelets. .... 39

Figure 2.8. (a) Optical transmittance spectra and haze of rGO thin film (black) CuNW (red) and CuNW/rGO (blue) on glass substrates. The inset shows photographs of the corresponding samples placed over OSC logos. (b) Durability test of CuNW (red) and rGO-coated CuNW (blue) TCEs under with 80% relative humidity at 80 °C temperature. (c) Durability test of CuNW (red) and rGO-covered CuNW (blue) TCEs under ambient conditions over the course of 30 days..... 40

Table 2.1. Performance evaluation of our TCEs compared to those reported in the literature. ... 40

Figure 2.9. Optical transmittance versus sheet resistance of all TCEs fabricated in the present work. The three lines represent  $\sigma_{DC}/\sigma_{op}$  values of 35, 100, 220 as shown..... 41

Table 3.1. Parameters of sol-gel deposited AZO and GZO thin films ..... 44

Figure 3.1. SEM images of (a) AZO and (b) GZO films before plasma treatment; the corresponding images after plasma treatment are shown in (c) and (d). ..... 45

Figure 3.2. Optical transmittance spectra of sol-gel-deposited and plasma-treated thin film TCEs across the visible and near-infrared range of wavelengths. (a) Transmittance spectra of AZO and passivated AZO/rGO samples fabricated on glass substrates; the inset shows photographs of both samples placed over the OSC logo. (b) Transmittance spectra of GZO and passivated GZO/rGO samples fabricated on glass substrates; the inset shows photographs of both samples placed over the OSC logo..... 46

Figure 3.3. (a) Normalized sheet resistance versus the time (in days) during which the samples were exposed to 50% relative humidity at room temperature. (b) Normalized sheet resistance versus the time (in hours) during which the samples were exposed to 80% relative humidity at 80 °C. .... 48

Figure 3.4. SEM images of: (a) An rGO layer fully covering an AZO thin film sample. (b) An rGO layer partially covering an AZO thin film sample. (c) An rGO layer fully covering a GZO thin film sample. (d) An rGO layer partially covering the lower-right half of a GZO thin film sample..... 48

Figure 4.1. (a) Optical transmittance (at the wavelength of 550 nm) versus the sheet resistance for CuNW samples fabricated on glass substrates, on PEN substrates, and on glass substrates while embedded in ZnO. (b) Sheet resistance versus number of bending cycles of CuNW and CuNW/ZnO samples on PEN substrates. The inset is a photograph of a flexible sample of a CuNW TCE on PEN held over the OSC logo..... 54

Figure 4.2. (a) Photographs of bare CuNW and CuNW/rGO samples before and after a scotch-tape-peel test; yellow boxes indicate the taped areas. (b) Sheet resistance of CuNW/ZnO samples on rigid glass substrates and also on flexible plastic (PEN) substrates versus the number of scotch-tape-peel tests. The embedding of the nanowire network within the ZnO matrix clearly improves the adhesion of CuNWs to the glass substrate. .... 55

Figure 4.3. SEM images of bare CuNW and hybrid CuNW/ZnO thin films on glass substrates. (a) Frontal view of a bare CuNW sample. (b) Edge view (at 5° grazing angle) of the bare CuNW film. (c) Frontal view of a hybrid CuNW/ZnO thin-film sample. (d) Edge view (at 5° grazing angle) of the hybrid CuNW/ZnO sample. .... 57

Figure 4.4. (a) Transmittance spectra of CuNW, CuNW/ZnO and CuNW/ZnO/rGO samples deposited on glass substrates. (b) Measured sheet resistance versus the number of days during which the samples were exposed to 85% relative humidity at 85 °C. The reduced graphene oxide (rGO) coating applied to the CuNW/ZnO film appears to prevent the penetration of moisture into

the pores and cracks of the ZnO matrix, thereby prolonging the TCE's lifetime. (c) SEM image of a CuNW/ZnO/rGO sample showing embedded CuNWs beneath the surface, and wrinkles in the rGO layer in the upper left-hand corner of the imaged area. .... 58

Figure 5.1. (left) Planar heterojunction perovskite solar cell architecture using a compact titanium dioxide layer as the ETL and Spiro-MeOTAD as the HTL. (right) Band diagram of the cell showing direction of electron and hole flow..... 61

Figure 5.2. (left) Six finished perovskite cells on ITO substrates and finished with silver back electrodes. (right) IV graph for high temperature two-step perovskite solar cell showing extremely low fill factor, regardless of short circuit current. Reference cell based on average literature high performance perovskite cell. .... 62

Figure 5.3. Diagram showing the effect of shunt losses and series losses in a solar cell.[122] In this diagram small effects of series and shunt resistance are shown, an order of magnitude small than the values in our cells..... 63

Figure 5.4. (left) Perovskite film formed on ITO substrate with TiO<sub>2</sub> electron transport layer. ITO electrode contact can be seen on the right side of the glass substrate. (right) Absorption data of both PbI<sub>2</sub> film and the resulting perovskite after dipping in MAI. .... 64

Figure 5.5. XRD graph showing peak shift from 12.3° to 14.08° (110 peak) consistent with perovskite conversion and elimination of PbI<sub>2</sub> precursor. ITO peaks are seen throughout both samples..... 65

Figure 5.6. (left) PbI<sub>2</sub> film deposited on TiO<sub>2</sub> ETL. (right) Converted perovskite via dip-coating from the same substrate. (center) Photo of examined substrate showing half of it that has been dipped in MAI solution for 5 minutes..... 66

Figure 5.7. (left) On-edge scanning electron image of a cleaved perovskite solar cell, showing approximate layers of the thin film device. Total cell thickness is ~600 nm. (right) Scanning electron micrograph of a perovskite film on top of ETL and ITO showing some pinholes in the layer..... 66

Figure 5.8. (left) I-V curve of illuminated solar cells based on three separate precursor solutions. (right) Scanning electron micrograph with inset of magnified perovskite grains deposited from DMSO based precursor. .... 67

Table 5.1. Comparison of different perovskite precursors used with identical deposition steps.. 68

Figure 5.9. Photograph of high-temperature-ETL perovskite cells showing the variance during spin coating based on precursor used, and ETL surface roughness. .... 68

Figure 5.10. (left) Inverted planar heterojunction perovskite solar cell using PEDOT:PSS as the hole transport layer and PCBM as the ETL. (right) Band diagram of completed solar cell showing direction of electron and hole flow. .... 69

Figure 5.11. I-V curves of the different ETLs used with hybrid perovskite solar cells. In all cases, the extremely high series resistance and low shunt resistance limits the fill factor greatly. .... 70

Table 5.2. Summary of performance characteristics of perovskite cells using different ETLs.... 70

Figure 6.1 . Rough schematic of etched ITO contacts with CuNWs sprayed on top for testing mechanical and chemical stability. Substrates are 1”x 1” in size..... 77

Figure 6.2. (a) Scanning electron micrograph of CuNWs that have been coated with nickel. (b) EDX of same area showing the nickel primarily on the wires. .... 78

Figure 6.3. Chart showing the progression in resistance across nickel coated CuNW TCE with each deposition step and process and over 48 hours in low humidity, room temperature environment. .... 79

Figure 6.4. (left) Photograph of CuNW film that heated PEDOT:PSS has been spin coated on in an incomplete film. (right) Optical micrograph of same CuNW film that has been eroded or displaced where PEDOT:PSS solution has contacted. .... 80

Figure 6.5. Progression of CuNW TCE (no nickel coating) resistance after process (final resistance measured is  $\sim 5000 \Omega$ ) ..... 80

Figure 6.6. (left) Microscope image of tape affixed to CuNW/TTIP TCE. (right) Same substrate with tape removed, showing robustness of conducting film..... 81

Figure 6.7. (a) Scanning electron micrograph showing a more realistic pattern of a full CuNW TCE, with bundles and multiple nanowires stacked on one another at intersections. (b) Photograph showing comparison to ITO TCE (left) perovskite cell and CuNW TCE perovskite cell showing the surface roughness that penetrates through all layers to the Ag fingers..... 82

Figure 6.8 . Difference in surface profile height when spin or spray coating PEDOT:PSS on CuNW TCEs to form a planar HTL. .... 82

Figure 6.9. Profilometry data showing the one method of surface planarization that worked to a quantifiable degree, rolling pressure on the CuNW TCE. .... 83

Table 6.2. Summary of conductivity restoring methods previously used on CuNW TCEs and attempted on a completed perovskite cell with CuNW back electrode. .... 84

Table 6.3. List of cell architectures attempted with CuNW back electrode stamped after vacuum filtration..... 84

Figure 6.10. (left) Completed perovskite solar cell with evaporated back electrode. (left) Completed perovskite solar cell with CuNW back electrode. .... 85

Figure 6.11. Comparison of transmission through a perovskite cell with and without CuNW back electrode, and a nearly opaque aluminum electrode. .... 85

Figure C.1 (left) SRM-232 surface resistivity meter. (right) Photograph of customized 4-probe electrode and Keithley source-meter setup. .... 92

## LIST OF TABLES

Table 3.1. Parameters of sol-gel deposited AZO and GZO thin films .....	44
Table 5.2. Summary of performance characteristics of perovskite cells using different ETLs....	70
Table 6.1. Summar of barrier layers tested on CuNWs to prevent corrosion from iodine elements in the perovskite layer. Some of these failures may not be a component of chemistry, but rather surface roughness and the film coverage, which is discussed later. ....	77
Table 6.2. Summary of conductivity restoring methods previously used on CuNW TCEs and attempted on a completed perovskite cell with CuNW back electrode. ....	84

## ACRONYMS AND TERMINOLOGIES

AFM	Atomic force microscope
AgNW	Silver nanowire
CuNW	Copper nanowire
DSSC	Dye-sensitized solar cell
ETL	Electron transport layer
FF	Fill-factor
FTO	Fluorine-doped tin oxide
GO	Graphene oxide
HTL	Hole transport layer
ITO	Indium-doped tin oxide
$I_{sc}$	Short circuit current
OSC	Organic solar cell
P3HT	Poly(3-hexylthiophene)
PCBM	[6,6]-phenyl- $C_{61}$ -butyric acid methyl ester
PSC	Perovskite Solar Cell
PEDOT:PSS	Poly(3,4-ethylenedioxythiophene) polystyrene sulfonate
PEN	Polyethylene naphthalate
PET	Polyethylene terephthalate
PVD	Physical vapor deposition
rGO	Reduced graphene oxide
$R_s$	Sheet resistance
SEM	Scanning electron microscope
TCE	Transparent conducting electrode
c-TiO <sub>2</sub>	Compact titanium dioxide layer
mp-TiO <sub>2</sub>	Mesoporous titanium dioxide layer
$V_{oc}$	Open circuit voltage
ZnO	Zinc oxide

## ABSTRACT

Recent advances in third generation photovoltaics, particularly the rapid increase in perovskite power conversion efficiencies, may provide a cheap alternative to silicon solar cells in the near future. A key component to these devices is the transparent front electrode, and in the case of Dye Sensitized Solar Cells, it is the most expensive part. A lightweight, cost-effective, robust, and easy-to-fabricate new generation TCE is required to enable competition with silicon.

Indium Tin Oxide, commonly used in touchscreen devices, Organic Light Emitting Diodes (OLEDs), and thin film photovoltaics, is widely used and commonly referred to as the industry standard. As the global supply of indium decreases and the demand for this TCE increases, a similar alternative TCE is required to accompany the next generation solar cells that promise energy with lighter and significantly cheaper modules. This alternative TCE needs to provide similar sheet resistance and optical transmittance to ITO, while also being mechanically and chemically robust.

The work in this thesis begins with an exploration of several synthesized ITO replacement materials, such as copper nanowires, conductive polymer PEDOT:PSS, zinc oxide thin films, reduced graphene oxide and combinations of the above. A guiding philosophy to this work was prioritizing cheap, easy deposition methods and overall scalability. Shortcomings of these TCEs were investigated and different materials were hybridized to take advantage of each layers strengths for development of an ideal ITO replacement. For CuNW-based composite electrodes, ~85% optical transmittance and ~25  $\Omega$ /sq were observed and characterized to understand the underlying mechanisms for optimization.

The second half of this work is an examination of many different perovskite synthesis methods first to achieve highest performance, and then to integrate compatible methods with our CuNW TCEs. Several literature methods investigated were irreproducible, and those that were successful posed difficulties integrating with CuNW-based TCEs. Those shortcomings are discussed, and how future work might skirt the issues revealed here to produce a very low cost, high performance perovskite solar cell.

# CHAPTER 1

## INTRODUCTION

### 1.1 INDUSTRY STANDARD TRANSPARENT CONDUCTING ELECTRODES

Transparent conducting films or transparent conducting electrodes (TCEs) are thin films of optically transparent and electrically conductive material. These two characteristics render it crucial to the function of such devices as liquid-crystal displays, Organic Light Emitting Diodes (OLEDs), touchscreens and photovoltaics[1]–[6]. These two performance characteristics, sheet resistance ( $R_s$ ) and optical transmittance ( $T$ ) are two key parameters commonly used to assess the suitability of a TCE for practical applications. Typically, low sheet resistance and high optical transmittance are desired, but this can vary depending on the specific application or its constraints. In the case of solar cells,  $R_s \leq 10 \Omega/\text{sq}$  is desired due to its contribution to series resistance ( $R_{series}$ ) in a completed cell, which directly affects the fill factor and efficiency. An optical transmittance of greater than 85% at visible wavelengths is also desired for photovoltaics, as more light received by the active material translates to a higher photocurrent. Several other desirable or even required parameters for TCEs in solar cells are discovered and discussed later in this thesis.

The present industry standard for TCEs is Indium Tin Oxide (ITO), which has a sheet resistance  $R_s = 10 \Omega/\text{sq}$  with optical transmittance  $T \approx 90\%$  for visible light.[7]–[11]. It is a ternary composition of indium, tin and oxygen in varied proportions, but typically oxygen-saturated with 74% In, 18% O<sub>2</sub>, and 8% Sn by weight. Its large bandgap of 4 eV makes it mostly transparent in the visible spectrum and its extinction coefficient,  $k$ , in this wavelength range is zero. Transparent and colorless in thin layers, it is yellowish to grey in bulk form. In the ultraviolet (UV), infrared (IR), and near-IR region it is opaque, reaching a maximum  $k$  in the IR regime, similar to the behavior of  $k$  for metals.[12]

Due to the scarcity of indium and growing market demand, alternative TCEs are desired[13] as a report from the U.S. Geological Survey's Mineral Resources Program showed the average price of indium from U.S. producers has risen from \$565 to \$735 per kilogram over the past 5 years[14]. Moreover, TCEs that are compatible with flexible substrates are favored nowadays for applications such as wearable electronics, a market in which ITO fails due to rigidity. Because of these drawbacks, much effort has been directed in recent years toward finding substitute materials for ITO. Fluorine doped tin oxide serves as a similar but inferior TCE (in specific applications), with higher haze, lower transmittance, but better stability at higher temperatures[15]. This is more ideal for mesoporous perovskite or DSSC architectures which require a 450-500 °C annealing step. TO can be deposited via magnetron sputtering on polyethylene naphthalate (PEN) and polyethylene terephthalate (PET) substrates, but increased degradation with bending cycles and higher sheet resistance are tradeoffs that come with flexibility[16]. Many alternative TCEs have been investigated in the last decade, such as indium-free conductive metal oxides[17], metal meshes, conductive polymers[18], nanowire grids, and graphene[1].

## **1.2 ALTERNATIVE TRANSPARENT CONDUCTING ELECTRODES**

Many nano-materials have been developed to replace ITO as a TCE, but each comes with limitations inherent to the material or tradeoffs for the specific application. Indium-free conducting metal oxides like fluorine doped tin oxide, zinc oxide or doped zinc oxide are commonly used as TCEs[19]–[21]. These films are typically deposited via vacuum processes such as sputtering or physical vapor deposition (PVD), and have slightly inferior performance to ITO. Sol-gel films of similar material have also been investigated due to ease of fabrication and scalability, but also produce inferior conductivity to ITO[19], [22].

Conductive polymers such as poly(3,4-ethylenedioxythiophene) polystyrene sulfonate (PEDOT:PSS) have also been investigated as a TCE; with commercially available mixtures having conductivity from 100-1000 S/cm, but can be further improved to 4600 S/cm with appropriate treatment[23]. Because of the mechanical flexibility of PEDOT:PSS, it is also used as a counter electrode for thin film photovoltaics (not necessarily transparent, but with higher conductivity)[24]–[26]. When mixed with poly(3-hexylthiophene), PEDOT:PSS is also used as a hole transport layer in organic solar cells, in addition to being a planar hole transport layer in low-temperature perovskite solar cells[27]–[30].

Single-layer graphene exhibits excellent optical and electrical properties, yielding  $R_s = 30 \Omega/\text{sq}$  and  $T = 90\%$  when fabricated via chemical vapor deposition[2]. This process, while being excellent in quality, is difficult to scale up and costly to mass produce. Reducing graphene oxide (GO) is a cost-effective solution for large area TCEs, but comes with limitations in electrical/optical properties and uniformity due to attached functional groups or fabrication defects. Transparent conducting electrodes of only rGO have achieved  $R_s = 200\text{-}300 \Omega/\text{sq}$  with  $T = 80\%$  on glass[31], [32].

Metal nanowires made with copper, silver, and gold are used as TCEs by depositing on glass substrates. These nanowires can be deposited on flexible substrates to fabricate bendable or even deformable TCEs[16], [33]–[35]. Silver nanowires (AgNW) are typically synthesized via a polyol process, and can exhibit lengths of 25-40  $\mu\text{m}$  and diameters as low as 35 nm[36], [37]. The best AgNW TCEs reported have  $R_s < 25 \Omega/\text{sq}$  and  $T = 90\%$ . Copper nanowires (CuNW) are synthesized using different solution processes that yield nanowires from 10  $\mu\text{m}$  to millimeters in length and diameters of 24-100 nm[35], [38], [39]. Once deposited on substrates and treated to restore conductivity by fusing the nanowires together, they can yield  $R_s = 50 \Omega/\text{sq}$  and  $T = 93\%$ .

With higher nanowire concentration, a lower sheet resistance and lower optical transmittance can also be achieved, the extreme case being a film that resembles bulk copper with no optical transmittance . This process can be tuned in the other direction as well, by lowering the number of wires per unit area and thereby increasing the exposed substrate area.

### 1.3 DYE SENSITIZED SOLAR CELLS

The second portion of this thesis is dedicated to the development of in-house solar cells with the purpose of integration of copper nanowire and hybrid TCEs. Initial work was conducted with a collaborator using Organic Solar Cells (OSCs), but the few trials conducted were unsuccessful due to shorting caused by rough surface profile inherent to CuNW. Dye Sensitized Solar Cells (DSSCs), also known as the Grätzel Cell, were investigated because of their low cost and ease of synthesis. These features make them ideal candidates for low budget projects such as college and even high school labs[40]–[42]. DSSCs were co-invented by Brian O'Regan and Michael Grätzel in 1988, and the first high-efficiency cell was published by them in 1991.[43] The underlying technology that functions within DSSCs was first discovered in 1960, when illuminated dyes were seen to generate electricity at oxide electrodes in electrochemical cells.[44]

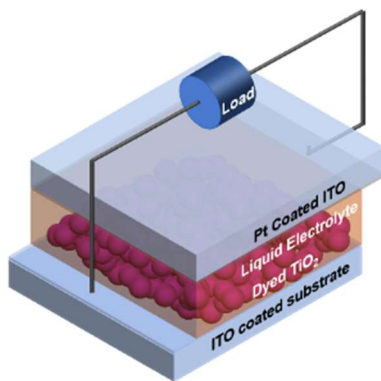


Figure 1.1. Diagram of a basic DSSC (not to scale) illustrating the buildup of each layer sandwiched between two ITO electrodes. In a cell without spacers, the electrolyte is held in the cell by capillary action.

Today, a modern DSSC is composed of a porous layer of titanium dioxide nanoparticles coated by a molecular dye that absorbs sunlight, much like chlorophyll in leaves. The titanium dioxide is immersed in an electrolyte solution which also makes contact with a platinum-based catalyst thin film located at the cathode. Sunlight passes through the transparent front electrode into the dye-stained titanium dioxide, generating electrons that flow through the  $\text{TiO}_2$  towards the front electrode. After flowing through the external circuit, they are reintroduced into the cell on a metal electrode (typically platinum or graphite) and into the electrolyte, which transports them back to the dye molecules and the cycle is complete.

In a classroom setting, raspberry or blackberry dye can be used as the active layer absorber staining the  $\text{TiO}_2$  mesoporous scaffolding. A basic cell can be assembled with such a dye,  $\text{TiO}_2$  nanoparticles, hotplate, isopropyl alcohol, a few squares of ITO coated glass, a graphite pencil, and an iodine electrolyte. Hobby kits exist to replicate these cells, and while they are very low in efficiency, they can present the basics of photovoltaics to students with a simple multimeter and sunlight.

Cutting edge DSSCs typically use a ruthenium-based molecular dye [ $\text{Ru}(4,4'\text{-dicarboxy-2,2'\text{-bipyridine})_2(\text{NCS})_2$ ] (N3 or N719) coating a 12  $\mu\text{m}$  thick film of transparent 10-20 nm diameter  $\text{TiO}_2$  nanoparticles followed by a 4  $\mu\text{m}$  thick layer of much larger  $\text{TiO}_2$  nanoparticles (400 nm diameter) for scattering photons back into the transparent film. The photo-generated electrons diffuse through the sintered nanoparticle network to be collected at the front transparent electrode, while the dye is regenerated via reduction by a  $\text{I}_3/\text{I}$  redox shuttle contained in a high-performance liquid electrolyte. Diffusion of the oxidized form of the shuttle to the back electrode

completes the circuit.[44] DSSCs are one of the most efficient third-generation solar cells available (validated power conversion efficiency  $\eta = 14.1\%$  [45]), making them attractive as a replacement for existing technologies in “low density” applications like rooftop solar collectors where the mechanical robustness and light weight of the glass-less collector is valued. While not as efficient as the more expensive silicon cells used in large-scale deployments, small increases in DSSC conversion efficiency could make them more viable in the future.[46]

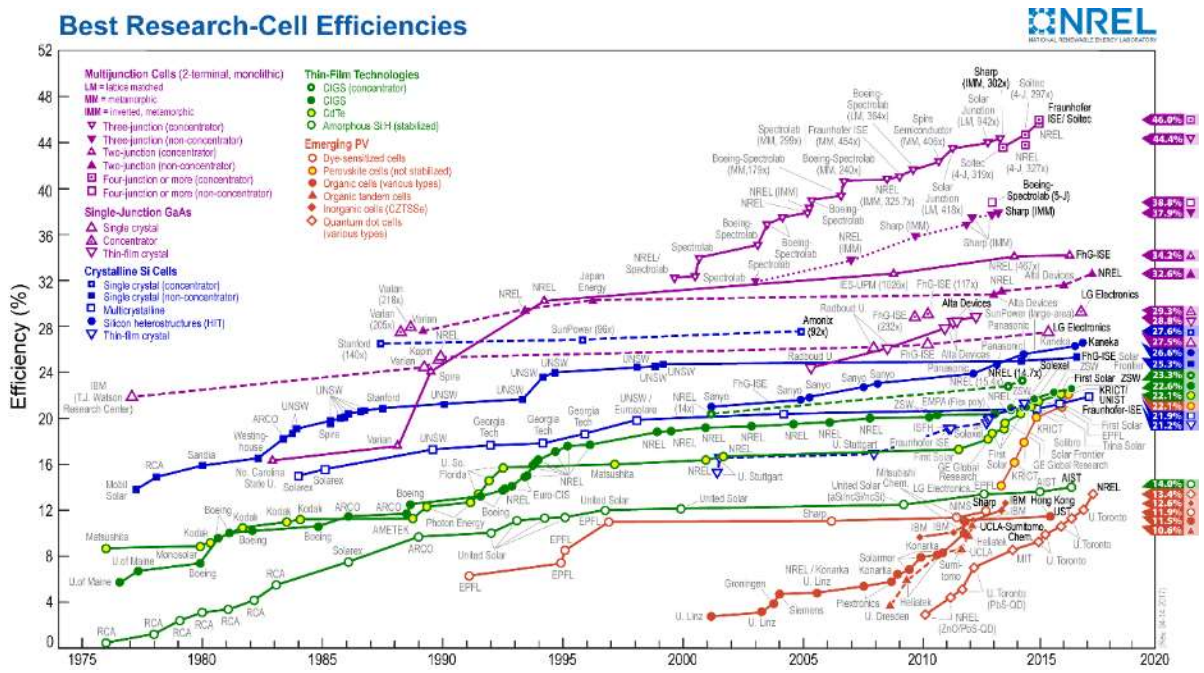


Figure 1.2. Research Cell Record Efficiency Chart provided by National Renewable Energy Laboratory (NREL).[45] Note the quick increase in emerging PV technologies compared to crystalline Si cells.

### 1.4 THIN FILM PHOTOVOLTAIC TECHNOLOGY

Emerging photovoltaic cell technology over the past two decades have included dye-sensitized cells (DSSCs), organo-inorganic halide perovskite cells, organic cells and inorganic cells, and quantum dot cells[47], [48]. While these photovoltaic cells have efficiencies below 25% and are far inferior to silicon photovoltaics in terms of stability[49] and multi-junction cells in power conversion efficiency, they all have shown great improvement since their inception,

particularly organo-inorganic hybrid perovskite cells[50]–[54]. Perovskite solar cells (PSCs) have grown rapidly in design and efficiency since their inception in 2009.[55] Perovskite photovoltaic cells began as a modification to dye-sensitized solar cells, with the ruthenium absorber replaced by perovskite in the mesoporous architecture[54], [56], [57]. This was later modified into planar heterojunction perovskite cells [58] to make easier in deposition, which led to low-temperature synthesis, paving the way for low-cost, low temperature perovskite photovoltaics[30], [53], [59]–[64].

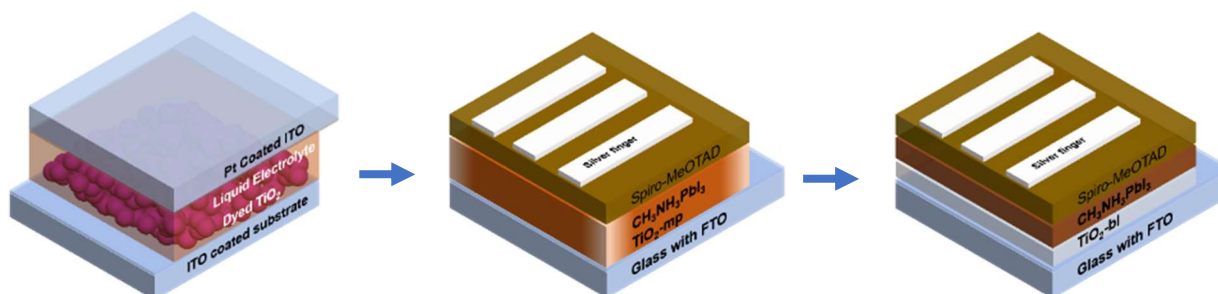


Figure 1.3. (from left) Evolution of perovskite solar cell from DSSC architecture. The mesoporous scaffolding layer is eventually removed in favor of a much thinner scaffold-free perovskite layer.

Today, the record laboratory-scale power conversion efficiency is 22.1% (certified by NREL <https://www.nrel.gov>) and has grown in research interest rapidly, from the initial first publication in 2009 to 1100 in 2015.[55] The more common perovskite precursors used are methylammonium iodide ( $\text{CH}_3\text{NH}_3\text{PbI}_3$ ), methylammonium bromide ( $\text{CH}_3\text{NH}_3\text{PbBrI}$ ), and methylammonium lead iodide with traces of chlorine ( $\text{CH}_3\text{NH}_3\text{PbI}_{3-x}\text{Cl}_x$ ) dissolved in N,N-dimethylformamide (DMF) or dimethyl sulfoxide (DMSO).[60], [65]–[70]

In a typical planar heterojunction PSC, the device is constructed on a fluorine-doped tin oxide (FTO) coated substrate. A titanium dioxide ( $\text{TiO}_2$ ) layer  $\sim 40$  nm thick is spin coated onto the substrate and serves as the electron transport layer (ETL). After annealing the  $\text{TiO}_2$  layer at  $450\text{--}500$  °C to sinter the particles together, the active layer is deposited via spin coating and then

heated at  $\sim 100$  °C to complete the transformation from lead iodide to perovskite. Spiro-MeOTAD (2,2',7,7'-tetrakis-(N,N-di-p-methoxyphenylamine)-9,9'-bifluorene) is then spin-coated on top as the hole transport layer. The cell is subsequently transferred to a vacuum chamber for evaporation of a silver or gold back contact. The low temperature analogy architecture inverts the electron and hole transport layers so that PEDOT:PSS is spin coated onto the transparent front electrode as the HTL, and [6,6]-phenyl-C<sub>61</sub>-butyric acid methyl ester (PCBM) in chlorobenzene is used as the electron transport layer, with evaporated aluminum as the back electrode. The inverted architecture is favorable for  $< 150$  °C processing steps, and achieves similar efficiencies.[71] In the research presented in this thesis, many of these architectures were implemented to determine the most compatible with copper nanowire hybrid TCEs and achieve highest performance.

## CHAPTER 2

# ULTRA-HIGH ASPECT RATIO COPPER-NANOWIRE-BASED HYBRID TRANSPARENT CONDUCTIVE ELECTRODES WITH PEDOT:PSS AND REDUCED GRAPHENE OXIDE EXHIBITING REDUCED SURFACE ROUGHNESS AND IMPROVED STABILITY

### 2.1 INTRODUCTION

Transparent conductive electrodes (TCEs) are widely used in applications ranging from touch screens and displays in consumer electronics to light emitting diodes and solar panels.[2]–[6] Among the relevant performance characteristics, sheet resistance ( $R_s$ ) and optical transmittance (T) are two key parameters commonly used to assess the suitability of a TCE for practical applications. In general, low sheet resistance and high optical transmittance are desired, although the minimum requirements vary depending on the specific application. With a typical transmittance of greater than 85% at visible wavelengths, a sheet resistance  $< 200 \Omega/\text{sq}$  is usually sufficient for many touch screen applications, while  $R_s \leq 10 \Omega/\text{sq}$  is necessary for solar cells and OLEDs.

The present industry standard for TCEs is Indium Tin Oxide (ITO), which has  $R_s \approx 10 \Omega/\text{sq}$  and  $T \approx 90\%$  for visible light.[7]–[9] However, due to the scarcity of indium, there has been a push towards finding alternative materials coatings that can match or overcome the performance metrics offered by ITO. Moreover, TCEs that are compatible with flexible substrates are favored nowadays for applications such as wearable electronics, a market in which ITO fails due to its rigidity. Because of these drawbacks, much effort has been directed in recent years toward finding substitute materials for ITO.

Several alternatives have been investigated to serve as TCE during the past decade. Indium-free conductive metal oxide, for instance, doped Zinc Oxide and Tin Oxide have been the subject of many investigations. Typically, large energy input and a vacuum environment are required to produce high quality oxide films using thin-film deposition techniques[72]. Other fabrication methods such as sol-gel deposition have also been used at high annealing temperatures to produce conductive oxide coatings.[73], [74] Carbon-based nano-materials such as carbon nanotubes and graphene have been used to fabricate TCEs as well. Carbon-nanotubes-based TCEs typically have  $R_s=150 \text{ } \Omega/\text{sq}$  at  $T=80\%$ .[6] With a sheet resistance of  $30 \text{ } \Omega/\text{sq}$  at  $T=90\%$ , continuous graphene films grown with chemical vapor deposition show excellent performance.[2] Solution processed graphene flakes are also investigated due to their low cost and ease of fabrication; these TCEs exhibit  $R_s$  values ranging from  $200\text{-}300 \text{ } \Omega/\text{sq}$  at  $T=80\%$ .[5] Among all the materials investigated to date, percolating metal nanowire films are the most promising choices for TCE. Specifically, silver nanowire (AgNW) ink synthesized via a solution route can be readily deposited on select substrates using techniques such as spin-coating, spray coating, dip-coating, Mayer rod coating, or vacuum filtration followed by dry transfer. Each of these methods has been employed to produce high performance TCEs. However, silver is similar in abundance to indium, which hinders its large-scale applications.

Copper has a low bulk resistivity (i.e.,  $16.8 \text{ n}\Omega\cdot\text{m}$  compared to  $15.9 \text{ n}\Omega\cdot\text{m}$  for silver) and is 1000 times more abundant. Rathmell et al. have demonstrated the synthesis and deposition of copper nanowires (CuNWs) in large quantities;[35] however, owing to the nanowires' low aspect ratio, the sheet resistance and optical transmittance of the fabricated TCEs were still not suitable for many applications. According to the prediction of one-dimensional stick percolation theory,[75] the nanowire density  $N$  is related to the length of wire  $L$  in accordance with:

$N = (4.236/L)^2/\pi$ . This indicates that the longer the nanowires are, the fewer will be needed to form a percolating network, which will then occlude less light. Knowing the importance of the length of nanowires in TCE applications, Guo et al. employed a catalytic effect to synthesize CuNWs with large aspect ratios.[38]

While CuNWs are promising material for TCE applications, there remain many challenges that need to be addressed prior to their commercialization. Annealing of the as produced nanowire coatings at moderate to high temperatures is necessary to form good contacts at wire-wire junctions in order to achieve acceptable levels of electrical conductivity (i.e. achieve sufficient percolation). However, the annealing temperatures are usually high enough to prevent the use of flexible substrates. In addition, copper is known to oxidize in air. The degradation due to oxidation will be far more substantial for nanowires than for bulk copper, because of the larger surface area of the nanowires that is exposed to air. From a device integration perspective, the surface roughness of the TCEs is also a crucial limiting factor in many applications: since the percolating nanowire network contains hills at wire-wire junctions and voids in between the wires, the existence of such peaks and valleys could give rise to electrical shunts and shorts in the fabricated devices.[18]

In this work, we synthesized ultra-long CuNWs using a solution method adopted from the work of Guo et al,[38] and obtained TCEs that are, in some respects, superior to those fabricated with previously synthesized copper and silver nanowires. We then adopted a transfer technique to deposit CuNWs onto a PET substrate, thus avoiding the exposure of the substrate to annealing procedures. We also managed to embed the nanowires in a PEDOT:PSS thin film, similar to what Gaynor et al. have done with AgNWs,[18] which helped to reduce the surface roughness of our TCEs. Additionally, by applying reduced graphene oxide (rGO) platelets as an over-coating layer,

we succeeded in preventing the oxidation of CuNWs and also improving the stability of our TCEs in high humidity and high temperature environments.

## 2.2 EXPERIMENTS

**2.2.1 Nanowire synthesis** Two methods of copper nanowire synthesis were carried out in order to compare the resulting aspect ratios. Our first method of copper nanowire synthesis was a one-step solution process following several procedures reported by Rathmell et al [35] and summarized in the supplemental information. The nanowires were found to be between 30 – 50  $\mu\text{m}$  long, with diameters ranging from 120 – 500 nm.

Our second method of copper nanowire synthesis follows the one-step solution process of Guo et al.[38] and is used throughout this work. Briefly, 20 ml of Oleylamine was pipetted into a 50 ml capacity round-bottom 3-neck flask, in which temperature was precisely controlled by a Glas-Col Digi-II system. Subsequently 1.6 mmol  $\text{CuCl}_2$  and 0.8 mmol  $\text{Ni}(\text{acac})_2$  were added to the flask which was purged with high-purity Argon. The mixture was vigorously stirred and kept at 80  $^\circ\text{C}$  for 30 minutes to achieve a full dissolution that had a dark blue color. The temperature was then ramped up to 175  $^\circ\text{C}$  to initiate the anisotropic growth of copper nanowires. This reaction continued for at least 10 hours, during which high-purity Argon was purged into the flask. During the reaction, the solution underwent color changes from dark blue to clear brown to opaque red. After the reaction was completed, the red suspension was allowed to cool down to room temperature. Equal volume of hexane was poured into the flask to precipitate the nanowires from the solution. Copper nanowires were then separated from the solvent via centrifugation (6000 rpm, 15 minutes, at least 3 times), followed by dispersing in an Isopropyl alcohol (IPA) solution containing 1 wt% Polyvinylpyrrolidone (PVP). Finally, the nanowires were washed and stored in IPA.

**2.2.2 Fabrication of CuNW TCEs** Several methods of TCE fabrication were used with both silver or CuNW combined with graphene, or PEDOT:PSS to determine the best performers. The results obtained with silver nanowires and with the initially synthesized copper nanowires are detailed in the supplemental information. The second method of copper nanowire growth described in the preceding subsection yielded the highest aspect-ratio nanowires (see Results and Discussion); the majority of our investigations involving flexible substrates and resulting in our highest performing samples were carried out using these materials. Suspensions of CuNWs in IPA form a stable solution that can be readily spray-coated via an airbrush (Paasche Model H) onto a flat substrate. Glass substrates were fixed on a tilted hot-plate, on which the temperature was maintained at 60 °C to facilitate evaporation of solvent and avoid flooding. The spraying condition was optimized for uniform distribution of the nanowire network, with the spraying distance of 10 cm and the spraying pressure in the delivery tube ~15 psi. The density of nanowires can be controlled by varying the volume of material sprayed onto the target substrate. Larger volumes of sprayed CuNW suspension consistently resulted in denser networks.

To remove the excess organics and to improve contact at wire-wire junctions, two different annealing techniques were used after spray-coating the substrates. In one case, the samples were annealed in a tube furnace under a forming gas environment (95% N<sub>2</sub> + 5% H<sub>2</sub>) at various temperatures for 1 hour. Upon completion, the samples were cooled to room temperature in the forming gas atmosphere in order to avoid re-oxidation. In other cases, the annealing was performed using low-pressure (< 5 torr) air plasma (PLASMA-PREEN-II-862) for 2 minutes.

**2.2.3 Fabrication of PEDOT:PSS/CuNW hybrid thin films** PEDOT:PSS modified with 5 wt% Dimethyl Sulfoxide (DMSO) was used to spin-coat flexible PET substrates.[76] Prior to deposition, the PET substrates were plasma cleaned for 20 seconds to improve their hydrophilicity.

Typically, 0.4 ml of DMSO modified PEDOT:PSS was pipetted onto the substrate and spun at 2000 rpm for 40 seconds, followed by 4000 rpm for 15 seconds to dry the film.

To fabricate the PEDOT:PSS hybrid films, a pre-annealed CuNW film on a glass substrate was placed facing down onto the PEDOT:PSS layer. The CuNW film was subsequently transferred and embedded into the PEDOT:PSS layer by applying a pressure of ~20 MPa using a shop press. The pressure was applied for at least 10 seconds before lifting the upper substrate.

#### **2.2.4 Fabrication of CuNW/reduced Graphene Oxide (rGO) hybrid thin films**

Graphene oxide (GO) was purchased from Graphene Supermarket. GO is separated from the stock solvent via centrifugation and dispersed in IPA at 0.02 mg/ml. The IPA suspension was spray-coated onto a CuNW film (prior to annealing the CuNWs) under the same spraying conditions as described earlier. The samples were then annealed in a forming gas environment at 200 °C for 1 hour.

**2.2.5 Sample Characterization** Scanning electron microscope (SEM, Hitachi S-4800 Type II) was used to examine fabricated CuNW films, PEDOT:PSS/CuNW films, and CuNW/rGO films. Cross-sectional SEM images were captured by mounting the substrate vertically, while angled SEM images of the PEDOT:PSS/CuNW films were captured by mounting the samples vertically and tilting the stage by 5°. Atomic force microscopy (AFM) was used to study the surface morphology of synthesized materials and fabricated thin films. Raman spectroscopy for GO and rGO was acquired with Renishaw's structural and chemical analyser. Optical transmittances were measured by a Cary UV-Vis-NIR spectrophotometer and corrected with blank substrates. Haze measurements were conducted with an integrating sphere, using SuperK COMPACT supercontinuum white light laser (450 – 2400 nm) as light source and Ocean Optics USB4000 Spectrometer as detector. Sheet resistances were measured with a four-point probe

(SRM-232-2000) at multiple locations on all samples. A Veeco DEKTAK 150 profilometer was used to measure the surface profiles of the PEDOT:PSS/CuNW films.

## 2.3 RESULTS AND DISCUSSION

**2.3.1 CuNW synthesis** CuNWs were synthesized using the solution process suggested by Guo et al.[38]. A photograph of a homogeneous CuNW suspension in IPA is shown in Fig. 2.1a. Scanning electron microscopy (SEM) was conducted to study the dimensions of the synthesized nanowires, which were spray-coated (using an airbrush) onto glass substrates. A randomly oriented but uniformly distributed network of nanowires was seen to have formed after spraying; see Fig. 1b. We randomly select 50 nanowires from the SEM images and measured an average length of 75  $\mu\text{m}$  and average diameter of 45 nm, corresponding to an aspect ratio of  $\sim 1600$ . A high magnification SEM image (Fig. 2.1c) of a nanowire bundle reveals a narrow distribution of wire diameters. Atomic Force Microscopy revealed the smoothness of the nanowire surfaces (see Fig. 2.2).

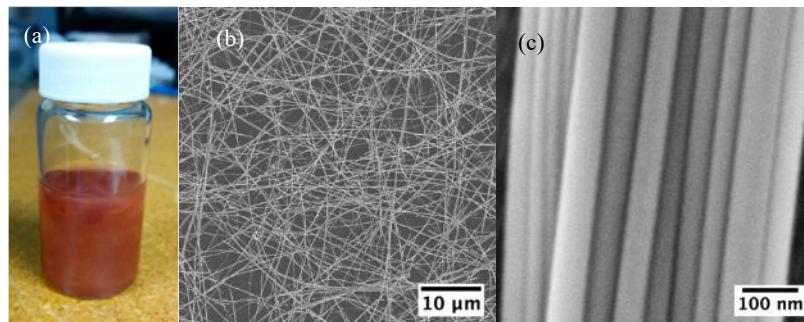


Figure 2.1. (a) Photograph of synthesized CuNWs in IPA suspension. (b) SEM image of synthesized CuNWs spray-coated onto a glass substrate; the nanowires are seen to be homogeneously distributed. (c) SEM image of a nanowire bundle shows the wires' fairly uniform diameter.

Due to the insulating nature of the organic coatings that remain on nanowires after the fabrication process is completed, the wire-wire junctions typically have high electrical resistance; as a result, the samples are not electrically conductive. Removal of the organics is thus necessary

to improve electrical contact at wire-wire junctions. Thermal annealing and plasma treatment of the spray-coated CuNW thin films were employed for removal of the organics and causing the nanowires at overlapping junctions to meld. The two methods exhibited varying degrees of effectiveness and practical convenience. Thermal annealing of spray-coated CuNWs was conducted on 5 samples with similar nanowire densities under a forming gas environment (95% N<sub>2</sub> + 5% H<sub>2</sub>) at temperatures ranging from 100 to 300 °C, in 50 °C increments for 1 hour. Upon completion of the annealing process, the samples were cooled to room temperature. (It is important that the samples are cooled in the reducing atmosphere in order to avoid re-oxidation.) The sheet resistance of each annealed sample was measured with a four-point probe at multiple locations, and then averaged for each sample. From Fig. 2.3a, it is seen that the sheet resistance and also the standard deviation of the measurements are optimum when the sample is annealed at 200 °C. Figures 3c and 3d are AFM images of wire-wire junctions for un-annealed and annealed samples, respectively, while figures 3e and 3f are the corresponding line height profiles for the two samples. For the un-annealed sample, the junction height (red profile) is approximately the sum of the heights of two individual wires (black profile). However, for the annealed sample, the junction height is seen to be only slightly higher than each of the wires, indicating nano-fusion. This melding of the nanowires at various junctions is believed to be primarily responsible for improvements of the sheet resistance. As we increased the annealing temperature beyond 200 °C, the sheet resistance increased slightly, presumably due to the coalescence of CuNWs.[75]

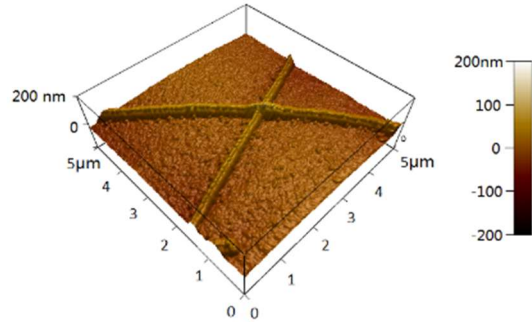


Figure 2.2. 3D reconstructed AFM image showing the smoothness of the nanowire surface.

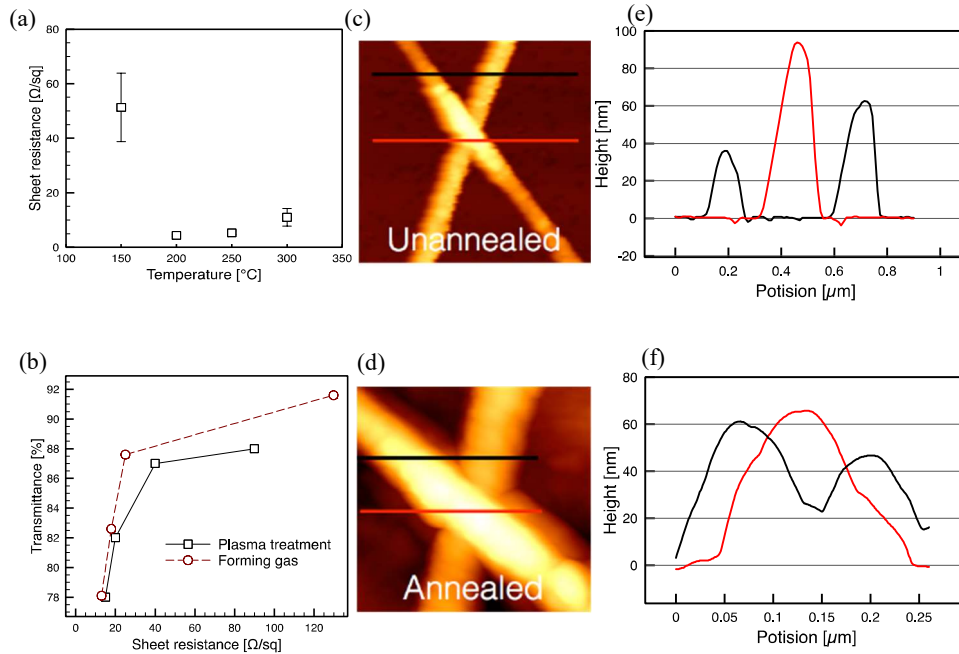


Figure 2.3. (a) Sheet resistance  $R_s$  versus annealing temperature in a forming-gas atmosphere for one hour. (b) Optical transmittance  $T_{550}$  versus sheet resistance  $R_s$  for thermal annealing in forming-gas (red), and for plasma cleaning (black). (c-f) AFM images and line height profiles of un-annealed and annealed nanowire junctions.

Removal of organic coatings of CuNWs could also be achieved using plasma treatment (as an alternative to thermal annealing). The plasma treatment was carried out under a low-pressure air environment ( $< 5$  torr) for 2 minutes, which is approximately the maximum treatment time before sample deformation occurs. Fig. 2.3b shows a comparison of sheet resistance  $R_s$  and optical transmittance  $T_{550}$  obtained using each annealing techniques under their respective optimal

conditions (i.e., thermal annealing at 200 °C for 1 h, and plasma treatment under low-pressure air for 2 minutes). While thermal annealing in a forming gas atmosphere provides slightly better sheet resistance at a given optical transmittance compared to plasma treatment, the latter method has the advantages of speed (two minutes compared to over an hour, including cooling) and simplicity (e.g., no need for a special gas). Thus, these features of plasma treatment are advantageous in commercial grade fabrication.

**3.2 Composite electrode with PEDOT:PSS/CuNW** It is well known that the surface roughness of the electrode is an adverse factor in many opto-electronic applications.[77], [78] With the CuNW TCE, since the nanowires form a network by stacking on top of each other, the wire-wire junctions are significantly elevated above the voids in between nanowires. This rough morphology of the nanowire network can result in local thinning of any active or passive layer that is subsequently deposited over the metallic network, which leads to shunting or shorting.<sup>18</sup> In order to reduce the surface roughness of our CuNW TCEs, we adopted a transfer method similar to what Gaynor *et al.* have done with AgNWs.[18] Pre-annealed CuNW films were deposited onto a different glass or polyethylene terephthalate (PET) substrate, and they were embedded in a conductive polymer film (PEDOT:PSS). The schematic of the transfer process is shown Fig.4. CuNWs were spray-coated onto a glass substrate and, subsequently, plasma treated under previously described conditions. Typically, films of plasma-treated CuNWs had  $T_{550} = 87\%$  and sheet resistance  $R_s = 23.1 \pm 4.8 \Omega/\text{sq}$ . As a receiving layer, PEDOT:PSS was spin-coated onto a glass or a PET substrate and dried. Typical PEDOT:PSS thin films used in this work have thickness  $\sim 70$  nm. The sheet resistance of the PEDOT:PSS film, being greater than 500 k $\Omega/\text{sq}$ , is therefore negligible as a contributing factor to the final conductivity of the composite electrode. The pre-annealed (percolated) CuNW network was finally transferred onto the PEDOT:PSS film under the

~20 MPa pressure of a shop press. The transfer process has nearly a 100% yield, meaning that all of the nanowires from the donor substrate were transferred to the target substrate. After complete transfer, the PET/PEDOT:PSS/CuNW samples had a sheet resistance of  $R_s \sim 25 \Omega/\text{sq}$ , consistent with those of bare CuNW networks.

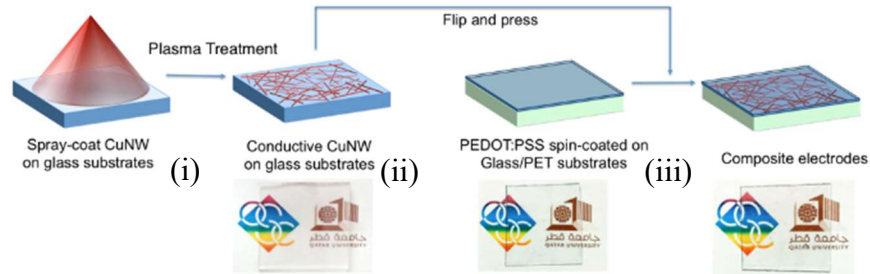


Figure 2.4. Schematic depiction of the transfer process for spray-coated CuNWs to a spin-coated PEDOT:PSS film using the “flip and press” method. The photographs below the diagram show, from left to right, (i) CuNWs on a glass substrate, (ii) PEDOT:PSS film on a PET substrate, and (iii) hybrid TCE on a PET substrate. In each case, the OSC and QU logos are placed beneath the substrate in order to allow visual comparison of the samples’ transparencies.

Figures 2.5a and 2.5b are the cross-sectional SEM images of the transferred CuNWs on PET substrates without and with the PEDOT:PSS thin film. In the absence of the PEDOT:PSS receiving layer, it is easy to observe nanowires sticking out of the plane of the sample (Fig. 2.5a). In contrast, when CuNWs are transferred onto the PEDOT:PSS layer, the cross-sectional profile becomes cleaner and shows fewer nanowires sticking out of the surface (Fig. 2.5b). The reduction of the surface roughness can also be seen from SEM images taken at a viewing angle of  $5^\circ$  (see Figs. 2.5c and 2.5d). Whereas in Fig. 2.5c spray-coated CuNWs on a glass substrate can be identified individually, especially at the junctions, a smoother and more homogeneous surface is seen to have been obtained in Fig. 2.5d when the CuNWs are transferred onto a PEDOT:PSS layer on a PET substrate. Furthermore, PEDOT:PSS is widely employed in organic electronics applications as a buffer layer between those of ITO and the active materials to improve contact

and charge injection. Therefore, we chose to employ PEDOT:PSS as a receiving layer to improve both the smoothness as well as integration with active materials for future device explorations.

Surface profilometer was used to measure the surface roughness of our samples; three scanning locations are randomly chosen on each sample and each scan covers 1 mm length. The results of these measurements are plotted in Fig. 2.5e. The spray-coated CuNWs on glass exhibit rougher surface profiles, with arithmetic average roughness  $R_{ave} = 57.28$  nm and root mean squared roughness  $R_{RMS} = 73.93$  nm averaged over the 3 scans. Many peaks are seen due to the surface morphology of the nanowire network. Figure 2.5f is the surface profiles of PEDOT:PSS/CuNW thin film. Comparison of the height profiles (Fig. 2.5f and 2.5e) reveals smoother film (lower peak heights, Fig. 2.5f) for the PEDOT:PSS embedded CuNW networks. The surface roughness values for these are  $R_{ave} = 17.4$  nm and  $R_{RMS} = 25.8$  nm. Therefore, the transfer of CuNWs into PEDOT:PSS reduces the surface roughness considerably, which is a desirable feature for device integration. Additionally, since the mechanical transfer process does not involve any thermal treatment of the accepting substrate, this technique can be used with different substrate materials, resulting in substrate-independent values of sheet resistance. This approach is invaluable for achieving the high performance TCE on flexible, plastic supports.

The fabricated PEDOT:PSS/CuNW hybrid TCE, having high optical transmittance and low haze value over the visible spectrum ( $T_{550} = 84.2\%$ ; Haze  $\approx 6\%$ ; see Fig. 2.6a) and low sheet resistance ( $R_s \sim 25 \Omega/\text{sq}$ ), is suitable for many practical applications. To test the mechanical durability of the fabricated TCEs on flexible PET substrates, a sample was bent 400 times (bend radius  $\sim 5$  cm) and its sheet resistance was recorded after every 50 bending cycles; the results are plotted in Fig. 2.6b. In the first 300 bending cycles, there was no notable change in  $R_s$ , indicating the mechanical stability of the fabricated PET/PEDOT:PSS/CuNW TCEs.

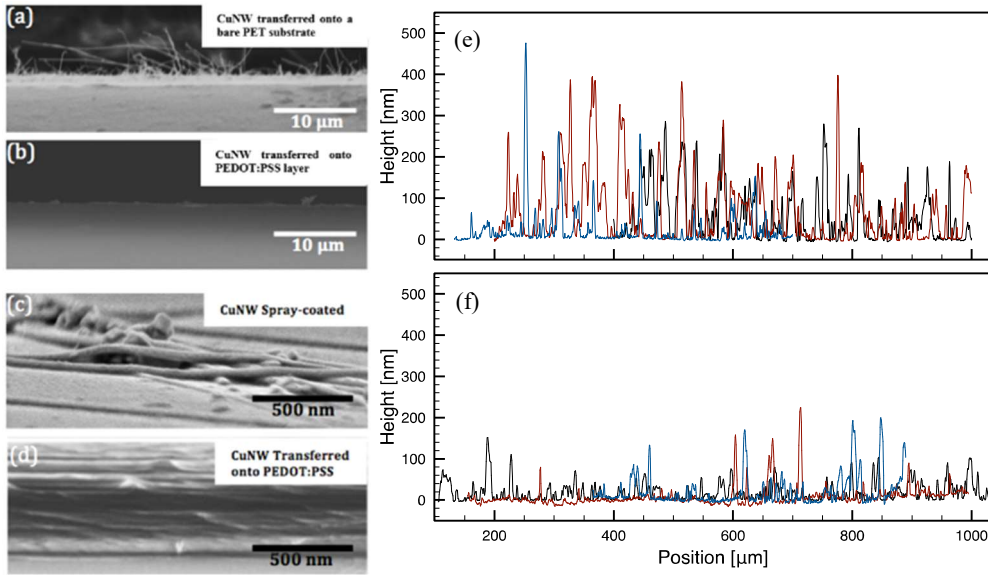


Figure 2.5. (a) Cross sectional SEM view of CuNWs transferred to a bare PET substrate, showing numerous nanowires sticking out of the plane of the substrate; (b) Cross sectional SEM view of CuNWs transferred to a spin-coated PEDOT:PSS film atop a PET substrate; hardly any nanowires are seen to be sticking out of the plane in this case. (c) Angled SEM image of spray-coated CuNWs on a glass substrate; (d) Angled SEM image of CuNWs transferred onto a thin film of PEDOT:PSS atop a PET substrate. (e) Surface profiles of spray-coated CuNWs on a glass substrate; and (f) Surface profiles of PEDOT:PSS/CuNW thin film exhibiting substantially reduced roughness. Different colors represent different scans.

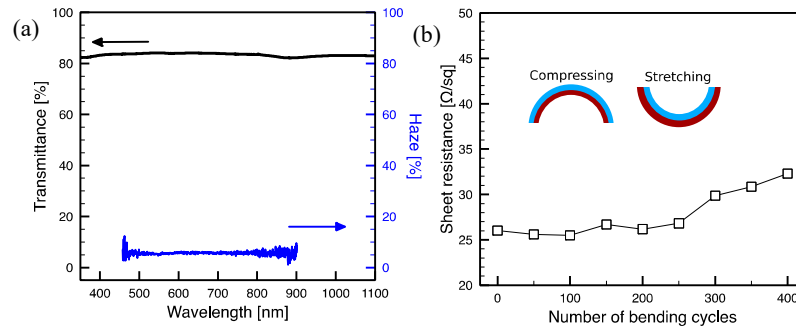


Figure 2.6. (a) Optical transmittance spectrum and haze of a PEDOT:PSS/CuNW sample on a PET substrate. The inset shows a photograph of the corresponding sample placed over OSC and QU logos. (b) Sheet resistance versus the number of bending cycles of a typical PEDOT:PSS/CuNW film on PET substrate (bending radius  $\sim 5$  cm).

**3.3 Composite electrodes with CuNW/rGO** A major challenge for CuNW films is they oxidize readily, thus decreasing the surface conductivity of the electrode over time. Passivation of these transparent electrodes is therefore critical, even when the TCE is encapsulated within a device, due to risk of oxidation or impurity diffusion from the active layer. In an attempt to create

effective passivation layers, we used pristine graphene platelets as well as rGO platelets, using the deposition methods described above. Producing a high-quality large-area sheet of graphene using vapor phase methods can be economically prohibitive and requires substantial process optimization, but *in situ* reduction of GO platelets to produce a thin protective graphene layer over our spray-coated CuNWs is both cost-effective and rapid.

The GO platelets purchased from Graphene Supermarket have lateral size of  $\sim 5 \mu\text{m}$ , with 80% of the platelets being monolayer. GO platelets were separated from the stock solvent via centrifugation and dispersed in IPA at a concentration of 0.02 mg/ml. Spray-coating this suspension of GO yielded a homogeneous and continuous thin film. Subsequent reduction of GO is necessary for restoring its electrical conductivity.[3], [31] After spraying CuNWs and GO, the samples were annealed in a forming gas environment at 200 °C for 1 hour. The reduction of GO could be visually identified by the color change from light brown to black. To further investigate the reduction of GO to rGO, Raman shift was measured on spray-coated GO thin film and rGO thin film (reduced in the same condition described above), and they are presented in Fig. 2.7a. It is seen that the G band peak has shifted from  $1598 \text{ cm}^{-1}$  to  $1591 \text{ cm}^{-1}$  after the reduction. The peak intensity ratio between D band and G band is also reduced, indicating the partial reduction of GO to rGO. The SEM image in Fig. 2.7b shows that nanowires are covered with a uniform and continuous rGO coating. Small cracks are observed in the SEM images (for instance, in the red circle), but overall the nanowires are completely and homogeneously covered by rGO. The optical transmittance versus sheet resistance of the samples plotted in Fig. 2.7c shows that CuNW films suffer a loss of about  $\sim 4\%$  in transmittance when coated with rGO platelets. Despite the loss of optical transmittance, sheet resistances as well as standard deviation of measurements have been significantly lowered, resulting in a more uniform electrical conductivity across a given sample.

The improvement of conductivity is likely because of the two-dimensional rGO sheets bridging the gaps between disconnected or non-overlapping nanowires, thus creating additional pathways for the conduction electrons. Interestingly, if we reverse the order of deposition (that is, spray-coat the substrate with GO platelets first, followed by CuNWs) and anneal the sample under the same conditions, we find that the sheet resistance is considerably lowered while the optical transmittance remains the same. The samples prepared in the reversed order show  $R_s = 5.9 \pm 2.1 \text{ } \Omega/\text{sq}$  with  $T_{550} = 83.7\%$ . A SEM image showing such a configuration is shown in Fig. 7d.

We are uncertain as to what has caused this interesting improvement in conductivity. It is conceivable, of course, that CuNWs form a better ohmic contact with our 4-point probe than does the rGO film, hence the lowered values of sheet resistance when the probe is in direct contact with the nanowires.

The optical transmittance spectra for both CuNW and hybrid CuNW/rGO samples are shown in Fig. 2.8a. It is seen that the CuNW and the CuNW/rGO hybrid TCE both have relative flat transmittance over the visible and NIR range. It is also notable that the CuNW/rGO sample has slightly higher haze value ( $\sim 6\%$ ) than the CuNW sample ( $\sim 4\%$ ).

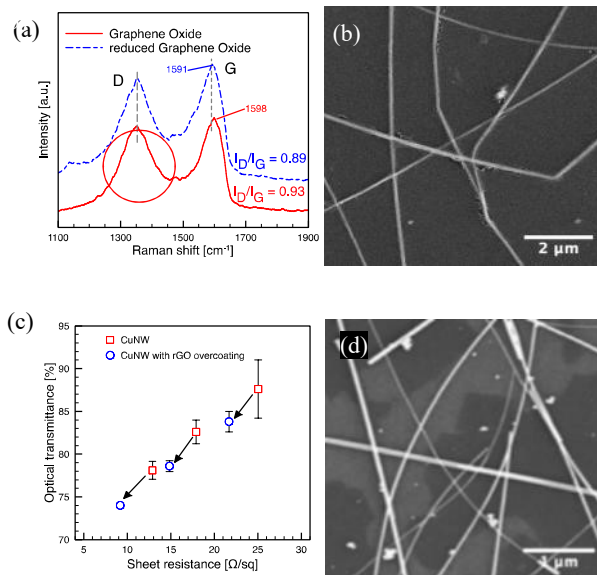


Figure 2.7. (a) Raman spectroscopy of GO and rGO thin films. (b) SEM image of CuNWs buried under homogeneous rGO overcoating. Small cracks are observed in the marked red circle. (c) Optical transmittance at 550 nm versus the sheet resistance of samples of bare CuNW (red) and rGO-covered CuNW (blue), both on glass substrates. (d) SEM image of CuNWs spray-coated over one or more layers of rGO platelets.

To test the durability of both CuNW TCE and CuNW/rGO hybrid TCE, the samples were placed in an enclosed environment with 80% relative humidity at 80 °C. The sheet resistances were measured every 12 hours over 2 days and plotted in Fig. 2.8b. No change was observed in the optical transmittance of the samples after the exposure. However, the sheet resistance of the bare CuNW TCE is seen to be nearly doubled, while those of the CuNW/rGO hybrid TCE remains essentially intact. Another durability test was carried out in an ambient environment over a course of 30 days. As seen in Fig. 2.8c, there is an increase of  $R_s$  for both CuNW and CuNW/rGO samples in the first 5 days; afterward, while the sheet resistance of the bare CuNW sample continuously increases, over the course of the experiment, the measured resistance of the CuNW/rGO remains stable. These tests highlight the importance of rGO over-coating as an approach to impact the longevity of the CuNW TCE.

To enable performance comparison of the various TCEs, the ratio of DC conductivity to optical conductivity is commonly used as a key figure of merit (FOM).[79] The following equation relates the transmittance of the film to its sheet resistance:

$$T = \left(1 + \frac{Z_0}{2R_s} \frac{\sigma_{op}}{\sigma_{DC}}\right)^{-2}.$$

Here  $\sigma_{op}$  is the optical conductivity and  $\sigma_{DC}$  is the DC conductivity. Using the above relationship,  $\sigma_{DC}/\sigma_{op}$  is calculated and summarized in table 2.1 and plotted in Fig. 2.9.

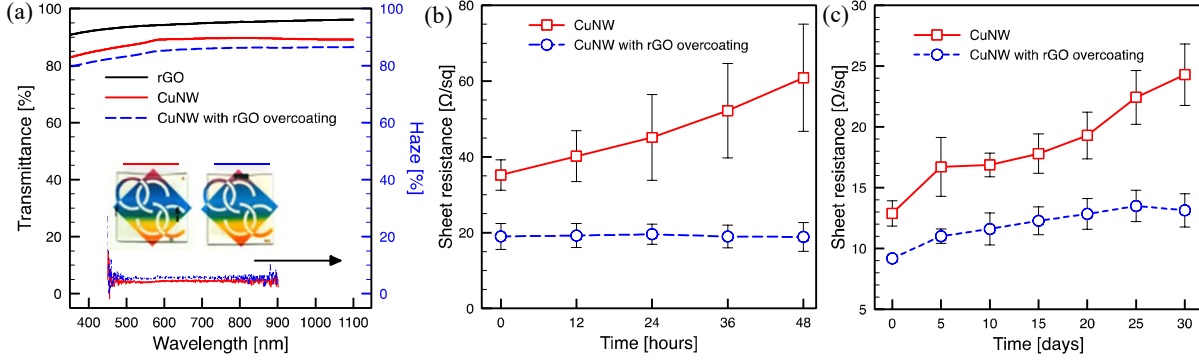


Figure 2.8. (a) Optical transmittance spectra and haze of rGO thin film (black) CuNW (red) and CuNW/rGO (blue) on glass substrates. The inset shows photographs of the corresponding samples placed over OSC logos. (b) Durability test of CuNW (red) and rGO-coated CuNW (blue) TCEs under with 80% relative humidity at 80 °C temperature. (c) Durability test of CuNW (red) and rGO-covered CuNW (blue) TCEs under ambient conditions over the course of 30 days.

Samples	$R_s(\Omega/\text{sq})$	$T_{550}(\%)$	$\sigma_{DC}/\sigma_{op}$
CuNW	23.1	87	113
PEDOT:PSS/CuNW	25	84.2	84
CuNW beneath rGO	21.7	83.8	94
CuNW over rGO	5.9	83.7	343
CuNW (Ref. 15)	51.5	93.1	101
CuNW beneath rGO (Ref. 19)	34	80	47

Table 2.1. Performance evaluation of our TCEs compared to those reported in the literature.

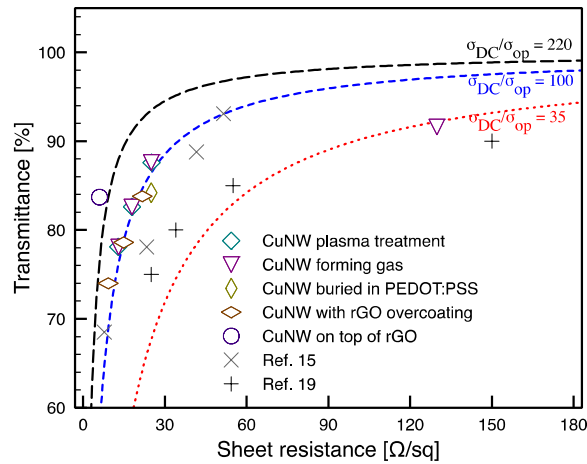


Figure 2.9. Optical transmittance versus sheet resistance of all TCEs fabricated in the present work. The three lines represent  $\sigma_{DC}/\sigma_{op}$  values of 35, 100, 220 as shown.

## 2.4 CONCLUSIONS

In this work, we have synthesized copper nanowires with ultra-high aspect ratio ( $L/D \approx 1600$ ) via a solution process and deposited a homogeneous network of these nanowires on glass substrates using a spray-coating technique. Optimal conditions for two annealing methods, thermal annealing and plasma treatment, have been determined for the fabricated CuNW films. The optimized CuNW-based TCEs are subsequently combined with PEDOT:PSS and rGO in order to reduce surface roughness and improve durability. Our fabricated TCEs should be suitable for a wide range of opto-electronic applications.

## CHAPTER 3

# SOL-GEL DEPOSITED ALUMINUM-DOPED AND GALLIUM-DOPED ZINC OXIDE THIN-FILM TRANSPARENT CONDUCTIVE ELECTRODES WITH A PROTECTIVE COATING OF REDUCED GRAPHENE OXIDE

### 3.1 INTRODUCTION

Transparent conductive electrodes (TCEs) are crucial components of opto-electronic devices such as thin film photovoltaic modules[3], [5], [80] and touch-screen displays[81], [82]. Among the existing materials, indium tin oxide (ITO) is the most common commercially viable TCE, owing to its good visible light transmittance and excellent electrical conductivity[83]–[85]. However, the diminishing indium supply of the world may not be able to meet the rapidly growing demand for TCEs. In recent years, thin films of zinc oxide (ZnO) doped with n-type dopants have been considered as promising substitutes for the ITO material. In particular, aluminum-doped zinc oxide (AZO) and gallium-doped zinc oxide (GZO) have been extensively studied as suitable TCEs for a wide variety of applications. These thin-film electrodes can be deposited via a number of different techniques such as spray pyrolysis, chemical vapor deposition[86], molecular beam epitaxy[87], sputtering[88]–[93], and sol-gel process[94]–[99]. Long-term stability in ordinary as well as harsh environments is necessary for successful commercialization for essentially all applications. However, the electrical conductivity of AZO and GZO thin films suffers from material degradation when these films are exposed to air ambient or harsher environments[89], [90]. Many approaches have been proposed and investigated by various researchers to improve the stability of AZO and GZO thin films under adverse conditions[100], [101]. However, to our knowledge, no one has reported the stability of AZO or GZO thin films protected by a cover layer of reduced graphene oxide (rGO).

In this work, we deposited AZO and GZO thin films on glass substrates using the sol-gel process, and applied plasma treatment to the deposited films to improve the electrical conductivity. More importantly, to address a well-known degradation issue these ZnO-based thin film TCEs suffer, we deposited layers of reduced graphene oxide (rGO) on top of our plasma-treated AZO and GZO films as passivation coating layers, and observed significant improvements in stability in air ambient as well as in a harsh environment.

### 3.2 METHODS

The deposition and annealing of AZO and GZO thin films is described in our previous work[26]. In brief, equimolar mixtures of diethanolamine (DEA) and zinc acetate are dissolved in 2-Methoxyethanol at a concentration of 0.5 M. Subsequently,  $\text{Al}(\text{NO}_3)_3$  or  $\text{Ga}(\text{NO}_3)_3$  is added to the solution at 2 or 1 atomic percent (at.%) to  $\text{Zn}^{2+}$  (e.g.  $[\text{Al}]/[\text{Al} + \text{Zn}] = 2\%$  or  $[\text{Ga}]/[\text{Ga} + \text{Zn}] = 1\%$ ), and the solution is stirred for 1 hour. The precursor solutions are aged for at least 24 hours before spin-coating. The thin films are deposited by repeating the combination of spin-coating and pre-annealing processes. After the films are deposited, they are exposed to low-pressure (i.e., below 5 torr) air plasma in a plasma-cleaner (PLASMA-PREEN-II-862) for 10 minutes.

In order to deposit the rGO over-coating, an aqueous suspension of graphene oxide (GO) platelets with 0.2 mg/ml concentration was spin-coated (at 1000 rpm for 45 seconds) atop our sol-gel deposited and plasma-treated AZO and GZO films. Following the spin-coating of GO platelets, the samples were annealed in forming gas environment at 180 °C for 1 hour to (partially) reduce the GO material. The sheet resistance of our samples was measured by the 4-point probe method using a Keithley 2400 Source Measurement Unit. Optical transmittance was measured using a Cary-3000 spectrophotometer, with the bare glass substrate used as baseline. Film thickness was measured by a Veeco DEKTAK 150 profilometer.

### 3.3 RESULTS

In our previous work[102], we demonstrated that AZO and GZO thin films prepared by the sol-gel process have extremely poor electrical conductivity ( $> 200 \text{ M}\Omega/\text{sq}$ ) before plasma treatment. However, after plasma treatment, these AZO and GZO films exhibit sheet resistances as low as  $200 \text{ }\Omega/\text{sq}$  and  $130 \text{ }\Omega/\text{sq}$ , respectively. In addition, our plasma-treated AZO and GZO films have over 90% optical transmittance across the visible and in the near-infrared range of wavelengths. A comparison of the various parameters of our sol-gel deposited and plasma treated thin films versus those reported in the literature is given in Table 3.1.

Material	Film thickness (nm)	T (%)	Rs ( $\Omega/\text{sq}$ )	Annealing method	Reference
AZO (2 at%)	330	$> 92$	200	Plasma treatment	This work
AZO (1 at%)	313	$> 80$	130	500 °C in air	[18]
AZO (2 at%)	200	$\sim 90$	2200	Laser irradiation	[19]
AZO (1 at%)	150	$> 85$	4400	650 °C in air	[23]
GZO (1 at%)	353	$> 94$	130	Plasma treatment	This work
GZO (2 at%)	65	91.5	$4.3 \times 10^7$	500 °C in air	[20]
GZO (3 at%)	200	$> 80$	950	IR lamp + 600 °C in vacuum	[21]
GZO (1 at%)	200	$\sim 85$	$2.1 \times 10^7$	550 °C in air	[22]
GZO (1.5 at%)	200	$> 85$	3300	650 °C in air	[23]

Table 3.1. Parameters of sol-gel deposited AZO and GZO thin films

Improvement in the electrical conductivity of our plasma-treated aluminum-doped and gallium-doped ZnO thin-film samples was accompanied by a change in the morphology of these samples. The scanning electron microscope (SEM) images of our AZO and GZO films, both before and after plasma treatment, are shown in Fig.3.1. It is seen in Figs.(3.1a) and (3.1b) that the AZO/GZO crystalline nanoparticles with sharp and clear boundaries are individually distinguishable before plasma treatment, whereas the plasma-treated samples shown in Figs.(3.1c) and (3.1d) have sintered and inter-diffused nanoparticles across the film's surface. During the treatment, the energetic plasma partially melted and merged the nanometer-sized particles and

made the thin film much more continuous. It is this sintering of the nanoparticles that we believe to be responsible for the improvement of the electrical conductivity of our plasma-treated samples.

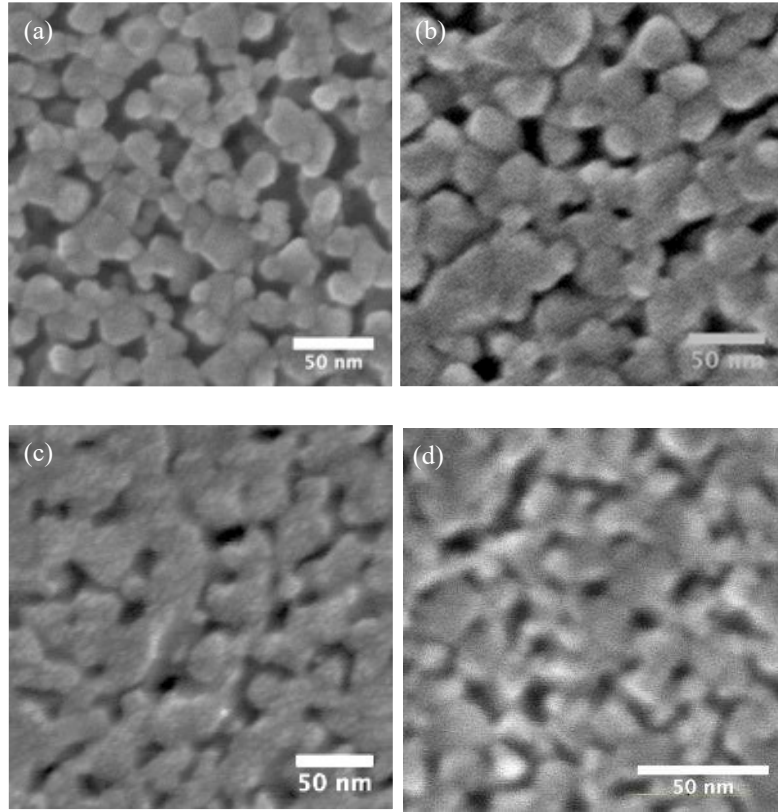


Figure 3.1. SEM images of (a) AZO and (b) GZO films before plasma treatment; the corresponding images after plasma treatment are shown in (c) and (d).

Previous work has shown degradation of ZnO, AZO, and GZO films due to exposure to heat and/or humidity[89], [90]. This is true of sol-gel deposited as well as sputtered films, even though the latter typically have a more compact structure and are consequently more stable than the former in hot/humid environments[101]. In our previous work[13], we have shown that a reduced graphene oxide (rGO) thin film can protect copper nanowires from degradation caused by heat and moisture. In an attempt to improve the stability of our ZnO-based thin-film samples, we spin-coated graphene oxide (GO) platelets in the form of a passivation layer on top of the plasma-treated AZO and GZO films and, subsequently, reduced the GO film in a forming gas (5% H<sub>2</sub> +

95% N<sub>2</sub>) environment at moderate temperatures (180 °C) for 1 hour. The effectiveness of partially reducing GO by this particular process has been discussed in our previous work[13]. As can be seen in Fig.2, the resulting films (both AZO and GZO) had slightly lower optical transmittance due to the presence of the rGO coating. The sheet-resistance of the samples after passivation with the rGO layer, however, remained essentially the same as that before passivation (< 200 Ω/sq).

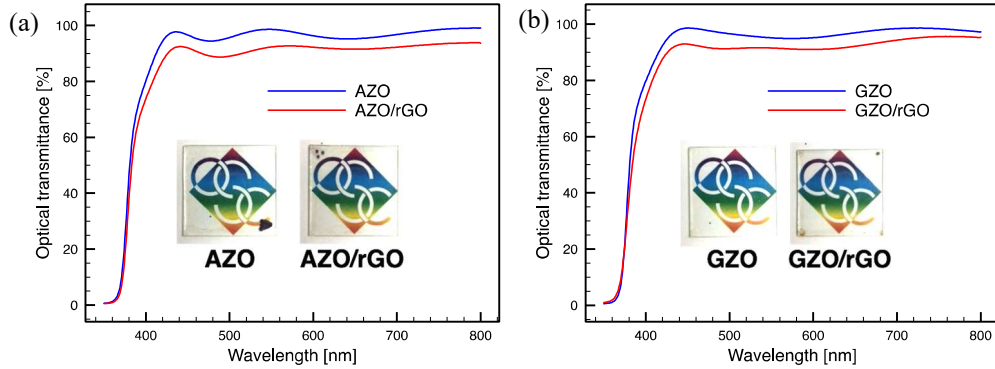


Figure 3.2. Optical transmittance spectra of sol-gel-deposited and plasma-treated thin film TCEs across the visible and near-infrared range of wavelengths. (a) Transmittance spectra of AZO and passivated AZO/rGO samples fabricated on glass substrates; the inset shows photographs of both samples placed over the OSC logo. (b) Transmittance spectra of GZO and passivated GZO/rGO samples fabricated on glass substrates; the inset shows photographs of both samples placed over the OSC logo.

To test the effectiveness of the rGO coating as a passivation layer, we stored the samples in an environment with 50% relative humidity at room temperature for a period of 30 days. The sheet resistances of the samples were measured during the test period and normalized to the original values of as-fabricated samples. Normalized plots of sheet resistance versus time for these samples are shown in Fig.(3.3a). On one hand, the electrical conductivity of AZO and GZO samples without rGO coating is seen to have degraded rapidly during the first seven days, and continued to degrade afterward, resulting in a 50-fold increase in their sheet resistance. On the other hand, samples with rGO passivation coating exhibit significantly improved stability over the entire 30-day period; in particular, the sheet resistance of the GZO/rGO sample at the end of the month is less than double its initial value. Another test was conducted under a harsh environment

with 80% relative humidity at 80 °C for a period of 48 hours, and the sheet resistance was monitored every 12 hours; the results are shown in Fig.(3.3b). Once again, the stability of rGO-coated samples is seen to have improved substantially relative to that of the uncoated samples. Whereas the un-protected AZO and GZO samples showed a 25-fold and 15-fold increase of sheet resistance, respectively, the sheet resistance of the passivated AZO/rGO sample had less than tripled during the same period, while that of the GZO/rGO sample remained essentially intact.

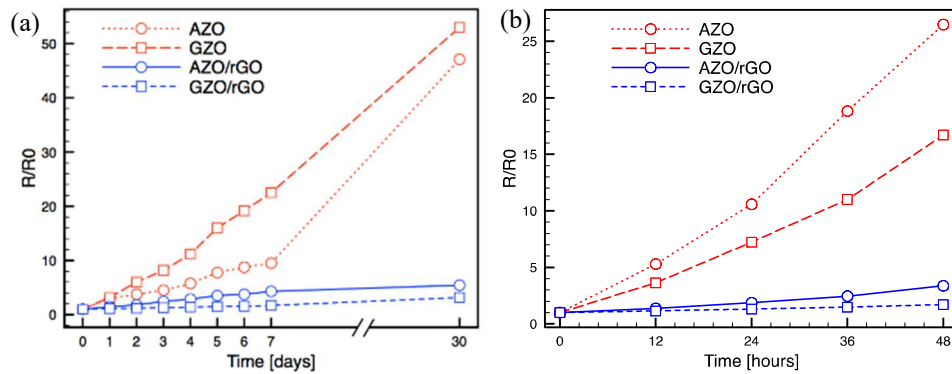


Figure 3.3. (a) Normalized sheet resistance versus the time (in days) during which the samples were exposed to 50% relative humidity at room temperature. (b) Normalized sheet resistance versus the time (in hours) during which the samples were exposed to 80% relative humidity at 80 °C.

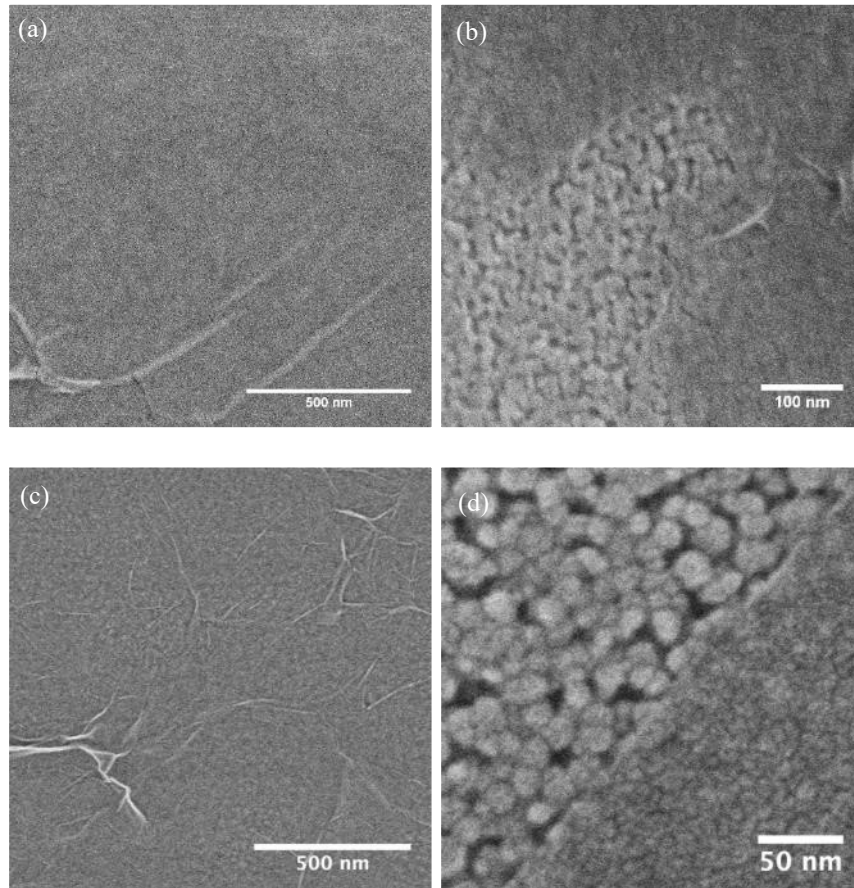


Figure 3.4. SEM images of: (a) An rGO layer fully covering an AZO thin film sample. (b) An rGO layer partially covering an AZO thin film sample. (c) An rGO layer fully covering a GZO thin film sample. (d) An rGO layer partially covering the lower-right half of a GZO thin film sample.

The SEM images in Fig.3.4 show the coverage of rGO on the surface of the AZO or GZO samples. Fig.(3.4a) is a representative view of a typical AZO/rGO sample, in which the rGO passivation layer almost completely covers the surface of the AZO film. The bright ridges seen in this SEM image are wrinkles in the rGO layer. The full and uniform coverage by rGO across the surface protects the sample against moisture attacks. Upon closer inspection, however, one finds isolated spots where the AZO surface is not seamlessly covered. Fig.(3.4b) shows an instance where only the lower-right-half of the imaged region is protected by the rGO layer. Similarly, a

GZO thin film fully covered by rGO layer is shown in Fig.(3.4c) and a half-covered region of a GZO/rGO sample is shown in Fig.(3.4d).

### 3.4 CONCLUSION

We employed the conventional method of sol-gel deposition to fabricate AZO and GZO thin film TCEs on glass substrates, and applied plasma treatment to these films following deposition. Our best samples are a 1 at.% GZO with sheet resistance  $R_s < 130 \Omega/\text{sq}$ , and a 2 at.% AZO with  $R_s < 200 \Omega/\text{sq}$ . The AZO and GZO samples prepared in this work both exhibit over 90% optical transmittance across the visible and near-infrared wavelength range. We imaged the fabricated TCEs using a scanning electron microscope, and observed surface morphology changes due to plasma treatment, which may explain the significant enhancement of the electrical conductivity over those samples that were treated solely by thermal annealing. Lastly and most importantly, we deposited an rGO protective layer over our plasma-treated AZO and GZO films for purposes of passivation. The smooth and continuous rGO layer almost completely passivates the AZO and GZO thin films. The rGO coated TCEs exhibit substantial improvement in sample stability in both air ambient and harsh (i.e., 80% relative humidity at 80 °C) environments.

## CHAPTER 4

# HYBRID TRANSPARENT CONDUCTIVE ELECTRODES WITH COPPER NANOWIRES EMBEDDED IN A ZINC OXIDE MATRIX AND PROTECTED BY REDUCED GRAPHENE OXIDE PLATELETS

### 4.1 INTRODUCTION

Transparent conductive electrodes (TCEs) usually come in the form of thin films, and have both high optical transparency (in a desired range of wavelengths) and high electrical conductivity.[102] Although they are rarely seen as independent devices in their own right, TCEs have been integrated into the fabric of a vast array of common opto-electronic devices and systems. For instance, liquid crystal displays (LCDs) currently provide the largest single market for TCE products.[103]–[105] As an example, recall that a sheet of TCE resides beneath the touch-screen display of every iPhone in use today. Another example is provided by organic and DSSC photovoltaic modules, each of which requires a TCE as a window to transmit visible and near infrared sunlight to the solar-active material, and then to collect and conduct the photoelectric current that is generated within the cell.[106]–[110]

In the aforementioned applications, indium tin oxide (ITO) has always been favored as the TCE material due to its superior optical transmittance and excellent electrical conductivity.[85], [111] In addition, the physical and chemical stability of ITO and its endurance in the face of environmental adversity have been decisive factors in its widespread commercial success. However, ITO has its own drawbacks, the most prominent of which being the fact that indium is a scarce element whose worldwide supply is not expected to meet the rapidly growing market demands. According to a report from the U.S. Geological Survey's Mineral Resources Program,

the annual average price of indium from U.S. producers has risen from \$565 to \$735 per kilogram over the past 5 years. Another shortcoming of ITO is its mechanical inflexibility, considering that a number of new technologies such as wearable electronics require the transparent electrodes to be flexible or even deformable.[35], [112]Although ITO can be deposited on flexible substrates such as polyethylene terephthalate (PET), its electrical conductivity rapidly degrades and eventually disappears after multiple bending cycles, especially for small bending radii. The bottom line is that, while ITO has successfully met the stringent requirements of existing applications, finding suitable substitutes for ITO will be crucial for the continued growth and expansion of the opto-electronics industry.

Several materials have been developed and studied in the past decade as candidates to replace ITO: metal mesh[80], metallic nanowires such as silver nanowires (AgNWs)[35] or copper nanowires (CuNWs)[112], conductive metal oxides such as fluorine tin oxide (FTO)[113], zinc oxide (ZnO)[13], and doped zinc oxide[104], and carbonous materials such as carbon nanotubes[103] and graphene[106]. Each of these emerging materials has its own advantages and disadvantages. For example, CuNWs can be synthesized fairly easily and inexpensively in large quantities, but they lack long-term stability; both zinc oxide and graphene can be highly transparent in the visible wavelength range, but their sheet resistance is inferior to that of ITO.

Next generation opto-electronic devices require TCEs to not only have good optical transmittance and sheet resistance, but also possess properties such as flexibility, stability in harsh environments, and longevity. Hybridization can help overcome the shortcomings of the new classes of TCE materials by combining their strengths. In the present work, we synthesized CuNWs via a one-pot solution method, and used a traditional sol-gel deposited zinc oxide (ZnO) thin film to embed and anchor the CuNWs onto the substrate. These transparent conductive

electrodes, having sheet resistances in the range of 10 to 50  $\Omega/\text{sq}$ , exhibit excellent electrical conductivity while their optical transmittance across the visible spectrum exceeds 75%. In order to improve the long-term stability of our TCEs in harsh environments, we applied a reduced graphene oxide (rGO) cover layer via spin-coating followed by annealing in a forming gas atmosphere. Our rGO-coated samples exhibit significant improvement over unprotected samples as demonstrated by their stable sheet resistance in a harsh environment (85% relative humidity at 85°C) during several days of testing.

## 4.2 METHODS

**4.2.1 Fabrication of CuNW TCE** Details of the synthesis of CuNWs have been described in our previous publication.[13] CuNW-based TCEs can be fabricated on rigid glass as well as flexible polyethylene naphthalate (PEN) substrates. Before deposition, the glass substrates were cleaned with piranha solution and stored in DI water. PEN substrates were cleaned using an organic solvent (IPA) and DI water.

To fabricate the CuNW TCEs, clean substrates were affixed to a hot-plate maintained at 60 °C. An airbrush was used for spray-coating the desired volume of CuNW solution onto the substrate. Subsequent to the deposition of nanowires, the samples were placed in a plasma-cleaner and exposed to air plasma for 100 seconds to weld the nanowires at their crossing points in order to bring about electrical conductivity across the sample.

**4.2.2 Sol-gel deposition of zinc oxide thin film** The zinc oxide (ZnO) precursor is prepared by mixing diethanolamine, zinc acetate and 2-methoxyethanol. The precursor mixture was vigorously stirred to achieve a homogeneous solution. Before deposition, the solution was aged for at least 24 hours. Subsequent to aging, the ZnO precursor solution was pipetted onto the CuNW samples and spun at 1000 rpm for 45 seconds, followed by another round of spinning at 4000 rpm for 15

seconds. After the deposition, the CuNW/ZnO thin film was annealed in a forming gas environment (95% N<sub>2</sub> + 5% H<sub>2</sub>) at a moderate temperature for 1 hour.

**4.2.3 Deposition and reduction of graphene oxide (GO) platelets** Graphene oxide (GO) solution with concentration of 6 mg/ml was purchased from Graphene Supermarket. Before use, it was diluted to 0.2 mg/ml with IPA and sonicated in a water bath. GO was spin-coated on bare CuNW TCEs for purposes of comparing their scotch-tape-resistance, and also for passivation of CuNW/ZnO thin films. The spin-coating parameters were the same as those used for coating ZnO thin films. After the GO deposition, the samples were annealed in a forming gas environment at 250 °C for 1 hour, which resulted in partial reduction of the graphene oxide platelets.

**4.2.4 Characterizations** We measured the sheet resistance of our samples using the 4-probe method with a Keithley 2400 unit. Optical transmittance spectra were measured using a Cary-3000 UV-Vis spectrometer and corrected with blank substrates as baselines. Scanning Electron Microscope (SEM) images were taken using a Hitachi 4800 SEM. Grazing angle SEM images were taken by mounting the samples vertically and tilting the stage by 5°.

### 4.3. RESULTS AND DISCUSSIONS

In our previous work[13], we demonstrated that the synthesized CuNWs have an average length of 70 μm and an average diameter of 45 nm. Depending on the amount of CuNW solution used during spray-coating, our fabricated TCEs exhibit a range optical transmittance and sheet resistance values, as shown in Fig.(4.1a). It is clearly seen that sheet resistance  $R_s$  and optical transmittance  $T$  have an inverse relationship. Our best CuNW TCE on a glass substrate has  $R_s = 22.4 \Omega/\text{sq}$  and  $T = 88\%$  at a wavelength of 550 nm. For a CuNW network deposited on a flexible PEN substrate, the sheet-resistance is seen in Fig.(4.1a) to have slightly increased to  $R_s = 36 \Omega/\text{sq}$ ,

while the optical transmittance remains essentially the same as that for the sample on a glass substrate. To demonstrate the flexibility of the CuNW TCE on a plastic substrate, we bent our samples, including CuNW and CuNW/ZnO, on PEN substrates with a radius of  $\sim 5$  mm in multiple cycles of compressing and stretching. As shown in Fig.(4.1b), the sheet resistance of the samples did not change much after 1000 bending cycles.

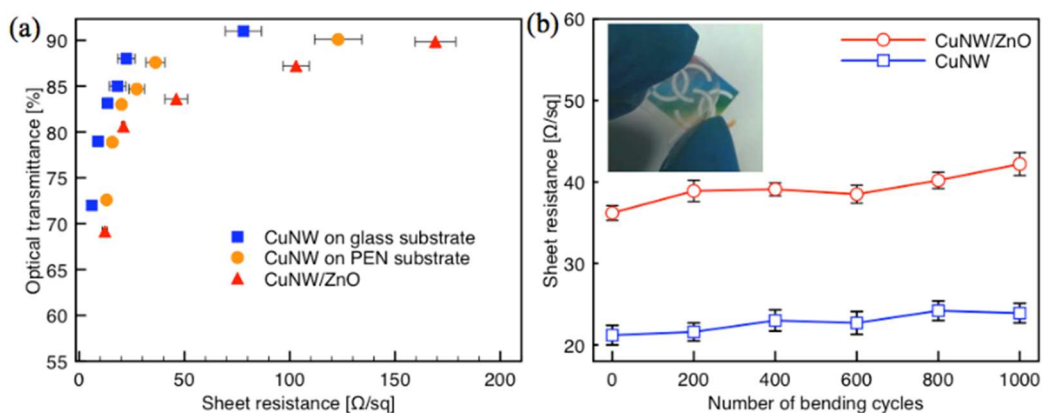


Figure 4.1. (a) Optical transmittance (at the wavelength of 550 nm) versus the sheet resistance for CuNW samples fabricated on glass substrates, on PEN substrates, and on glass substrates while embedded in ZnO. (b) Sheet resistance versus number of bending cycles of CuNW and CuNW/ZnO samples on PEN substrates. The inset is a photograph of a flexible sample of a CuNW TCE on PEN held over the OSC logo.

Although our CuNW TCEs have good sheet resistance and high optical transmittance, their adhesion to the substrate is rather weak. Figure (4.2a) shows photographs of two CuNW TCEs on glass substrates (one bare sample and one covered with rGO platelets) both before and after a scotch-tape peel test. It is seen that the right-half of the bare sample and the bottom-half of the rGO-coated sample (inside the yellow box, where the scotch tape was applied) are more transparent because the tape has effectively peeled off and removed the copper nanowires from the substrate. A subsequent measurement of sheet resistance also confirmed that the portion of the samples within the yellow boxes of Fig.(4.2a) had lost their electrical conductivity after the removal of the scotch tape.

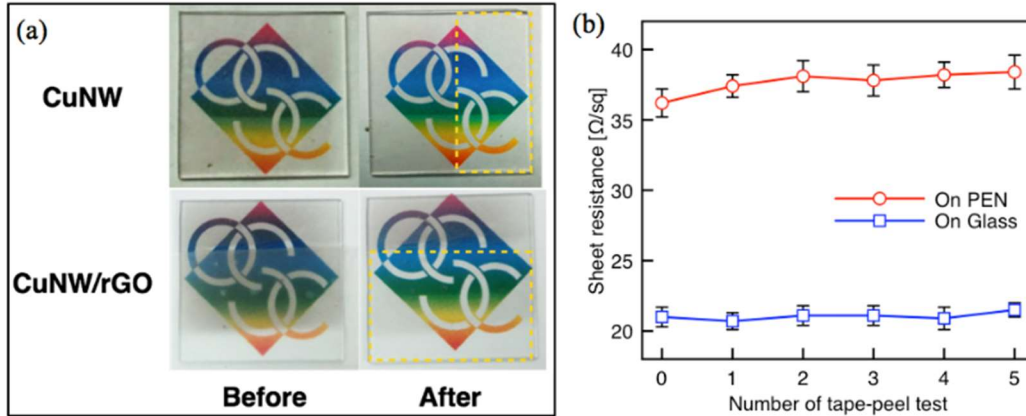


Figure 4.2. (a) Photographs of bare CuNW and CuNW/rGO samples before and after a scotch-tape-peel test; yellow boxes indicate the taped areas. (b) Sheet resistance of CuNW/ZnO samples on rigid glass substrates and also on flexible plastic (PEN) substrates versus the number of scotch-tape-peel tests. The embedding of the nanowire network within the ZnO matrix clearly improves the adhesion of CuNWs to the glass substrate.

In order to improve the adhesion of our CuNWs to the substrate, we deposited a coating/embedding layer of zinc oxide (ZnO) via the sol-gel deposition method. After the network of CuNWs on a glass substrate was plasma-treated, the ZnO precursor was cast onto the CuNWs and made to spread evenly using a spin-coater. The hybrid film was then annealed in a forming gas environment at a moderate temperature for 1 hour. The CuNW/ZnO film has slightly reduced transmittance compared to the bare CuNW sample, which can be readily inferred from the data plotted in Fig.(4.1a). However, the hybrid film now firmly adheres to the substrate, as confirmed by a repeated application of the scotch-tape peel test. As shown in Fig.(4.2b), the CuNW/ZnO TCE is mechanically strong, without suffering an appreciable loss of conductivity after five consecutive applications of the scotch-tape peel test. This enhancement in adhesion to the substrate was observed for both glass and flexible substrates. For a comparison, we deposited a graphene oxide (GO) thin film layer on top of the bare CuNW sample on glass, and proceeded to reduce the GO to form a protective coating of reduced graphene oxide (rGO) over the entire area of the sample. Figure (4.2a) reveals that the sample was still vulnerable to the tape test; upon removing the scotch-

tape, the bottom-half of the CuNW/rGO sample (inside the yellow box, where the tape was applied) had lost much of its nanowire network and, therefore, become non-conductive.

We imaged the bare CuNW sample as well as the CuNW/ZnO sample on a glass substrate using a scanning electron microscope (SEM). Images were captured in both frontal view and edge view (at 5° grazing angle). These images are shown in Fig.(4.3). Figures (4.3a) and (4.3b) show, respectively, the frontal and edge views of a bare CuNW film deposited on a glass substrate. The CuNWs are seen to be elevated slightly above the flat surface of the substrate, which, in all likelihood, is the cause for their poor adhesion to the substrate. In contrast, in Figs.(4.3c) and (4.3d), CuNWs are seen to be covered and anchored to the substrate by the ZnO thin-film; the surface of the hybrid film also appears to be smoother. Specifically, at the wire-wire junctions, the ZnO film appears to have flattened and smoothed the originally elevated surface of the CuNW network.

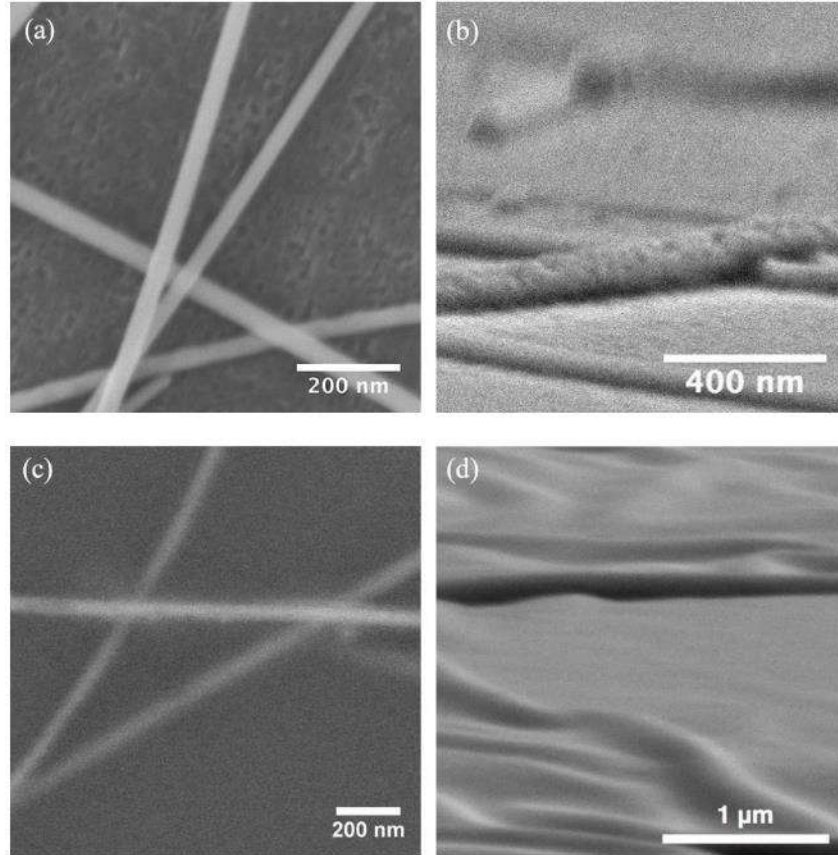


Figure 4.3. SEM images of bare CuNW and hybrid CuNW/ZnO thin films on glass substrates. (a) Frontal view of a bare CuNW sample. (b) Edge view (at 5° grazing angle) of the bare CuNW film. (c) Frontal view of a hybrid CuNW/ZnO thin-film sample. (d) Edge view (at 5° grazing angle) of the hybrid CuNW/ZnO sample.

With the CuNW network buried under the ZnO thin film, our TCEs are mechanically stable and resistant to scotch-tape peel. However, both CuNW and ZnO are known to degrade over time in air, and more drastically, in hot and humid environments. In our previous work[13], we have demonstrated the effectiveness of using an rGO layer as passivation for improving the lifetime of CuNW TCEs in harsh environments. The carbon atoms in a 2-D graphene sheet are about 1.42 Å apart, while the oxygen and water molecules are about 3.5 Å and 2.7 Å in diameter, respectively. That, we believe, is the reason why a graphene coating layer prevents the penetration of water and oxygen molecules. We thus prepared and tested CuNW/ZnO/rGO samples together with unprotected CuNW/ZnO samples on both glass and flexible substrates in a controlled environment

with 85% relative humidity at 85 °C for four days. Figure (4.4a) shows the optical transmittance spectra of CuNW, CuNW/ZnO, and CuNW/ZnO/rGO samples deposited on glass substrates. Since we are using rGO platelets that have a lateral dimension of several micrometers, a stack of several rGO layers is needed to produce a rather complete coverage of the CuNW/ZnO thin film underneath. This explains the loss of optical transmittance (upon addition of the rGO layer) that is greater than the typical 2.3% for single layered graphene; see Figure (4.4a). The sheet resistance of the samples was monitored and recorded at 12 hour intervals. Figure (4.4b) shows the change of the sheet resistance during the four-day period of the study. It is seen that, while the sheet resistance of the unprotected CuNW/ZnO film deteriorates substantially over time, the protected CuNW/ZnO/rGO sample remains quite stable, with only a slight increase observed in its sheet resistance after four days of exposure to the harsh environment.

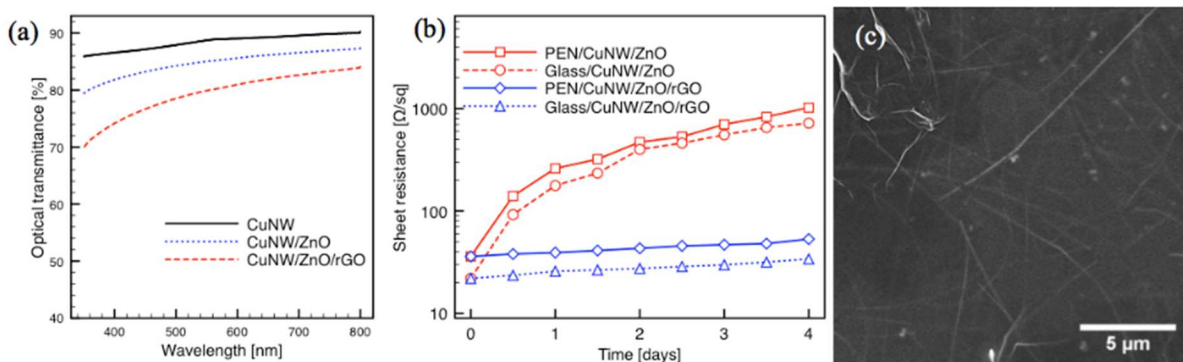


Figure 4.4. (a) Transmittance spectra of CuNW, CuNW/ZnO and CuNW/ZnO/rGO samples deposited on glass substrates. (b) Measured sheet resistance versus the number of days during which the samples were exposed to 85% relative humidity at 85 °C. The reduced graphene oxide (rGO) coating applied to the CuNW/ZnO film appears to prevent the penetration of moisture into the pores and cracks of the ZnO matrix, thereby prolonging the TCE's lifetime. (c) SEM image of a CuNW/ZnO/rGO sample showing embedded CuNWs beneath the surface, and wrinkles in the rGO layer in the upper left-hand corner of the imaged area.

Figure (4.4c) shows a frontal SEM image of a CuNW/ZnO/rGO sample. While the embedded CuNWs are visible beneath the surface of the ZnO film, the rGO platelets are seen to blanket the entire surface of the hybrid CuNW/ZnO sample. In the top-left corner of the image, a

few wrinkles are visible in the rGO layer. The rGO passivation prevents oxygen and moisture from attacking the nanowires through the pores (and occasional cracks) within the ZnO matrix, thereby improving the overall stability of the TCE in normal as well as harsh environments.

### **4.3 CONCLUSION**

We synthesized high aspect-ratio CuNWs via a solution process and deposited them on glass and PEN substrates to fabricate high performance TCEs. Zinc oxide and reduced graphene oxide were deposited in sequence to strengthen the thin film electrode and to improve its stability. Our best Glass/CuNW/ZnO/rGO hybrid thin film has  $R_s \sim 20 \Omega/\text{sq}$  and  $T \sim 79\%$  at a wavelength of 550 nm. In addition, our hybrid TCE is resistant to scotch-tape peel and is stable when exposed to high humidity at elevated temperatures.

## CHAPTER 5

### PEROVSKITE SOLAR CELLS

#### PEROVSKITE SOLAR CELL SYNTHESIS AND DEPOSITION

##### High temperature Perovskite Solar Cells for benchmark testing and troubleshooting

The initial perovskite investigated was the two-step perovskite using TiO<sub>2</sub> as the ETL and Spiro-MeOTAD as the HTL. The TiO<sub>2</sub> was initially deposited on ITO substrates because of availability, but later changed to FTO because of the high-temperature sintering TiO<sub>2</sub> requires. This sintering step is crucial to not only remove organic binders which prevent agglomeration during the deposition process, but also introduces “necking” of the TiO<sub>2</sub> particles which is crucial to electron transport through the semiconductor. While ITO has great sheet resistance (8-15 Ω/sq), it increases when annealed at temperatures greater than 200 °C [114], while FTO undergoes no sheet resistance change at 500 °C. This increase in sheet resistance translates to an increase in overall series resistance of the solar cell, which affects the fill factor negatively[115].

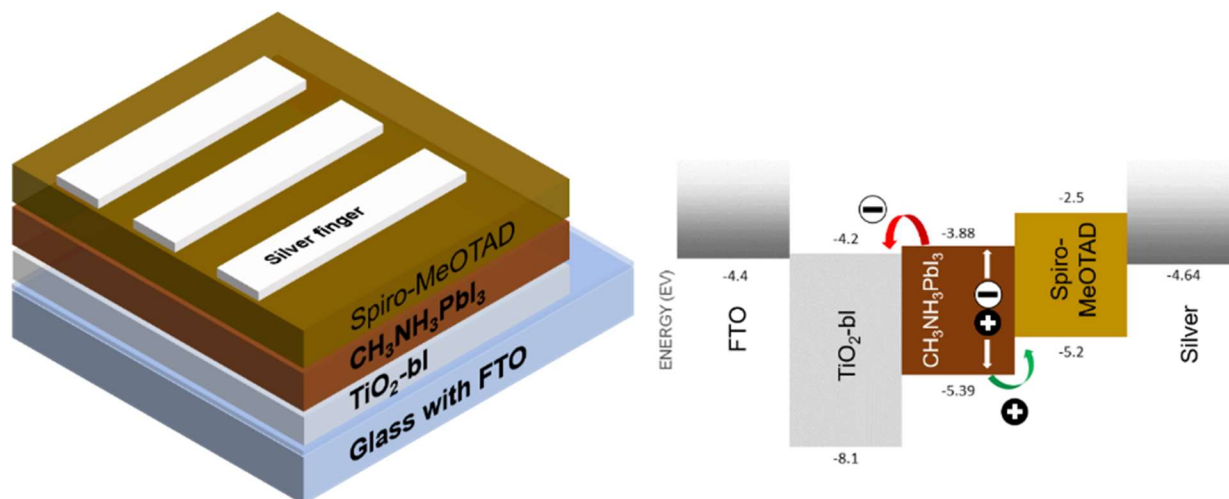


Figure 5.1. (left) Planar heterojunction perovskite solar cell architecture using a compact titanium dioxide layer as the ETL and Spiro-MeOTAD as the HTL. (right) Band diagram of the cell showing direction of electron and hole flow.

The  $\text{TiO}_2$  electron transport layer was synthesized (Appendix A.5) to reproduce reported recipes[116]–[119] that used both low and high temperature annealing steps. Both device architectures were taken for comparison purposes, as high-temperature  $\text{TiO}_2$  ETL had previously been reproduced in our work with DSSCs. The majority of the deposition steps (Appendix B.1) were conducted in a low humidity environment ( $< 35\%$ ), and the back electrode is evaporated using a shadow mask in an Edwards ebeam evaporator. Due to the instability of perovskite solar cells and the reversion of perovskite to lead iodide when exposed to humidity[29], [49], [54], [120], the cells were stored in a dessicator between testing.

All cells consistently underperformed in both voltage and fill factor compared to the literature records, while a current density of  $19.31 \text{ mA/cm}^2$  was achieved. This particular configuration is composed of a 50 nm layer  $\text{TiO}_2$  ETL, 200 nm perovskite layer, and 100 nm layer HTL and Ag electrode evaporated via ebeam (See Table 5.2). Average current density of these high-temperature-ETL cells were  $10.5 \text{ mA/cm}^2$ , and average open circuit voltage 414 mV. Due to the poor fill factor, power conversion efficiency was limited to  $\eta < 4\%$ .

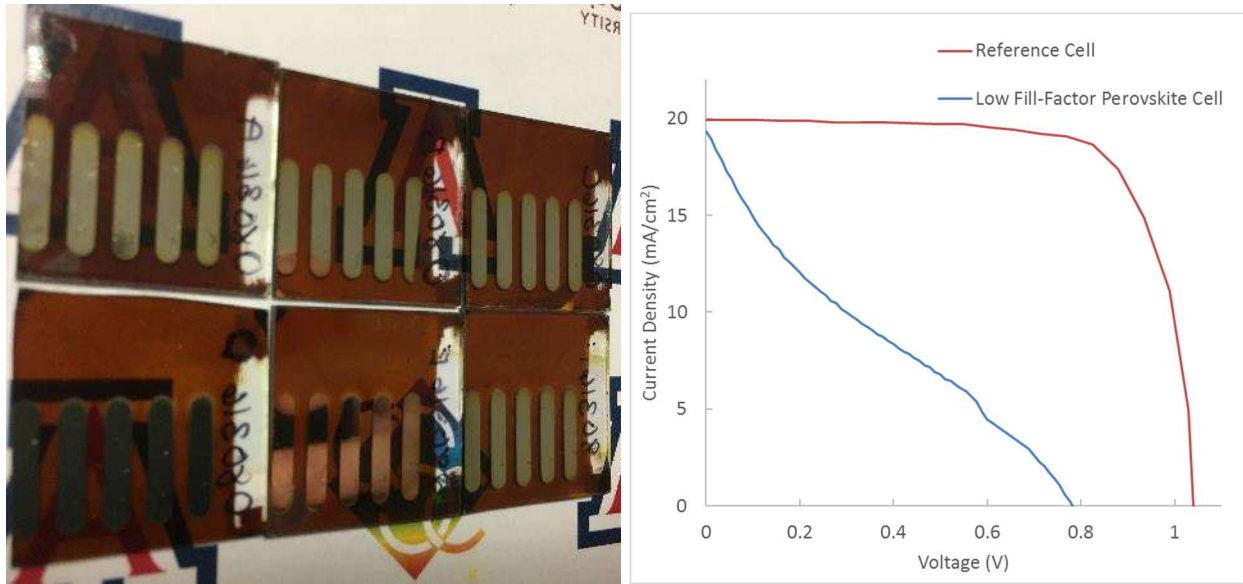


Figure 5.2. (left) Six finished perovskite cells on ITO substrates and finished with silver back electrodes. (right) IV graph for high temperature two-step perovskite solar cell showing extremely low fill factor, regardless of short circuit current. Reference cell based on average literature high performance perovskite cell.

This poor fill factor is understood to be a combination of factors, and the primary factor is the cells having a high series resistance and a low shunt resistance. A high series resistance results from poor contact between semiconductor layers and high resistance in the front or back electrode, while a poor shunt resistance is characteristic of a non-uniform perovskite layer with pinholes and defects which lead to recombination.[121], [122] Power conversion efficiency is dictated by the equation

$$\eta = \frac{J_{SC} \times V_{OC} \times FF}{P_{in}}$$

thereby limiting our cells' efficiencies predominantly due to significantly lower fill factor and slightly lower open circuit voltages.

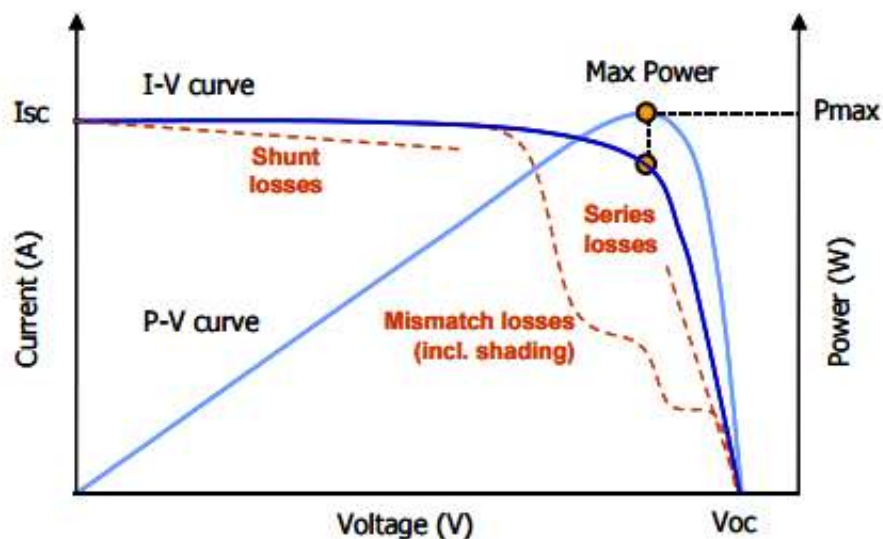


Figure 5.3. Diagram showing the effect of shunt losses and series losses in a solar cell.[122] In this diagram small effects of series and shunt resistance are shown, an order of magnitude small than the values in our cells.

Perovskite performance is known to be limited by the balance between shunt and series resistance, but not to the degree seen in our cells. A relatively thick HTL is required to prevent leakage through pinholes, but also increases the series resistance.[47] This effect is seen in all further perovskite cells presented in this thesis, an issue that was never rectified despite repeated attempts at optimization.

There is significant amounts of literature that discuss the recombination losses in perovskite, difficulty in depositing pinhole-free layers, and optimizing the electron and hole transport layers to achieve reproducible, high performance perovskite cells.[29], [54], [58], [123]–[130] To determine if the coverage in the fabricated cells was complete (ie pinhole-free), many characterizations of the perovskite active material were carried out and compared with literature reports.

The conversion of lead (II) iodide precursor to perovskite grains is typically observed in two-step depositions by the color change from bright yellow to shiny reddish-brown. In all two-step depositions we tested, the same transformation was seen, though the different methods differed in performance and under scrutiny with scanning electron microscopy (SEM).

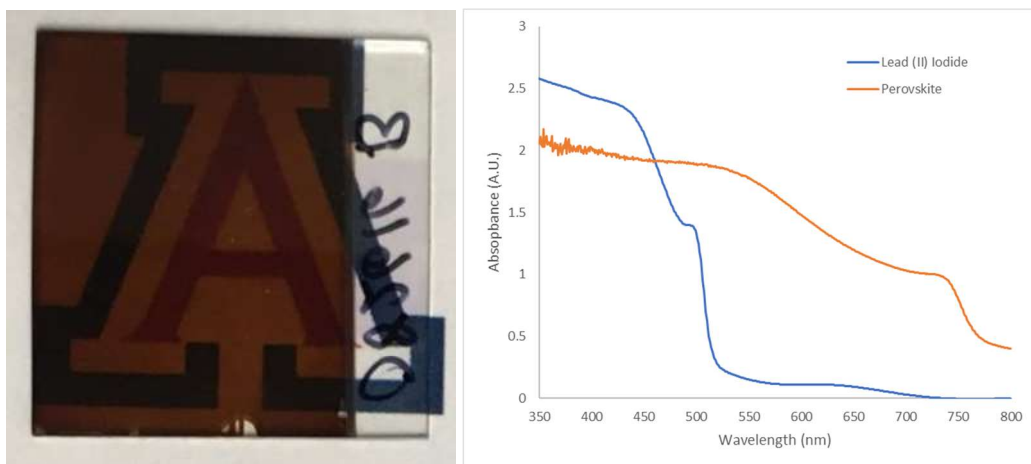


Figure 5.4. (left) Perovskite film formed on ITO substrate with  $\text{TiO}_2$  electron transport layer. ITO electrode contact can be seen on the right side of the glass substrate. (right) Absorption data of both  $\text{PbI}_2$  film and the resulting perovskite after dipping in MAI.

Absorption spectrum was measured before and after the conversion of  $\text{PbI}_2$  to perovskite, and in both cases matched reported behaviors, with the specific perovskite absorption dips at  $\sim 500$  nm and 750 nm observed.[131], [132] To confirm that the perovskite material was pure in composition and to gauge how much of the initial  $\text{PbI}_2$  was converting to perovskite, X-ray diffraction on perovskite films deposited on the front TCE (ITO) and  $\text{TiO}_2$  were carried out and evidence that complete consumption of the  $\text{PbI}_2$  precursor is shown.

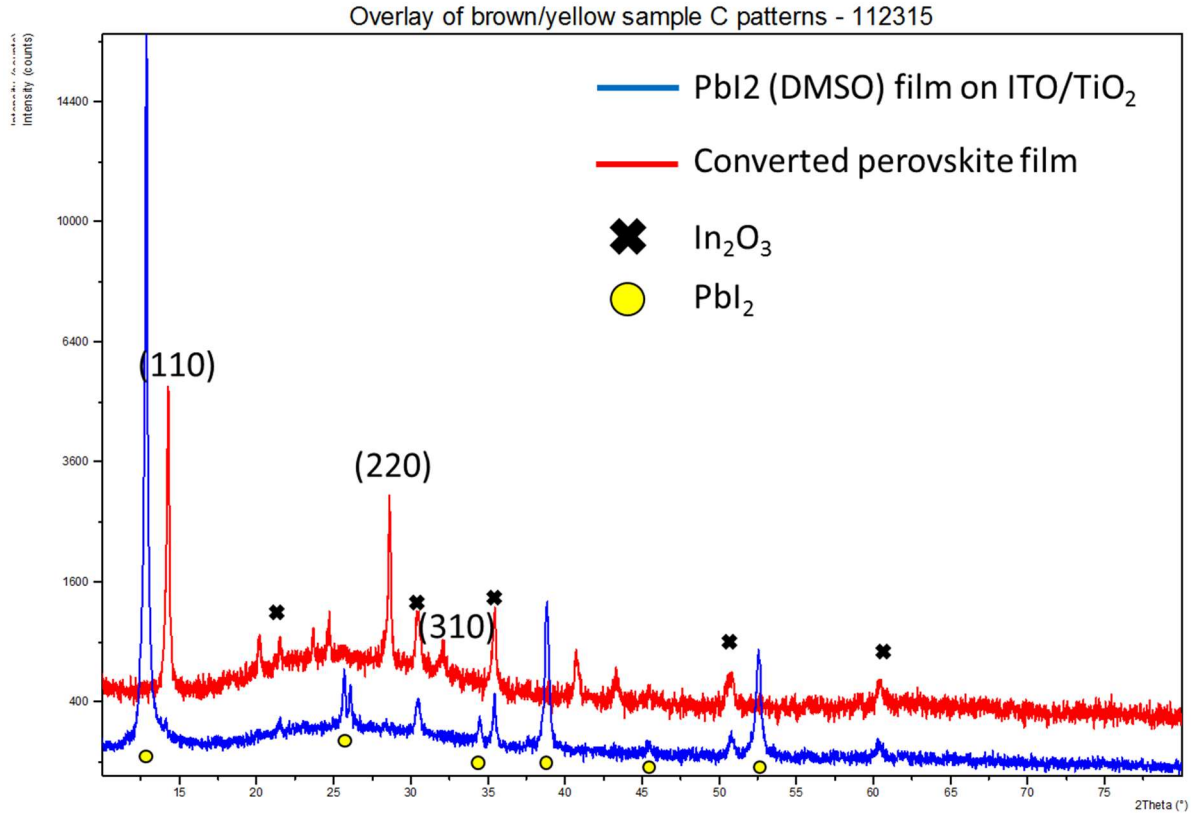


Figure 5.5. XRD graph showing peak shift from 12.3° to 14.08° (110 peak) consistent with perovskite conversion and elimination of PbI<sub>2</sub> precursor. ITO peaks are seen throughout both samples.

In the converted perovskite trace, the peak at 12° disappeared completely, replaced by three new peaks corresponding to the (110), (220), and (310) orthorhombic planes at 14.08°, 28.70° and 32.12° respectively. Under SEM, the change was also observed from PbI<sub>2</sub> to CH<sub>3</sub>NH<sub>3</sub>PbI<sub>3</sub> in addition to uniform layers with minimal pinholes.

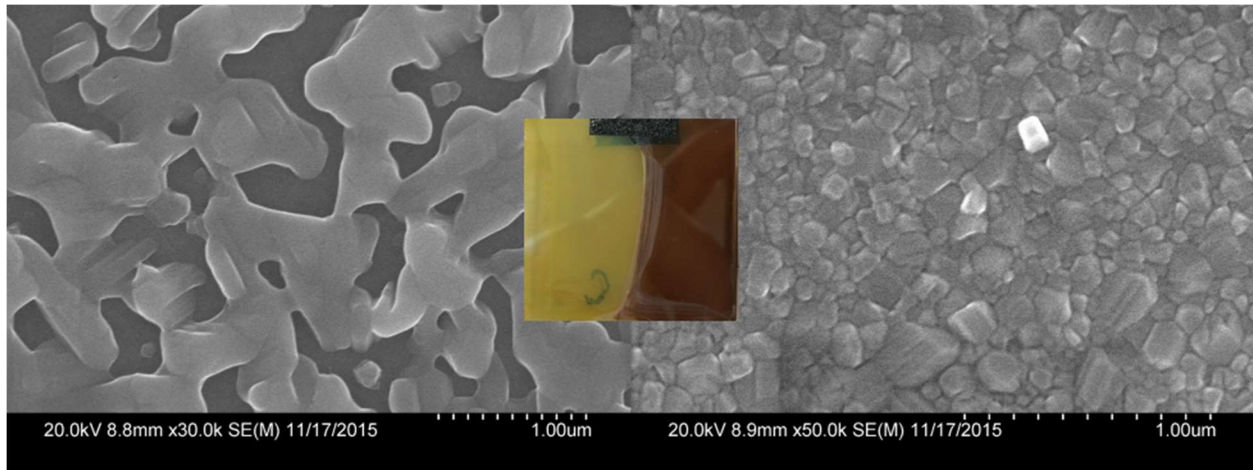


Figure 5.6. (left)  $\text{PbI}_2$  film deposited on  $\text{TiO}_2$  ETL. (right) Converted perovskite via dip-coating from the same substrate. (center) Photo of examined substrate showing half of it that has been dipped in MAI solution for 5 minutes.

SEM was also done on-edge to by cleaving completed cells to determine the thickness of deposited layers, though this method of imaging was difficult to reproduce. By changing the spin coater speed, temperature of precursor or concentration in solvent, some tuning of the thickness and smoothness of the layer could be achieved.

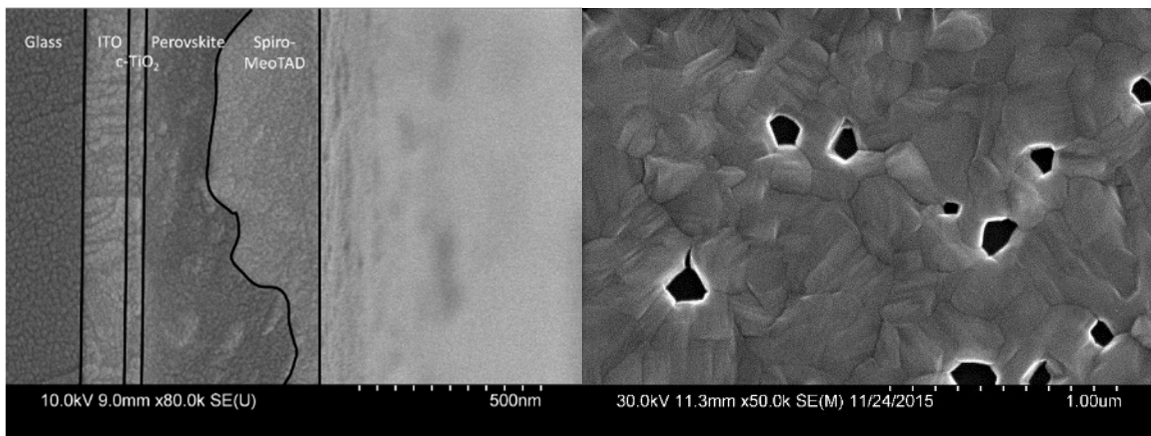


Figure 5.7. (left) On-edge scanning electron image of a cleaved perovskite solar cell, showing approximate layers of the thin film device. Total cell thickness is  $\sim 600$  nm. (right) Scanning electron micrograph of a perovskite film on top of ETL and ITO showing some pinholes in the layer.

Because of the thickness of film layers corresponding to similar values reported in the literature, the minimal amounts of pinholes, and the corresponding XRD graphs showing good

conversion of precursor to perovskite, the only remaining defect the author believes exists is the surface contact to preceding and subsequent ETL and HTL. With poor contact between the semiconductor layers, it is hypothesized that this could be contributing to high series resistance.

Multiple perovskite precursor and deposition methods were tested to alleviate this issue, but in all cases the same poor fill factor and voltage was observed (See Appendix A.2-A.3).

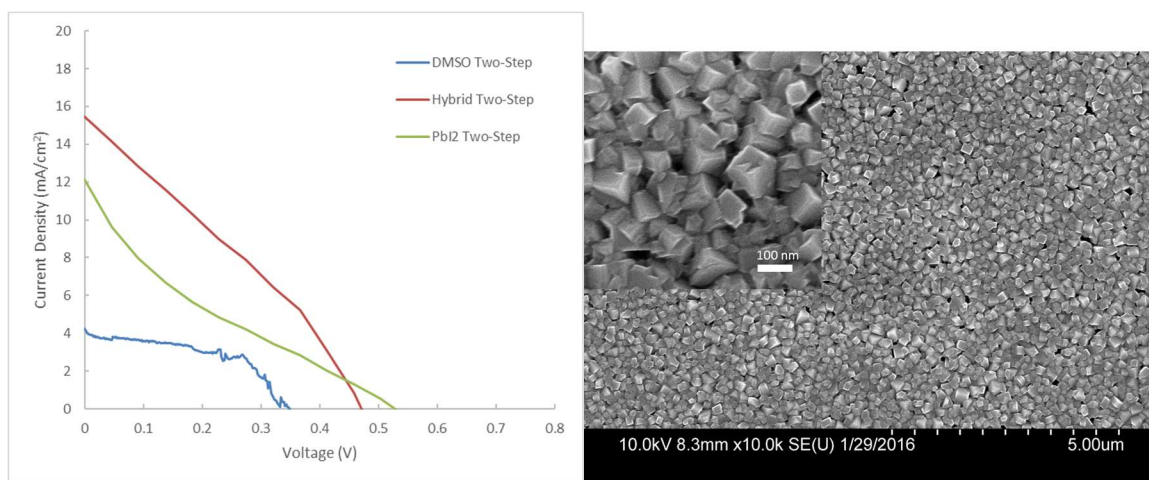


Figure 5.8. (left) I-V curve of illuminated solar cells based on three separate precursor solutions. (right) Scanning electron micrograph with inset of magnified perovskite grains deposited from DMSO based precursor.

In this specific test, the same TiO<sub>2</sub> ETL was used on all substrates, as were the HTL, Spiro-MeOTAD. Poorer than normal open circuit voltage was observed (See Table 5.1), but the hybrid perovskite outperformed the other two consistently in longitudinal testing. The high 1M concentration of PbI<sub>2</sub> in DMF or DMSO struggles to evenly coat an entire substrate via spin-coating, whereas the hybrid precursor deposits easily reproducible films. Improving the film uniformity of the non-hybrid precursors is achieved by heating the solution to 40-70° C prior to deposition.

Front TCE	ETL	Perovskite Process	HTL	Counter Electrode	$V_{oc}$ (V)	$J_{sc}$ (mA/cm <sup>2</sup> )	FF (%)	$\eta$ (%)
ITO	Compact TiO <sub>2</sub>	Hybrid Two-Step	Spiro-MeOTAD	Evaporated Ag	0.458	15.465	30.58	2.16
ITO	Compact TiO <sub>2</sub>	PbI <sub>2</sub> Two-Step	Spiro-MeOTAD	Evaporated Ag	0.504	12.145	18.8	1.15
ITO	Compact TiO <sub>2</sub>	DMSO Two-Step	Spiro-MeOTAD	Evaporated Ag	0.348	4.24	52.13	0.77

Table 5.1. Comparison of different perovskite precursors used with identical deposition steps.



Figure 5.9. Photograph of high-temperature-ETL perovskite cells showing the variance during spin coating based on precursor used, and ETL surface roughness.

### Low Temperature TiO<sub>2</sub> Perovskite Solar Cells

Due to the previously mentioned temperature limitations of CuNWs, several low temperature ETL layers were investigated, the primary being a method by Katoch *et al.*[118], [133], with titanium isopropoxide reacted in water and HCl to create a TiO<sub>2</sub> sol that could be spin coated onto ITO substrates (See Appendix B.2). This method requires an annealing step at 135 °C, which is compatible with CuNW TCEs. The perovskite solar cells are deposited nearly identical to the high temperature analogy, with the only difference being the ETL layer. These cells, while working, were quite low in all metrics and can be seen in Figure 5.11 and Table 5.2.

### Low Temperature PEDOT:PSS Perovskite Solar Cells

The inverted low temperature architecture was implemented to test against the TiO<sub>2</sub> low temperature blocking layer since it poorly performed during testing in fill factor and resulting

efficiency. In addition, our prior work with PEDOT:PSS in CuNW TCEs made this architecture appealing, with the potential for PEDOT:PSS serve as both HTL and improve surface roughness of the underlying CuNW layer.

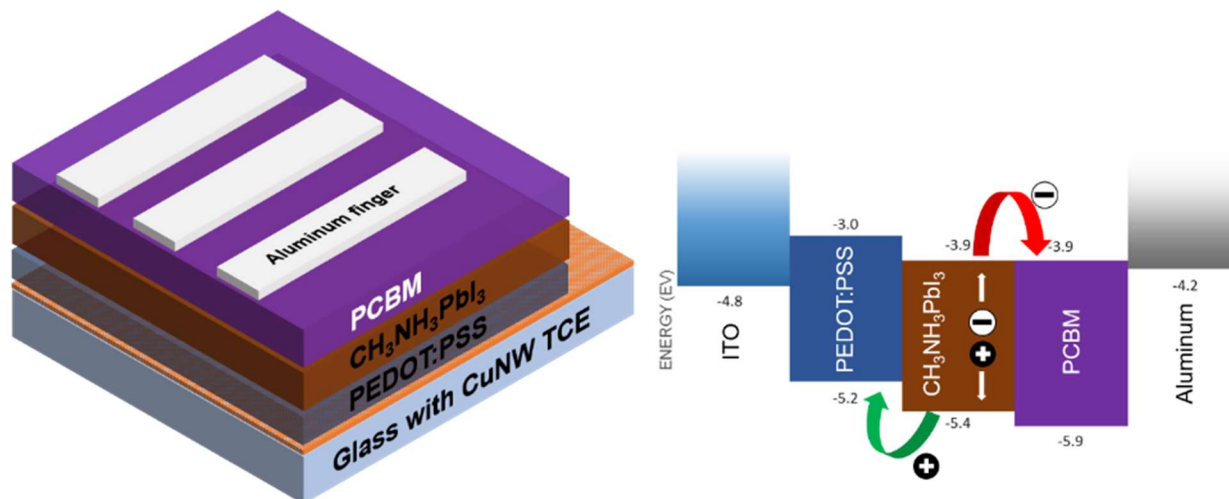


Figure 5.10. (left) Inverted planar heterojunction perovskite solar cell using PEDOT:PSS as the hole transport layer and PCBM as the ETL. (right) Band diagram of completed solar cell showing direction of electron and hole flow.

These cells were investigated using both one-step and two-step deposition methods, but the two-step deposition method resulted in significantly higher (Table 2) short circuit current and consistently outperformed in reproducibility. Because of the aluminum required for the back electrode, full testing of these cells were not done due to budget constraints.

### Electron Transport Layer Free Perovskite Solar Cells

To further troubleshoot the efficacy of the active layer material, perovskite cells were deposited without an electron transport layer between them and the front TCE. This architecture is simpler with one fewer layer to optimize, and is known to perform similarly as those with an ETL.[69], [134] This was also investigated (Table 2) for compatibility with CuNW as the front TCE as it did not require high annealing temperature.

## Low temperature ZnO electron transport layer

Zinc oxide has been used as a TiO<sub>2</sub> alternative, providing lower efficiencies as a tradeoff to not requiring the high temperature annealing. [28], [135], [136] Zinc oxide was synthesized similarly to Liu & Kelly[137] and used as a low temperature planar or pseudo-mesoporous ETL in perovskite cells. Similar to depositing TiO<sub>2</sub>, ZnO nanoparticles in solution are spin coated on the TCE, and repeated multiple cycles to achieve desired thickness. After an annealing step at 100-120 °C to improve necking and remove solvents, a two-step perovskite layer is deposited as described in the experiment section.

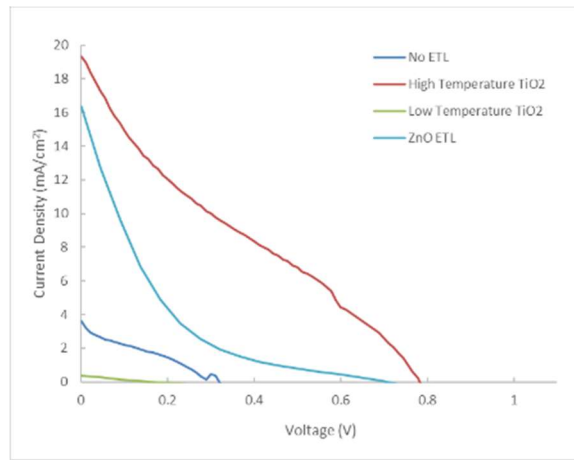


Figure 5.11. I-V curves of the different ETLs used with hybrid perovskite solar cells. In all cases, the extremely high series resistance and low shunt resistance limits the fill factor greatly.

Front TCE	ETL	Perovskite Process	HTL	Counter Electrode	$V_{oc}$ (V)	$J_{sc}$ ( $mA/cm^2$ )	FF (%)	$\eta$ (%)
ITO	None	Hybrid Two-Step	Spiro-MeOTAD	Evaporated Ag	0.311	3.612	26.25	0.3
ITO	High-Temp Compact TiO <sub>2</sub>	Hybrid Two-Step	Spiro-MeOTAD	Evaporated Ag	0.879	19.96	14.19	2.49
ITO	Low-Temp Compact TiO <sub>2</sub>	Hybrid Two-Step	Spiro-MeOTAD	Evaporated Ag	0.138	0.39	26.4	0.01
ITO	Mesoporous TiO <sub>2</sub>	Hybrid Two-Step	Spiro-MeOTAD	Evaporated Ag	0.56	0.1	N/A	N/A
ITO	ZnO nanoparticles	Hybrid Two-Step	Spiro-MeOTAD	Evaporated Ag	0.687	16.34	8.415	0.95

Table 5.2. Summary of performance characteristics of perovskite cells using different ETLs.

Overall, ZnO can be used as an ETL with diminished performance, but all the perovskite cells deposited universally had significant loss in fill factor. The high temperature TiO<sub>2</sub> competes

with the literature in terms of current density and voltage, but efficiency is still limited by the very poor fill factor. Further investigation into improving the series resistance throughout the cells, and increasing the shunt resistance is necessary to achieve full functioning perovskite solar cells.

## CHAPTER 6

### INTEGRATING COPPER NANOWIRES INTO DEVICES

#### 6.1 INTRODUCTION

Copper nanowire TCEs show a lot of promise, having similar conductivity as silver nanowires. However they exhibit lower stability over time in air, unless passivated with graphene, graphene oxide[13] or similar coating. Within this thesis, certain differences were observed between the use of silver nanowires (AgNWs) and copper nanowires (CuNWs). While silver nanowires can be stored and then deposited without treatment, copper nanowires required plasma, forming gas annealing, or acid treatment to remove the polyvinylpyrrolidone (PVP) coating that prevents oxidation and allows the nanowires to be suspended in isopropyl alcohol. Isopropyl alcohol as solvent for CuNW was used for several reasons[13]: the first being the ability to spray coat the nanowires for large scale TCE deposition, at low temperature and without expensive equipment. CuNWs suspended in IPA can be rapidly deposited onto substrates maintained at a temperature of 40-70 °C via artist airbrush (Paasche Model H with Argon) at a distance of 20 cm. Few works [138] have presented nanowires as an electrode replacing ITO or FTO in solar cells, and the research conducted in this thesis reveals why. Implementing the copper nanowire hybrid electrodes as both front and back electrode in a perovskite cell was investigated.

#### 6.2 METHODOLOGY

##### Copper Nanowires as the front electrode

##### Temperature Requirements

Copper nanowires were first investigated as the front electrode for dye-sensitized solar cells and immediately had foreseen issues with the titanium dioxide mesoporous layer requiring a 450-500 °C annealing step. Due to the liquid electrolyte functioning as the HTL in non-solid-state-

DSSCs, it was also impossible to invert the architecture and have the copper nanowires added last after all processing steps. Blade coating, screen printing, and even spin coating were realized as incompatible with as-deposited CuNW TCEs due to the mechanical instability.[13] More detail into integrating CuNWs into DSSCs is covered in the dissertation titled “*Emerging Materials for Transparent Conductive Electrodes and Their Applications in Photovoltaics.*” Some of the findings from DSSC integration were carried over to perovskite solar cells, and low temperature perovskite processing steps were investigated. In addition to requiring lower temperature deposition and annealing steps for compatibility with CuNWs, there also emerged the issues of mechanical stability, surface roughness and corrosion.

### **Mechanical Stability**

The limitations of the mechanical stability of CuNWs are previously reported in Chapters 2 and 4, and these issues continue to be hurdles when combining the TCE with perovskite solar cells. The failure of CuNW TCEs to pass the scotch tape test pose issues with deposition steps such as blade coating and spin coating with high viscosity solvents. In extreme cases, high viscosity solvents spin coated on top of CuNWs can remove or degrade the TCE, making them non-conductive. To improve the mechanical stability of the CuNW TCE, a titanium tetraispropoxide (TTIP) solution in IPA (see Appendix A.5) that was initially developed as an electron transport layer was also tested as an “anchoring solution.” Several other materials, such as ZnO nanoparticles (5-20 nm) were both synthesized and purchased from Sigma Aldrich for testing as both anchoring solution and electron transport layer.

### **Chemical Stability**

From our previous work with DSSCs, the limited corrosion resistance of CuNW TCEs was discovered when exposed to iodine elements. Perovskite solar cells contain considerable amounts

of iodine not only in the active layer, but also in the hole transport layer and can affect CuNWs through incomplete barrier layers between them. This corrosion can destroy the conductivity of a CuNW TCE in minutes so efforts were made to protect the underlying TCE. Several materials were investigated as a barrier between the iodine active layer and CuNW TCE. Testing was done by masking ITO substrates with Kapton tape and etching with HCl to leave two ITO contacts on either side of the substrate. CuNWs were spray coated and plasma cleaned to remove organics and the resistance was measured across the ITO contacts. Each material candidate was spin, spray or blade coated onto the CuNW TCE and the resistance was again measured across the ITO contacts. In the cases that the resistance degradation wasn't immediate, subsequent measurements were done 24 and 48 hours later.

As PEDOT:PSS is used as a hole transport layer in inverted perovskite solar cells, it was a prime candidate as the barrier layer between the CuNW TCE and perovskite active layer. In ITO-based solar cells, the PEDOT:PSS layer is spin-coated at high speed to achieve a 40-60 nm thick layer on the cleaned ITO surface. [53][59] Zinc oxide nanoparticles in solution were also investigated as a barrier layer because of their use as a low temperature ETL in planar perovskite solar cells.[137] Titanium tetraisopropoxide (TTIP) anchoring solution was tested as a barrier layer as well, due to the high mechanical stability it introduced to the CuNW TCEs, and its use in literature as precursor for ETLs in both DSSCs and perovskite cells. [28], [139]–[141] TiO<sub>2</sub> nanoparticles (P25, purchased from Sigma Aldrich) are used in DSSCs and perovskites as a mesoporous electron transport layer several microns thick. Pre-annealing these nanoparticles at 500 °C and using binder-free solvents for spin coating were tested as a barrier layer as titanium oxide is not easily corroded by iodine[138]. Reduced graphene oxide platelets showed capability as a humidity and oxidation barrier for copper nanowires[13], and similar techniques were used to

test if platelets of GO spin coated on CuNW and reduced in a forming gas environment would provide protection for the CuNW film against the iodine electrolyte.

### **Surface Roughness**

The high surface roughness of nanowire TCEs are well known to short thin film PV cells[1][70], [78], [142], so creating a planar TCE from CuNW hybrid films is desirable. In addition, spin coating on rough surfaces such as a nanowire grid does not produce a planar subsequent layer.[143] Spray coating and blade coating were investigated as deposition alternatives to planarize the TCE surface and are discussed later. Several alternative electron transport layers with varying viscosities were tried out to planarize the surfaces on which the perovskite precursor was deposited (See Appendix C).

### **Copper Nanowires as the Back Electrode**

Due to the transmittance of CuNW TCEs, using the film as a back electrode in transparent thin film solar cells was investigated. No current literature has examined this, but silver nanowires and conductive polymers have been used similarly as the back electrode for integration into tandem solar cells and aesthetic applications.[24], [52] Such aesthetic semi-transparent perovskite solar cells are being investigated for use in windows, roofs, greenhouses and other fashion elements. [144]–[147]

For use in tandem solar modules, the perovskite cell with transparent back electrode is mounted in front of a silicon cell, absorbing the higher energy photons and allowing the lower bandgap silicon cell to absorb the remainder.[70] Modeling done by Coutts *et al.*[148] provided the optimum band gap energies of the top cell ( $1.72\pm 0.02$  eV) and bottom cell ( $1.14\pm 0.02$  eV).

Hybrid perovskite solar cells are good candidates for the upper absorber as it is a strongly absorbing direct bandgap semiconductor with a bandgap around 1.6 eV.[70]

Depositing CuNW via spray coating on the back of a perovskite solar cell would be most ideal for controlling transmittance similar to reported work with silver nanowire back electrodes[70], but the organic PVP coating on the nanowires prevents this from being realized. Removing the PVP coating requires plasma cleaning[13], a process that is destructive to all organic chemicals in the film, including PEDOT:PSS and methylammonium iodide. Removing the PVP coating through nitric or acetic acid post deposition damages the perovskite solar cell rapidly. Similarly, the nickel electro-less plating process that protects the CuNWs from corrosion and improves conductivity, is not compatible with already assembled perovskite solar cells.

Copper nanowires were filtered onto a PTFE membrane through vacuum suction from solution in the presence of equal-volume nitric acid (10 wt%) before being washed with IPA. They were then transferred to complete perovskite cells (See Appendix B) with pressure. The transfer is complete with no visible copper remaining on the filter membrane. Completed solar cells are then characterized by direct surface contact of the probe to the CuNW, and the other clipped to the ITO contact.

## **6.3 RESULTS AND DISCUSSION**

### **Chemical stability**

Chemical stability of copper in nanowire form is an issue, as integration with DSSCs showed the quick degradation of copper from iodine contained in the electrolyte. Perovskite solar cells composed of lead iodide can diffuse down to the TCE, and erode the nanowire grid if not

properly protected from the iodine component. Nickel and platinum are both metals that are highly resistant to iodine corrosion[149], and nickel was investigated as a protective layer.

To test the effects of each deposition and processing step on the mechanical or chemical stability of the CuNW TCE, ITO substrates were masked and etched in concentrated HCl to leave two electrical contacts on the substrate. CuNWs were then spray coated and treated as detailed in previous work[13], overlapping the contacts for conductivity measuring across the substrate (See Figure 6.1). This allows the contacts to be masked off with scotch tape for spin coating processes to prevent coverage of contacts. Table 6.1 shows the layers tested in this fashion for protection against corrosion.

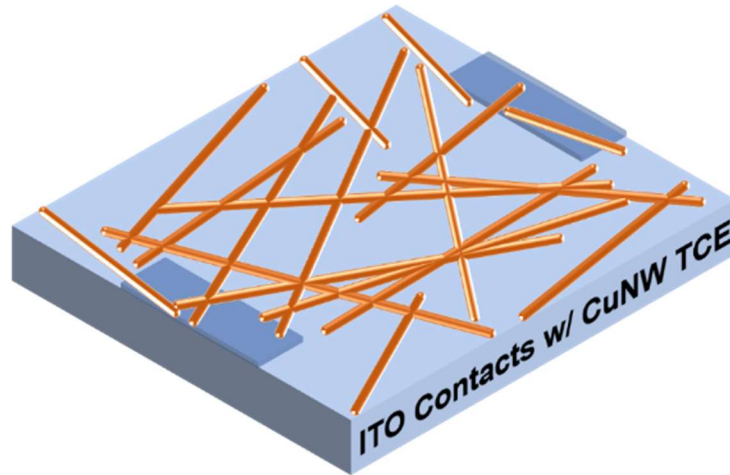


Figure 6.1 . Rough schematic of etched ITO contacts with CuNWs sprayed on top for testing mechanical and chemical stability. Substrates are 1”x 1” in size.

Barrier Layer	PEDOT:PSS	ZnO (5-20 nm)	TTIP	TiO <sub>2</sub> (P25)	rGO	Nickel Coating
Protects Against Iodine Corrosion	✗	✗	✗	✗	✗	✓

Table 6.1. Summar of barrier layers tested on CuNWs to prevent corrosion from iodine elements in the perovskite layer. Some of these failures may not be a component of chemistry, but rather surface roughness and the film coverage, which is discussed later.

The electro-less nickel plating developed by Rathmell *et al.*[150] was modified to nickel-plate the wires not in solution, but as-deposited on glass immediately after spray coating. This process is detailed in Appendix A.1 and provides excellent protection when directly exposed to iodine-containing perovskite. A benefit to this process is that the nickel coating attaches primarily to the CuNWs rather than the entire substrate, limiting the transmittance loss. All other layers tested did not provide adequate protection once the perovskite layer was deposited, and M $\Omega$  resistance was observed.

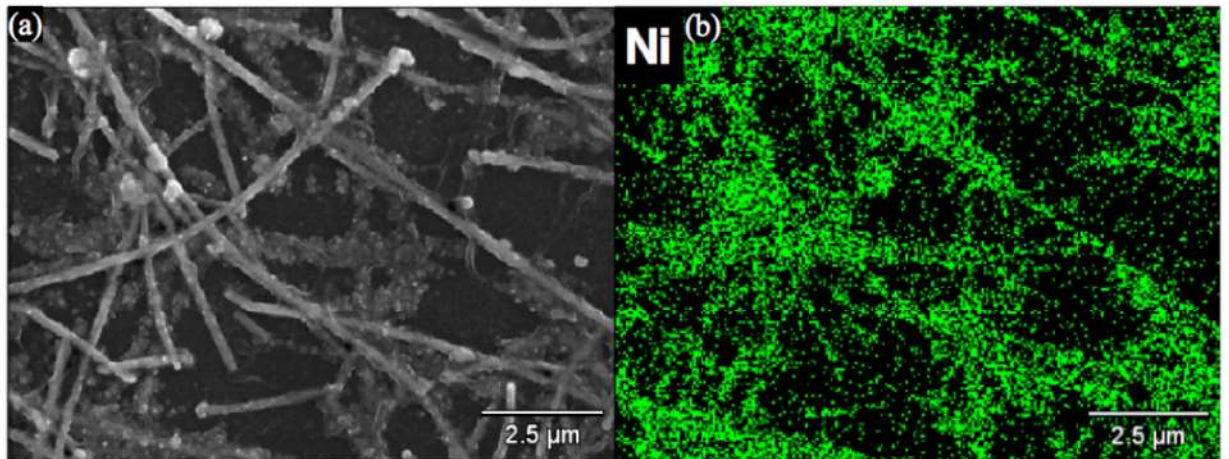


Figure 6.2. (a) Scanning electron micrograph of CuNWs that have been coated with nickel. (b) EDX of same area showing the nickel primarily on the wires instead of the substrate.

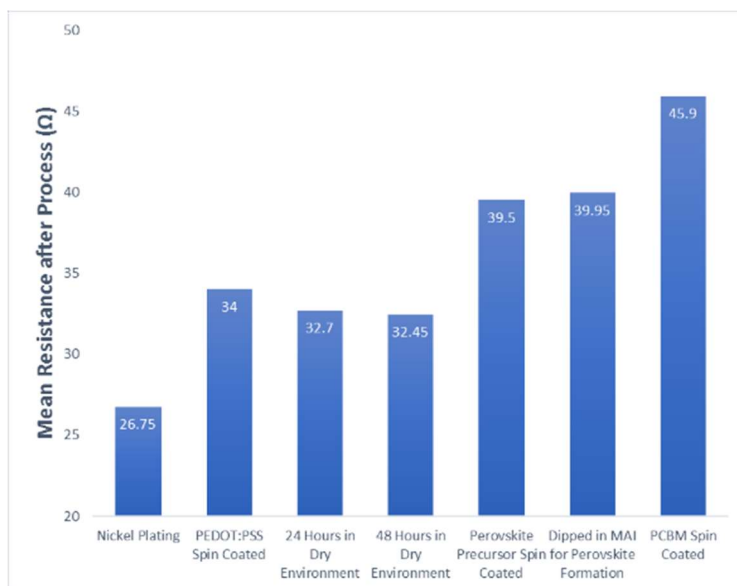


Figure 6.3. Chart showing the progression in resistance across nickel coated CuNW TCE with each deposition step and process and over 48 hours in low humidity, room temperature environment.

### Mechanical stability

Certain viscous solvents can damage or move the CuNW during the spin coating. PEDOT:PSS that has been preheated or has concentrated is one example of this, and not only can it displace the CuNWs during spin coating, but also degrades the wires over time. Figure (6.3) illustrates the immediate degradation of an unprotected CuNW film when exposed to PEDOT:PSS spin coated on when heated to 70 °C. Not only does the film approach MΩ resistance, but the CuNWs have disappeared completely in the PEDOT:PSS-coated region.

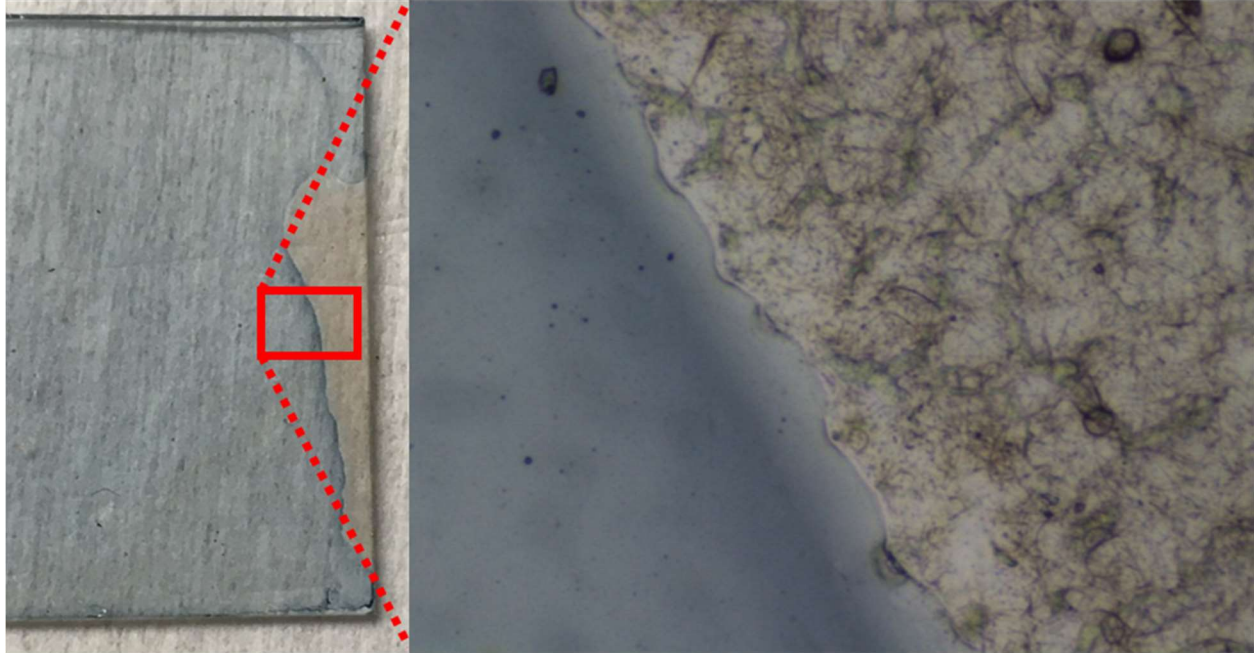


Figure 6.4. (left) Photograph of CuNW film that heated PEDOT:PSS has been spin coated on in an incomplete film. (right) Optical micrograph of same CuNW film that has been eroded or displaced where PEDOT:PSS solution has contacted.

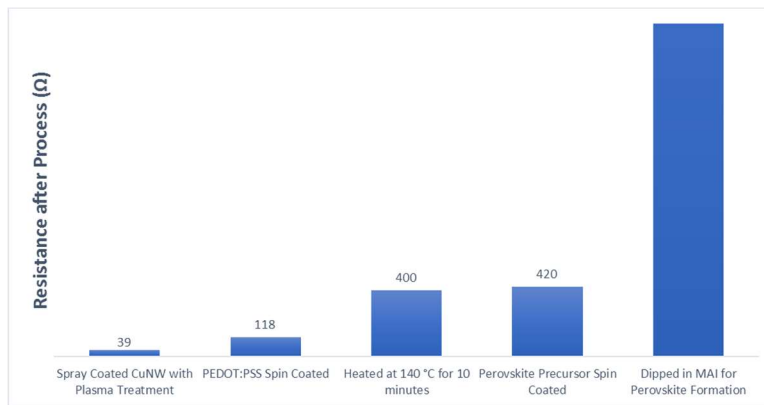


Figure 6.5. Progression of CuNW TCE (no nickel coating) resistance after process (final resistance measured is  $\sim 5000 \Omega$ )

In figure 6.4, exposed CuNW TCEs coated with PEDOT:PSS increase dramatically in resistance, and quickly degraded with subsequent layer depositions, also showing the iodine corrosion.

One solution to this is the TTIP anchoring solution that was developed which reproducibly protects the CuNW from even the scotch tape test (see figure 6.5). Future work should include

SEM, AFM and EDX analysis of the TTIP solution on CuNWs to further understand the mechanics of this anchoring.

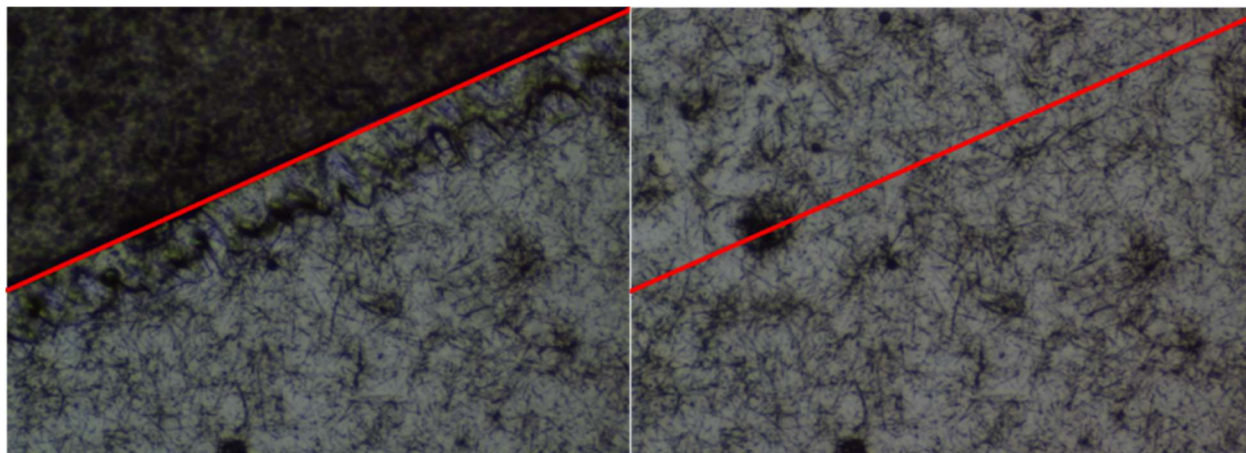


Figure 6.6. (left) Microscope image of tape affixed to CuNW/TTIP TCE. (right) Same substrate with tape removed, showing robustness of conducting film.

### **Surface roughness**

With issues of corrosion addressed via nickel plating, mechanical stability addressed with the TTIP anchoring solution, low temperature processes developed limited the processing temperature to under 120 °C, the last remaining issue to overcome is the surface roughness of CuNW TCEs. All the precursors used for both chemical stability and mechanical stability were tested via spin and spray coating to build up a planar layer on top of the CuNW. Unfortunately, due to the high peak-valley distance in CuNW TCEs (between 50 and 500 nm, depending on the number of nanowires overlapping), spin coating and even spray coating does not “fill in” the valleys and lead to a planar surface. It is speculated that surface tension of the solvent molecules, whether deionized water or IPA, do not allow for “filling” in the substrate, but rather preserve the underpinning structure at this scale. Following procedures in the literature for spin coating on

rough surfaces[143], little to no reduction in peak-valley distance was achieved with all ETL or buffer layers through spin coating. In addition, spray coating also yielded no reduction in peak-valley distances but in some areas amplified the peak-valley distance.

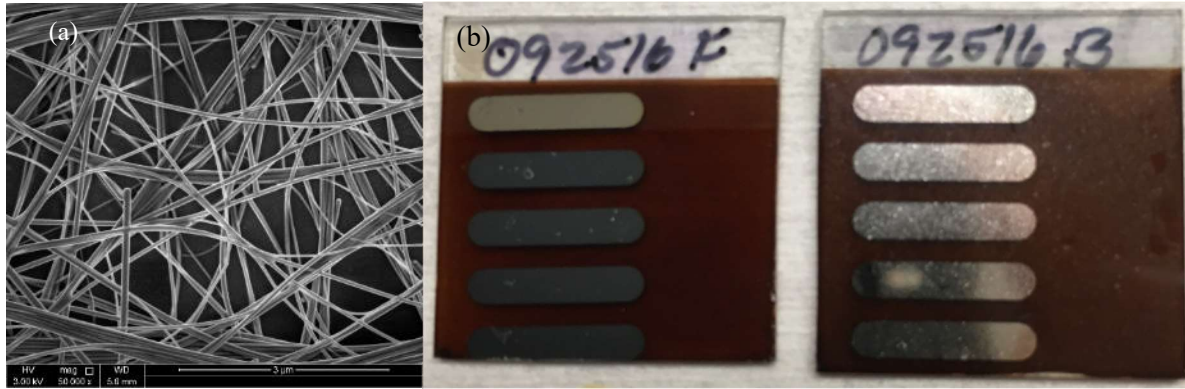


Figure 6.7. (a) Scanning electron micrograph showing a more realistic pattern of a full CuNW TCE, with bundles and multiple nanowires stacked on one another at intersections. (b) Photograph showing comparison to ITO TCE (left) perovskite cell and CuNW TCE perovskite cell showing the surface roughness that penetrates through all layers to the Ag fingers.

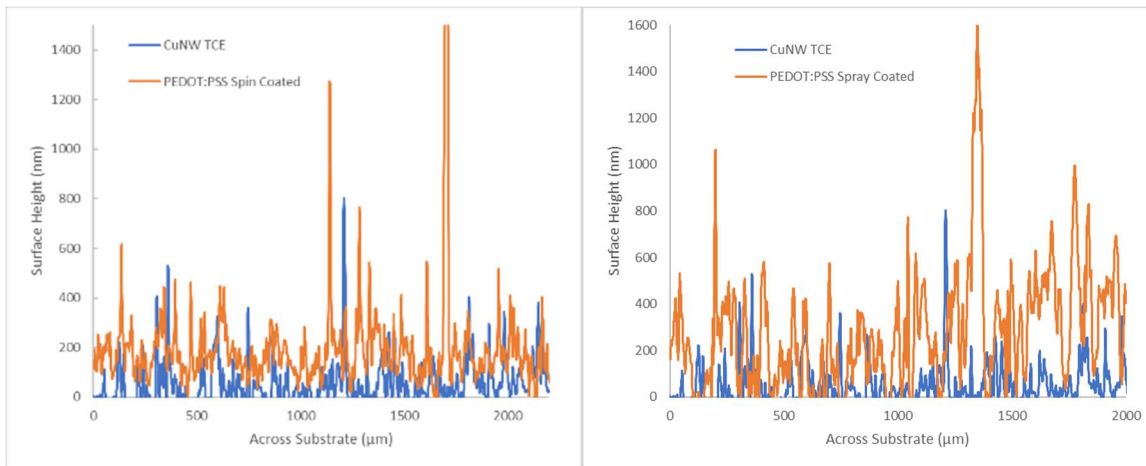


Figure 6.8 . Difference in surface profile height when spin or spray coating PEDOT:PSS on CuNW TCEs to form a planar HTL.

The only method that yielded a quantifiable change in peak-valley distance was rolling a glass vial of diameter 0.8” across the CuNW TCE using hand pressure. While removing some of the CuNWs,

the conductivity of the TCE improves with the pressure, and the surface roughness nearly halves with no change in film transmittance (see Figure 6.8).

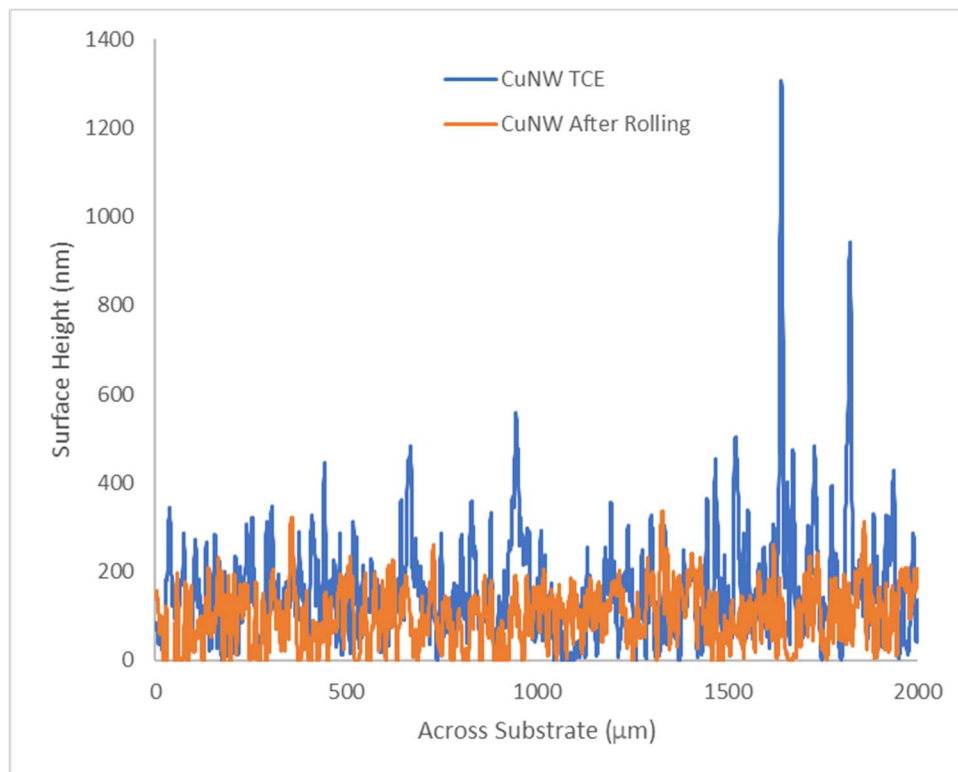


Figure 6.9. Profilometry data showing the one method of surface planarization that worked to a quantifiable degree, rolling pressure on the CuNW TCE.

Unfortunately, this reduced peak-valley distance is still not close to a planar surface upon which smooth films can be made via spin-coating or spray-coating. Experiments were done to spin or spray coat ETL and buffer layers post-rolling to create a planar surface for the perovskite to be deposited but completed cells yielded significant short-circuits. This can be assumed to be the result of the CuNWs penetrating all layers, thereby dissipating any generated electrons through recombination immediately.

### **Copper Nanowires as the Back Electrode**

Several methods were employed to either replicate the literature, or use previous processes explored to restore conductivity to deposited CuNWs. In every case, spray coating CuNWs onto completed perovskite solar cells and restoring conductivity resulted in a non-functioning solar cell (Table 6.2).

PVP Removal Process	Plasma Cleaning	Nitric Acid Wash	Acetic Acid Wash	Nickel Coating
Perovskite Solar Cell Remains Intact:	x	x	x	x

Table 6.2. Summary of conductivity restoring methods previously used on CuNW TCEs and attempted on a completed perovskite cell with CuNW back electrode.

To preserve the cell integrity, cells were stamped with the vacuum-filtered CuNWs with pressure and characterized immediately. Shorts are rampant through the system, exhibited by the very low resistance and voltage measured from front electrode to back electrode. Due to the poor voltage measured, full solar simulator measurements were not conducted.

Front TCE	ETL	Perovskite Process	HTL	Counter Electrode	$V_{oc}$ (V)	$J_{sc}$ ( $mA/cm^2$ )
ITO	PCBM	Hybrid Two-Step	PEDOT:PSS	CuNW	0.16	1.5
ITO	None	PbCl <sub>2</sub> :MAI	Spiro-MeoTAD	CuNW	0.04	1.1
ITO	ZnO	PbCl <sub>2</sub> :MAI	PEDOT:PSS	CuNW	0.04	1.3
FTO	High-Temp Compact TiO <sub>2</sub>	Hybrid Two-Step	Spiro-MeoTAD	CuNW	0.3	1.1

Table 6.3. List of cell architectures attempted with CuNW back electrode stamped after vacuum filtration.



Figure 6.10. (left) Completed perovskite solar cell with evaporated back electrode. (left) Completed perovskite solar cell with CuNW back electrode.

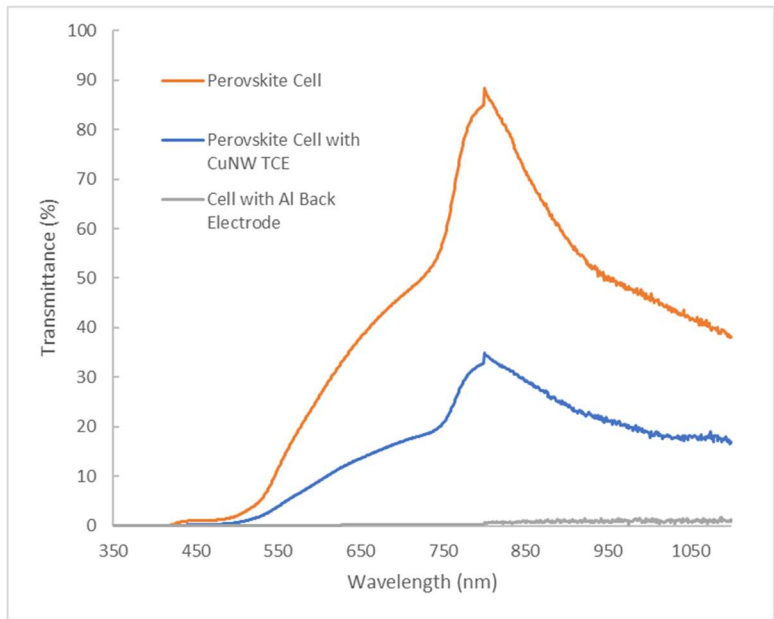


Figure 6.11. Comparison of transmission through a perovskite cell with and without CuNW back electrode, and a nearly opaque aluminum electrode.

In conclusion, multiple methods of perovskite synthesis and deposition were explored to first achieve comparable results to literature perovskite photovoltaics. While lacking in fill factor

significantly in all developed types of cells, work was conducted to integrate CuNW TCEs into these cells as both the front and back electrode. Three of the four difficult engineering problems were addressed to use a CuNW TCE as the front electrode, but much work much still be done to planarize the TCE for deposition of subsequent layers. Applying rolling pressure to an as-deposited CuNW TCE shows promise, and a heated press may be the next step moving forward. Using CuNW as the back electrode could also be further investigated using a precision press to prevent the CuNW TCE from penetrating the entire solar cell while still making ohmic contact with the top ETL or HTL.

## APPENDIX A: MATERIAL SYNTHESIS

### A.1 Ni-coated CuNW thin Films

The Ni-coating process is adopted from Rathmell *et al*[150] with slight modifications. Spray deposited CuNW samples were placed in a beaker with 3 mL ethylene glycol to submerge it entirely. Nickel acetylacetonate (0.1 M, 0.1 mL) and NaOH (0.03 M, 0.1 mL) were added while keeping the temperature at 114 °C. Finally, hydrazine solution (35 wt%, 0.157mL) was added to the mixture. The Ni-coated CuNWs were taken out of the solution after 5 minutes and rinsed with IPA and dried with compressed air.

### A.2 Two-Step PbI<sub>2</sub> Perovskite Precursor in DMF

Perovskite precursor solution was prepared by stirring lead (II) iodide (purchased from Sigma Aldrich, 99.999% purity) into dehydrated DMF at 1M concentration. This suspension is stirred vigorously for 12 hours at 40 °C. After cooling to room temperature, the yellow suspension is filtered via syringe filter (0.45 μm) leaving a yellow solution. This solution is stored in a dry box and wrapped with parafilm until use.

### A.3 PbI<sub>2</sub>:MAI Hybrid Perovskite Precursor in DMF

Perovskite precursor solution was synthesized by stirring Lead (II) Iodide (purchased from Sigma Aldrich, 99.999% purity) and Methylammonium Iodide (purchased from DyeSol) into dehydrated DMF at molar ratio 1:0.15, respectively. This suspension is stirred vigorously for 12 hours at room temperature. The yellow suspension is filtered via syringe filter (0.45 μm) leaving a yellow solution which is wrapped with parafilm and stored in a dry box until use.

#### **A.4 PbCl<sub>2</sub>:MAI One-Step Perovskite Precursor in DMF**

Lead Chloride based perovskite precursor was synthesized similar to Zhang *et al.*[151] by stirring Methylammonium Iodide and Lead (II) Chloride (Sigma Aldrich, 98% purity) at a 3:1 molar ratio, respectively, in dehydrated DMF at 40 wt%. This is stirred vigorously for 12 hours before filtration through a 0.45  $\mu\text{m}$  PTFE syringe filter and heated to 70  $^{\circ}\text{C}$  prior to use.

#### **A.5 TiO<sub>2</sub> electron transport layer synthesis**

High temperature annealed TiO<sub>2</sub> layers are synthesized similarly to Park *et al.* [152] by adding 200  $\mu\text{l}$  of titanium tetra-isopropoxide to 10 ml of IPA and shaking vigorously before use as ETL.

Low temperature nanoparticle dispersions of TiO<sub>2</sub> were synthesized following the method reported by Katoch *et al.*[118], [133], in which 365  $\mu\text{l}$  of titanium tetra-isopropoxide is added dropwise to 5 mL of anhydrous isopropyl alcohol in the presence of 70  $\mu\text{l}$  1M hydrochloric acid while stirring vigorously. After 2 hours of stirring at room temperature, the solution is filtered through a PTFE filter and spin coated as is.

## APPENDIX B: SOLAR CELL FABRICATION

### **B.1 High and Low Temperature Two-Step Planar Heterojunction Perovskite Solar Cell Deposition**

ITO or FTO substrates are boiled in IPA and then sonicated, then boiled again in deionized water. After cooling to room temperature, the substrates are blown dry with compressed air and then plasma cleaned in low pressure air for 5 minutes. The front contact is masked with scotch tape and 100  $\mu\text{l}$  of the above ETL precursor is deposited dynamically at 4000 rpm, then annealed (450  $^{\circ}\text{C}$  for a half hour for high temperature ETL  $\text{TiO}_2$ , 135  $^{\circ}\text{C}$  for a half hour for low temperature ETL  $\text{TiO}_2$ ). Once cooled, the substrates are then re-masked and the perovskite precursor layer (1M  $\text{PbI}_2$  in DMF) is deposited via spin coating at 4000 rpm dynamically. This layer is left to dry in air at room temperature and becomes shiny yellow within a minute. The substrate is then dipped into an MAI solution (10 mg/ml in IPA) for 5 minutes, at which point the film should turn to a shiny reddish-brown film. The substrate is washed with anhydrous IPA and dried at 4000 rpm in the spin coater. Spiro-MeOTAD solution was prepared by dissolving 72.3 mg of spiro-MeOTAD in 1 ml chlorobenzene, to which 28.8  $\mu\text{l}$  of 4-tert-butyl pyridine and 17.5 ml of lithium bis(trifluoromethanesulfonyl)imide (LiTFSI) solution (520 mg/ml acetonitrile) were added. The spiro-MeOTAD layer is deposited dynamically at 1000 rpm in a glove bag on the perovskite and then left in the glove bag over night to oxidize. The cells are finished with 100 nm ebeam evaporated silver electrode with shadow mask.

## **B.2 Low temperature Inverted Planar Heterojunction Perovskite Solar Cell Deposition**

ITO substrates are boiled in IPA and then sonicated, then boiled again in deionized water. After cooling to room temperature, the substrates are blown dry with compressed air and then plasma cleaned in low pressure air for 5 minutes. The front contact is masked with scotch tape and 100  $\mu$ l of PEDOT:PSS is deposited dynamically at 6000 rpm, then heated at 140 °C for 30 minutes to remove any moisture. Once cooled, the substrates are then re-masked and the perovskite precursor layer is deposited via spin coating at 4000 rpm dynamically. This layer is left to dry in air at room temperature before being dipped into an MAI solution (10 mg/ml in IPA) for 5 minutes, at which point the film should turn to a shiny reddish-brown film. The substrate is washed with anhydrous IPA and dried at 4000 rpm in the spin coater. [6,6]-phenyl-C<sub>61</sub>-butyric acid methyl ester (PCBM) in chlorobenzene (10wt%) is spin coated on the cell at 4000 rpm. The cells are finished with a 100 nm thermally evaporated aluminum electrode with shadow mask.

## **B.3 Mesoporous Perovskite Solar Cell Deposition**

FTO substrates are boiled in IPA and then sonicated before boiling again in deionized water. Once cooled to room temperature, they are blown dry with compressed air and then plasma cleaned in low pressure air for 5 minutes. P25 TiO<sub>2</sub> nanoparticle powder was mixed in ethanol at a 1:25 weight ratio and stirred vigorously for 48 hours to make the mesoporous TiO<sub>2</sub> suspension. The TiO<sub>2</sub>-mp was then spin coated on the FTO substrates at 3000 rpm before being heated to 450 °C for 30 minutes. Perovskite precursors (both one and two-step) were deposited via spin coating at 4000 rpm and the perovskite was formed via heating or dipping in MAI, respectively. Spiro-MeOTAD was spin coated at 1000 rpm before evaporation of a Ag electrode.

#### **B.4 Sandwiching back electrode configuration and why it doesn't work**

To expedite solar cell testing, several back electrodes were tested in similar fashion to a DSSC back electrode in which the back electrode material is deposited on a glass substrate and then applied to the rest of the cell to complete it. In a DSSC, this is commonly done with carbon or platinum coated ITO and provides the barrier to contain the liquid electrolyte.[153] Due to the liquid electrolyte surface tension, the cell can be assembled with or without spacers, and will still hold enough electrolyte for a testing session. The primary difference between this configuration and a perovskite solar cell is the use of liquid electrolyte rather than a solid-state hole transport layer. This solid-state hole transport layer is spin coated on top of the perovskite, creating a junction to the material and metal is evaporated as the back electrode to form an ohmic contact with the material. Replacing the evaporated metal with a planar electrode results in contact discontinuities due to surface roughness. Materials tested were: silver on glass substrates, CuNW on glass substrates, and PEDOT:PSS on glass substrates. In every case, no current was detected compared to control cells that had evaporated metal contacts.

## APPENDIX C: CHARACTERIZATION TOOLS AND METHODS

### C.1 Sheet Resistance Measurements

For localized measurements, we used a commercial SRM-232 surface resistivity meter. The SRM-232 has measuring range of 0 – 2000  $\Omega/\text{sq}$ , and accuracy of 0.1  $\Omega/\text{sq}$ . The four round probes are closely separated and therefore can only measure localized sheet resistance. Figure C.1 (a) is a photograph of SRM-232 surface resistivity meter in measurement.

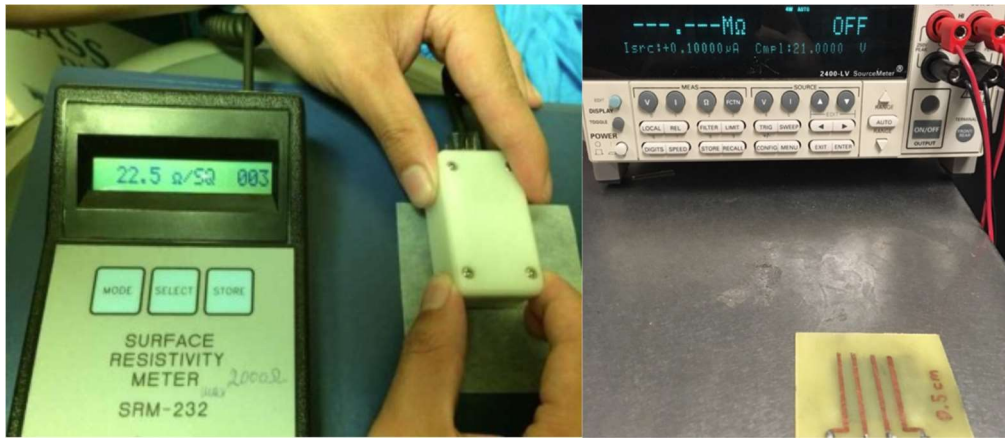


**Figure C.1** (left) SRM-232 surface resistivity meter. (right) Photograph of customized 4-probe electrode and Keithley source-meter setup.

However, in many other cases, the sheet resistance is higher than 2000  $\Omega/\text{sq}$ , especially in the cases of thermally annealed ZnO and doped ZnO thin films; in addition, measurements across the sample area rather than within localized region are usually more desirable. Hence we developed a customized 4-probe system for larger range and size of measurements. Figure B.1 (b) is a photograph of the customized 4-probe electrode connected to a Keithley 2400 source-meter unit.

### C.2 Absorption and optical transmittance measurements

The absorption and optical transmittance spectra were measured using Cary-3000 UV-Vis-NIR spectrophotometer. Specifically, the absorption of CuNW was measured by using a cube glass vial with CuNW solution in IPA, with pure IPA as baseline, using a one-beam configuration. Optical

transmittance spectra were measured using two-beam configuration, with a blank substrate mounted in the reference beam. Another blank substrate was placed in the measurement beam to set the baseline.

### **C.3 X-Ray Diffraction**

X-ray diffraction (XRD) data measurements were made using a PANalytical X'pert Plus Instrument equipped with a programmable incident beam slit with the slit fixed at  $0.5^\circ$ , and an X'Celerator Detector. A 5 mm mask was used to ensure that only the desired part of the slide was illuminated by the x-ray beam. The x-ray radiation used was Ni-filtered Cu  $K\alpha$ ,  $\lambda = 1.5418 \text{ \AA}$ . Measurements were made in the bisecting geometry. Diffraction patterns were analyzed using the Panalytical High Score software and compared with patterns deposited in the ICDD database (Faber J, Fawcett T, *Acta Cryst. (2002)*, **B58**, 325-332).

### **C.4 Scanning Electron Microscopy and Atomic Force Microscopy**

Scanning electron microscope (SEM, Hitachi S-4800 Type II) was used to examine the samples. Cross-sectional SEM images were captured by mounting the substrate vertically, while grazing-angle SEM images were captured by mounting the samples vertically and tilting the stage by  $5^\circ$ . To examine layers within a solar cell, a cell was cleaved after fabrication, and platinum deposited on the edge before imaging. Atomic force microscopy (AFM) was used to study the surface morphology of synthesized materials and fabricated thin films.

### **C.5 Surface Roughness Measurements**

A Veeco DEKTAK 150 profilometer was used to measure the surface profiles of the CuNW and hybrid transparent conducting electrodes. This surface profiler was also used to measure individual film thickness of perovskite solar cells by depositing layers on top of one another and making razor blade incisions in the films.

## REFERENCES

- [1] D. S. Hecht, L. Hu, and G. Irvin, “Emerging transparent electrodes based on thin films of carbon nanotubes, graphene, and metallic nanostructures,” *Adv. Mater.*, vol. 23, no. 13, pp. 1482–513, Apr. 2011.
- [2] S. Bae *et al.*, “Roll-to-roll production of 30-inch graphene films for transparent electrodes,” *Nat. Nanotechnol.*, vol. 5, no. 8, pp. 574–578, Aug. 2010.
- [3] Xuan Wang, \* and Linjie Zhi, and K. Müllen\*, “Transparent, Conductive Graphene Electrodes for Dye-Sensitized Solar Cells,” 2007.
- [4] S. Pang, Y. Hernandez, X. Feng, and K. Müllen, “Graphene as Transparent Electrode Material for Organic Electronics,” *Adv. Mater.*, vol. 23, no. 25, pp. 2779–2795, Jul. 2011.
- [5] J. Wu, H. A. Becerril, Z. Bao, Z. Liu, Y. Chen, and P. Peumans, “Organic solar cells with solution-processed graphene transparent electrodes,” *Appl. Phys. Lett.*, vol. 92, no. 26, p. 263302, Jun. 2008.
- [6] D. S. Hecht *et al.*, “Carbon-nanotube film on plastic as transparent electrode for resistive touch screens,” *J. Soc. Inf. Disp.*, vol. 17, no. 11, p. 941, 2009.
- [7] D. S. Ginley and C. Bright, “Transparent Conducting Oxides,” *MRS Bull.*, vol. 25, no. 8, pp. 15–18, 2000.
- [8] H. Kim, J. S. Horwitz, G. P. Kushto, Z. H. Kafafi, and D. B. Chrisey, “Indium tin oxide thin films grown on flexible plastic substrates by pulsed-laser deposition for organic light-emitting diodes,” *Appl. Phys. Lett.*, vol. 79, no. 3, pp. 284–286, Jul. 2001.
- [9] H. Kim *et al.*, “Effect of film thickness on the properties of indium tin oxide thin films,” [http://oasc12039.247realmedia.com/RealMedia/ads/click\\_lx.ads/www.aip.org/pt/adcenter/pdfcover\\_test/L-37/776270803/x01/AIP-PT/JAP\\_ArticleDL\\_0117/APRconf\\_1640x440Banner\\_12-16B.jpg/434f71374e315a556e61414141774c75?x](http://oasc12039.247realmedia.com/RealMedia/ads/click_lx.ads/www.aip.org/pt/adcenter/pdfcover_test/L-37/776270803/x01/AIP-PT/JAP_ArticleDL_0117/APRconf_1640x440Banner_12-16B.jpg/434f71374e315a556e61414141774c75?x), 2000.
- [10] W. Ke *et al.*, “Efficient hole-blocking layer-free planar halide perovskite thin-film solar cells,” *Nat. Commun.*, vol. 6, p. 6700, Mar. 2015.
- [11] D. S. Ginley and C. Bright, “Transparent Conducting Oxides,” *MRS Bull.*, vol. 25, no. 8, pp. 15–18, Aug. 2000.
- [12] H. Kim *et al.*, “Indium tin oxide thin films for organic light-emitting devices,” *Appl. Phys. Lett.*, vol. 74, no. 23, pp. 3444–3446, 1999.
- [13] Z. Zhu *et al.*, “Ultrahigh Aspect Ratio Copper-Nanowire-Based Hybrid Transparent Conductive Electrodes with PEDOT:PSS and Reduced Graphene Oxide Exhibiting Reduced Surface Roughness and Improved Stability.,” *ACS Appl. Mater. Interfaces*, vol. 7, no. 30, pp. 16223–30, 2015.
- [14] U. National Minerals Information Center, “Mineral Commodity Summaries 2016,” 2011.
- [15] M. A. Aouaj, R. Diaz, A. Belayachi, F. Rueda, and M. Abd-Lefdil, “Comparative study of

- ITO and FTO thin films grown by spray pyrolysis,” *Mater. Res. Bull.*, vol. 44, no. 7, pp. 1458–1461, 2009.
- [16] V. Nam and D. Lee, “Copper Nanowires and Their Applications for Flexible, Transparent Conducting Films: A Review,” *Nanomaterials*, vol. 6, no. 3, p. 47, Mar. 2016.
- [17] Z. Zhu *et al.*, “Sol-gel deposition and plasma treatment of intrinsic, aluminum-doped, and gallium-doped zinc oxide thin films as transparent conductive electrodes,” 2015, p. 956109.
- [18] W. Gaynor, G. F. Burkhard, M. D. McGehee, and P. Peumans, “Smooth Nanowire/Polymer Composite Transparent Electrodes,” *Adv. Mater.*, vol. 23, no. 26, pp. 2905–2910, Jul. 2011.
- [19] I. Winer, G. E. Shter, M. Mann-Lahav, and G. S. Grader, “Effect of solvents and stabilizers on sol–gel deposition of Ga-doped zinc oxide TCO films,” *J. Mater. Res.*, vol. 26, no. 10, pp. 1309–1315, May 2011.
- [20] V. Kumar, R. G. Singh, F. Singh, and L. P. Purohit, “Highly transparent and conducting boron doped zinc oxide films for window of Dye Sensitized Solar Cell applications,” *J. Alloys Compd.*, vol. 544, pp. 120–124, Dec. 2012.
- [21] I. Y. Y. Bu, “Highly conductive and transparent reduced graphene oxide/aluminium doped zinc oxide nanocomposite for the next generation solar cell applications,” *Opt. Mater. (Amst)*, vol. 36, no. 2, pp. 299–303, Dec. 2013.
- [22] S. Salam, M. Islam, and A. Akram, “Sol–gel synthesis of intrinsic and aluminum-doped zinc oxide thin films as transparent conducting oxides for thin film solar cells,” *Thin Solid Films*, vol. 529, pp. 242–247, Feb. 2013.
- [23] K. Sun, P. Li, Y. Xia, J. Chang, and J. Ouyang, “Transparent Conductive Oxide-Free Perovskite Solar Cells with PEDOT:PSS as Transparent Electrode,” *ACS Appl. Mater. Interfaces*, vol. 7, no. 28, pp. 15314–15320, Jul. 2015.
- [24] F. Jiang, T. Liu, S. Zeng, Q. Zhao, X. Min, and Z. Li, “Metal electrode – free perovskite solar cells with transfer-laminated conducting polymer electrode,” *Opt. Express*, vol. 23, no. 3, pp. 3748–3754, 2015.
- [25] L. Yin, Z. Zhao, F. Jiang, Z. Li, S. Xiong, and Y. Zhou, “PEDOT:PSS top electrode prepared by transfer lamination using plastic wrap as the transfer medium for organic solar cells,” *Org. Electron.*, vol. 15, no. 10, pp. 2593–2598, Oct. 2014.
- [26] T. Cheng, Y.-Z. Zhang, J.-D. Zhang, W.-Y. Lai, and W. Huang, “High-performance free-standing PEDOT:PSS electrodes for flexible and transparent all-solid- state supercapacitors.”
- [27] H.-B. Kim *et al.*, “Mixed solvents for the optimization of morphology in solution-processed, inverted-type perovskite/fullerene hybrid solar cells.,” *Nanoscale*, vol. 6, no. 12, pp. 6679–83, 2014.
- [28] Z. Z. Zhu *et al.*, “Sequential deposition as a route to high-performance perovskite-sensitized solar cells.,” *Energy Environ. Sci.*, vol. 7, no. 1, pp. 316–320, 2015.
- [29] L. Bu *et al.*, “Semitransparent Fully Air Processed Perovskite Solar Cells,” *ACS Appl.*

- Mater. Interfaces*, vol. 7, no. 32, pp. 17776–17781, 2015.
- [30] C. Tao *et al.*, “17.6% Stabilized Efficiency in Low-Temperature Processed Planar Perovskite Solar Cells,” *Energy Environ. Sci. Energy Environ. Sci.*, vol. 8, no. 8, pp. 2365–2370, 2015.
- [31] I. N. Kholmanov *et al.*, “Reduced Graphene Oxide/Copper Nanowire Hybrid Films as High-Performance Transparent Electrodes,” *ACS Nano*, vol. 7, no. 2, pp. 1811–1816, Feb. 2013.
- [32] H. A. Becerril, J. Mao, Z. Liu, R. M. Stoltenberg, Z. Bao, and Y. Chen, “Evaluation of Solution-Processed Reduced Graphene Oxide Films as Transparent Conductors,” *ACS Nano*, vol. 2, no. 3, pp. 463–470, Mar. 2008.
- [33] J. V van de Groep, P. Spinelli, and A. Polman, “Transparent Conducting Silver Nanowire Networks,” *Nano Lett.*, vol. 12, no. 6, pp. 3138–3144, 2012.
- [34] T. Synthesis, T. Copper, and T. C. Films, “Nanowires to Make Flexible , Transparent Conducting Films on Plastic Substrates,” 2011.
- [35] A. R. Rathmell, S. M. Bergin, Y.-L. Hua, Z.-Y. Li, and B. J. Wiley, “The growth mechanism of copper nanowires and their properties in flexible, transparent conducting films.,” *Adv. Mater.*, vol. 22, no. 32, pp. 3558–63, Aug. 2010.
- [36] S. Nam *et al.*, “Ultrasoother, extremely deformable and shape recoverable Ag nanowire embedded transparent electrode,” *Sci. Rep.*, vol. 4, pp. 4371–4375, Apr. 2014.
- [37] Yugang Sun, Brian Mayers, and Thurston Herricks, and Y. Xia\*, “Polyol Synthesis of Uniform Silver Nanowires: A Plausible Growth Mechanism and the Supporting Evidence,” 2003.
- [38] H. Guo *et al.*, “Copper nanowires as fully transparent conductive electrodes.,” *Sci. Rep.*, vol. 3, p. 2323, Jan. 2013.
- [39] D. Zhang *et al.*, “Synthesis of Ultralong Copper Nanowires for High-Performance Transparent Electrodes,” pp. 19–22, 2012.
- [40] D. M. (Solaronix), “DYE SOLAR CELLS FOR REAL The Assembly Guide for Making Your Own Solar Cells,” 2012.
- [41] G. Boschloo and A. Hagfeldt, “Characteristics of the Iodide/Triiodide Redox Mediator in Dye-Sensitized Solar Cells,” *Acc. Chem. Res.*, vol. 42, no. 11, pp. 1819–1826, Nov. 2009.
- [42] M. Grätzel, “Solar Energy Conversion by Dye-Sensitized Photovoltaic Cells,” *Inorg. Chem.*, vol. 44, no. 20, pp. 6841–6851, Oct. 2005.
- [43] B. O’Regan and M. Grätzel, “A low-cost, high-efficiency solar cell based on dye-sensitized colloidal TiO<sub>2</sub> films,” *Nature*, vol. 353, no. 6346, pp. 737–740, Oct. 1991.
- [44] H. Gerischer, M. E. Michel-Beyerle, F. Reberstrost, and H. Tributsch, “Sensitization of charge injection into semiconductors with large band gap,” *Electrochim. Acta*, vol. 13, no. 6, pp. 1509–1515, Jun. 1968.
- [45] N. R. E. L. (NREL), “Photovoltaic Research | NREL.” [Online]. Available:

- <https://www.nrel.gov/pv/>. [Accessed: 24-Apr-2017].
- [46] “Basic Research Needs for Solar Energy Utilization,” 2005.
- [47] J. Yan and B. R. Saunders, “Third-generation solar cells: a review and comparison of polymer:fullerene, hybrid polymer and perovskite solar cells,” *RSC Adv.*, vol. 4, no. 82, pp. 43286–43314, Aug. 2014.
- [48] A. B. Djurišić *et al.*, “Stability issues of the next generation solar cells,” *Phys. status solidi - Rapid Res. Lett.*, vol. 10, no. 4, pp. 281–299, Apr. 2016.
- [49] Y. Han *et al.*, “Degradation observations of encapsulated planar CH<sub>3</sub>NH<sub>3</sub>PbI<sub>3</sub> perovskite solar cells at high temperatures and humidity,” *J. Mater. Chem. A*, vol. 3, no. 15, pp. 8139–8147, 2015.
- [50] C. Liu *et al.*, “High Performance Planar Heterojunction Perovskite Solar Cells with Fullerene Derivatives as the Electron Transport Layer,” *ACS Appl. Mater. Interfaces*, vol. 7, pp. 1153–1159, 2015.
- [51] M. Yang *et al.*, “Facile fabrication of large-grain CH<sub>3</sub>NH<sub>3</sub>PbI<sub>3</sub>-xBr<sub>x</sub> films for high-efficiency solar cells via CH<sub>3</sub>NH<sub>3</sub>Br-selective Ostwald ripening,” *Nat. Commun.*, vol. 7, no. May, pp. 2–10, Aug. 2016.
- [52] F. Guo *et al.*, “High-performance semitransparent perovskite solar cells with solution-processed silver nanowires as top electrodes,” *Nanoscale*, vol. 7, pp. 1642–1649, 2015.
- [53] Y. Deng, E. Peng, Y. Shao, Z. Xiao, Q. Dong, and J. Huang, “Scalable fabrication of efficient organolead trihalide perovskite solar cells with doctor-bladed,” *Energy Environ. Sci.*, vol. 8, pp. 1544–1550, 2015.
- [54] H.-S. Ko *et al.*, “15.76% efficiency perovskite solar cells prepared under high relative humidity: importance of PbI<sub>2</sub> morphology in two-step deposition of CH<sub>3</sub>NH<sub>3</sub>PbI<sub>3</sub>,” *J. Mater. Chem. A*, vol. 3, no. 16, pp. 8808–8815, 2015.
- [55] J. S. Manser, J. A. Christians, and P. V. Kamat, “Intriguing Optoelectronic Properties of Metal Halide Perovskites,” *Chemical Reviews*. 2016.
- [56] N. J. Jeon, J. Lee, J. H. Noh, M. K. Nazeeruddin, M. Grätzel, and S. Il Seok, “Efficient inorganic-organic hybrid perovskite solar cells based on pyrene arylamine derivatives as hole-transporting materials,” *J. Am. Chem. Soc.*, vol. 135, no. 51, pp. 19087–19090, 2013.
- [57] J. Burschka *et al.*, “Sequential deposition as a route to high-performance perovskite-sensitized solar cells,” *Nature*, vol. 499, no. 7458, pp. 316–320, 2013.
- [58] Y.-J. Jeon *et al.*, “Planar heterojunction perovskite solar cells with superior reproducibility,” *Sci. Rep.*, vol. 4, p. 6953, 2014.
- [59] J. You *et al.*, “Low-temperature solution-processed perovskite solar cells with high efficiency and flexibility,” *ACS Nano*, vol. 8, no. 2, pp. 1674–80, 2014.
- [60] J. Seo *et al.*, “Benefits of very thin PCBM and LiF layers for solution-processed p-i-n perovskite solar cells,” *Energy Environ. Sci.*, vol. 7, no. 8, p. 2642, 2014.

- [61] P. Docampo, J. M. Ball, M. Darwich, G. E. Eperon, and H. J. Snaith, “Efficient organometal trihalide perovskite planar-heterojunction solar cells on flexible polymer substrates.,” *Nat. Commun.*, vol. 4, p. 2761, 2013.
- [62] Q. Wang, Y. Shao, Q. Dong, Z. Xiao, Y. Yuan, and J. Huang, “Large fill-factor bilayer iodine perovskite solar cells fabricated by a low-temperature solution-process,” *Energy Environ. Sci.*, vol. 7, no. 7, p. 2359, 2014.
- [63] R. Wu *et al.*, “Efficient electron-blocking layer-free planar heterojunction perovskite solar cells with a high open-circuit voltage,” *Org. Electron. physics, Mater. Appl.*, vol. 26, pp. 265–272, 2015.
- [64] C. Chen *et al.*, “Efficient perovskite solar cells based on low-temperature solution-processed (CH<sub>3</sub>NH<sub>3</sub>)PbI<sub>3</sub> perovskite/CuInS<sub>2</sub> planar heterojunctions.,” *Nanoscale Res. Lett.*, vol. 9, no. 1, p. 457, 2014.
- [65] Y. Zhou, M. Yang, W. Wu, A. L. Vasiliev, K. Zhu, and N. P. Padture, “Room-Temperature Crystallization of Hybrid-Perovskite Thin Films via Solvent-Solvent Extraction for High-Performance Solar Cells,” *J. Mater. Chem. A*, vol. 3, pp. 8178–8184, 2015.
- [66] D. Liu, J. Yang, and T. L. Kelly, “Compact layer free perovskite solar cells with 13.5% efficiency,” *J. Am. Chem. Soc.*, vol. 136, no. 49, pp. 17116–17122, 2014.
- [67] P. You, Z. Liu, Q. Tai, S. Liu, and F. Yan, “Efficient Semitransparent Perovskite Solar Cells with Graphene Electrodes,” *Adv. Mater.*, vol. 27, no. 24, pp. 3632–3638, 2015.
- [68] M. Ramesh, K. M. Boopathi, T. Y. Huang, Y. C. Huang, C. S. Tsao, and C. W. Chu, “Using an airbrush pen for layer-by-layer growth of continuous perovskite thin films for hybrid solar cells,” *ACS Appl. Mater. Interfaces*, vol. 7, no. 4, pp. 2359–2366, 2015.
- [69] W. Ke *et al.*, “Efficient hole-blocking layer-free planar halide perovskite thin-film solar cells,” *Nat. Commun.*, vol. 6, p. 6700, 2015.
- [70] C. D. Bailie *et al.*, “Semi-transparent perovskite solar cells for tandems with silicon and CIGS,” *Energy Environ. Sci.*, vol. 8, pp. 956–963, 2014.
- [71] Y.-J. Jeon *et al.*, “Planar heterojunction perovskite solar cells with superior reproducibility,” *Sci. Rep.*, vol. 4, p. 6953, Nov. 2014.
- [72] H. Saarenpää, T. Niemi, A. Tukiainen, H. Lemmetyinen, and N. Tkachenko, “Aluminum doped zinc oxide films grown by atomic layer deposition for organic photovoltaic devices,” *Sol. Energy Mater. Sol. Cells*, vol. 94, no. 8, pp. 1379–1383, 2010.
- [73] J.-H. Lee and B.-O. Park, “Transparent conducting ZnO:Al, In and Sn thin films deposited by the sol-gel method,” *Thin Solid Films*, vol. 426, no. 1, pp. 94–99, 2003.
- [74] M. Ohyama, H. Kozuka, and T. Yoko, “Sol-Gel Preparation of Transparent and Conductive Aluminum-Doped Zinc Oxide Films with Highly Preferential Crystal Orientation,” *J. Am. Ceram. Soc.*, vol. 81, no. 6, pp. 1622–1632, Jan. 2005.
- [75] L. Hu, H. Wu, and Y. Cui, “Metal nanogrids, nanowires, and nanofibers for transparent electrodes,” *MRS Bull.*, vol. 36, no. 10, pp. 760–765, 2011.

- [76] J. Y. Kim, J. H. Jung, D. E. Lee, and J. Joo, "Enhancement of electrical conductivity of poly(3,4-ethylenedioxythiophene)/poly(4-styrenesulfonate) by a change of solvents," *Synth. Met.*, vol. 126, no. 2, pp. 311–316, 2002.
- [77] W. Gaynor, J.-Y. Lee, and P. Peumans, "Fully Solution-Processed Inverted Polymer Solar Cells with Laminated Nanowire Electrodes," *ACS Nano*, vol. 4, no. 1, pp. 30–34, Jan. 2010.
- [78] W. Gaynor, G. F. Burkhard, M. D. McGehee, and P. Peumans, "Smooth Nanowire/Polymer Composite Transparent Electrodes," *Adv. Mater.*, vol. 23, pp. 2905–2910, 2011.
- [79] S. De *et al.*, "Silver Nanowire Networks as Flexible, Transparent, Conducting Films: Extremely High DC to Optical Conductivity Ratios," *ACS Nano*, vol. 3, no. 7, pp. 1767–1774, Jul. 2009.
- [80] T. Kawashima, T. Ezure, K. Okada, H. Matsui, K. Goto, and N. Tanabe, "FTO/ITO double-layered transparent conductive oxide for dye-sensitized solar cells," *J. Photochem. Photobiol. A Chem.*, vol. 164, no. 1, pp. 199–202, 2004.
- [81] A. R. Madaria, A. Kumar, and C. Zhou, "Large scale, highly conductive and patterned transparent films of silver nanowires on arbitrary substrates and their application in touch screens," *Nanotechnology*, vol. 22, no. 24, p. 245201, Jun. 2011.
- [82] J. Lee *et al.*, "Very long Ag nanowire synthesis and its application in a highly transparent, conductive and flexible metal electrode touch panel," *Nanoscale*, vol. 4, no. 20, p. 6408, 2012.
- [83] Y.-H. Tak, K.-B. Kim, H.-G. Park, K.-H. Lee, and J.-R. Lee, "Criteria for ITO (indium–tin-oxide) thin film as the bottom electrode of an organic light emitting diode," *Thin Solid Films*, vol. 411, no. 1, pp. 12–16, 2002.
- [84] S. Ishibashi, Y. Higuchi, Y. Ota, and K. Nakamura, "Low resistivity indium–tin oxide transparent conductive films. II. Effect of sputtering voltage on electrical property of films," *J. Vac. Sci. Technol. A Vacuum, Surfaces, Film.*, vol. 8, no. 3, pp. 1403–1406, May 1990.
- [85] T. Minami, "Transparent conducting oxide semiconductors for transparent electrodes," *Semicond. Sci. Technol.*, vol. 20, no. 4, pp. S35–S44, Apr. 2005.
- [86] W.-H. Kim, W. J. Maeng, M.-K. Kim, and H. Kim, "Low Pressure Chemical Vapor Deposition of Aluminum-Doped Zinc Oxide for Transparent Conducting Electrodes," *J. Electrochem. Soc.*, vol. 158, no. 8, p. D495, 2011.
- [87] T. Ohgaki *et al.*, "Optical Properties of Heavily Aluminum-Doped Zinc Oxide Thin Films Prepared by Molecular Beam Epitaxy," *Key Eng. Mater.*, vol. 248, pp. 91–94, 2003.
- [88] E. Fortunato *et al.*, "Highly stable transparent and conducting gallium-doped zinc oxide thin films for photovoltaic applications," *Sol. Energy Mater. Sol. Cells*, vol. 92, no. 12, pp. 1605–1610, 2008.
- [89] F.-H. Wang, C.-F. Yang, J.-C. Liou, and I.-C. Chen, "Effects of Hydrogen on the Optical and Electrical Characteristics of the Sputter-Deposited Al<sub>2</sub>O<sub>3</sub>-Doped ZnO Thin Films," *J. Nanomater.*, vol. 2014, pp. 1–7, 2014.

- [90] S. H. Lee, T. S. Lee, K. S. Lee, B. Cheong, Y. D. Kim, and W. M. Kim, "Characteristics of hydrogen co-doped ZnO : Al thin films," *J. Phys. D. Appl. Phys.*, vol. 41, no. 9, p. 95303, May 2008.
- [91] X. Yan, S. Venkataraj, and A. G. Aberle, "Modified Surface Texturing of Aluminium-Doped Zinc Oxide (AZO) Transparent Conductive Oxides for Thin-Film Silicon Solar Cells," *Energy Procedia*, vol. 33, pp. 157–165, 2013.
- [92] J. Liu *et al.*, "Investigation of aluminum–gallium co-doped zinc oxide targets for sputtering thin film and photovoltaic application," *J. Alloys Compd.*, vol. 575, pp. 174–182, 2013.
- [93] P. . Song, M. Watanabe, M. Kon, A. Mitsui, and Y. Shigesato, "Electrical and optical properties of gallium-doped zinc oxide films deposited by dc magnetron sputtering," *Thin Solid Films*, vol. 411, no. 1, pp. 82–86, 2002.
- [94] M.-C. Jun, S.-U. Park, and J.-H. Koh, "Comparative studies of Al-doped ZnO and Ga-doped ZnO transparent conducting oxide thin films."
- [95] Y. Hou and A. H. Jayatissa, "Low resistive gallium doped nanocrystalline zinc oxide for gas sensor application via sol–gel process," *Sensors Actuators B Chem.*, vol. 204, pp. 310–318, 2014.
- [96] Q. Li, X. Li, and J. Zhang, "Microstructure, optical and electrical properties of gallium-doped ZnO films prepared by sol–gel method," *J. Alloys Compd.*, vol. 572, pp. 175–179, 2013.
- [97] C.-Y. Tsay, K.-S. Fan, and C.-M. Lei, "Synthesis and characterization of sol–gel derived gallium-doped zinc oxide thin films," *J. Alloys Compd.*, vol. 512, no. 1, pp. 216–222, 2012.
- [98] W. M. Tsang, F. L. Wong, M. K. Fung, J. C. Chang, C. S. Lee, and S. T. Lee, "Transparent conducting aluminum-doped zinc oxide thin film prepared by sol–gel process followed by laser irradiation treatment," *Thin Solid Films*, vol. 517, no. 2, pp. 891–895, 2008.
- [99] S. Salam, M. Islam, and A. Akram, "Sol–gel synthesis of intrinsic and aluminum-doped zinc oxide thin films as transparent conducting oxides for thin film solar cells," *Thin Solid Films*, vol. 529, pp. 242–247, 2013.
- [100] H. Chen, Y. H. Jeony, and C.-B. Park, "Enhancement of Electrical Properties on ZnO: Al Thin Film due to Hydrogen Annealing and SiO<sub>2</sub> Coating in Damp-heat Environment," *Trans. Electr. Electron. Mater.*, vol. 10, no. 2, pp. 59–61, 2009.
- [101] M. A. Yaklin, D. A. Schneider, K. Norman, J. E. Granata, and C. L. Staiger, "Impacts of Humidity and Temperature on the Performance of Transparent Conducting Zinc Oxide," in *2010 35th IEEE Photovoltaic Specialists Conference*, 2010, pp. 002493–002496.
- [102] Z. Zhu *et al.*, "Sol-gel deposition and plasma treatment of intrinsic, aluminum-doped, and gallium-doped zinc oxide thin films as transparent conductive electrodes," 2015, p. 956109.
- [103] W. Fu, L. Liu, K. Jiang, Q. Li, and S. Fan, "Super-aligned carbon nanotube films as aligning layers and transparent electrodes for liquid crystal displays," *Carbon N. Y.*, vol. 48, no. 7, pp. 1876–1879, 2010.

- [104] B.-Y. Oh, W.-K. Lee, Y.-H. Kim, and D.-S. Seo, "Zinc oxide nanolevel surface transformation for liquid crystal orientation by ion bombardment," *J. Appl. Phys.*, vol. 105, no. 5, p. 54506, Mar. 2009.
- [105] Z. Wu *et al.*, "Transparent, Conductive Carbon Nanotube Films," *Science (80-. )*, vol. 305, no. 5688, pp. 1273–1276, Aug. 2004.
- [106] X. Wang, L. Zhi, and K. Müllen, "Transparent, Conductive Graphene Electrodes for Dye-Sensitized Solar Cells," *Nano Lett.*, vol. 8, no. 1, pp. 323–327, Jan. 2008.
- [107] A. Du Pasquier, H. Emrah Unalan, A. Kanwal, S. Miller, and M. Chhowalla, "Conducting and transparent single-wall carbon nanotube electrodes for polymer-fullerene solar cells," 2005.
- [108] J.-Y. Lee, S. T. Connor, Y. Cui, and P. Peumans, "Solution-Processed Metal Nanowire Mesh Transparent Electrodes," *Nano Lett.*, vol. 8, no. 2, pp. 689–692, 2008.
- [109] M. W. Rowell *et al.*, "Organic solar cells with carbon nanotube network electrodes," *Appl. Phys. Lett.*, vol. 88, no. 23, p. 233506, Jun. 2006.
- [110] T. Minami, "Present status of transparent conducting oxide thin-film development for Indium-Tin-Oxide (ITO) substitutes," *Thin Solid Films*, vol. 516, no. 17, pp. 5822–5828, 2008.
- [111] S. De *et al.*, "Silver Nanowire Networks as Flexible, Transparent, Conducting Films: Extremely High DC to Optical Conductivity Ratios," *ACS Nano*, vol. 3, no. 7, pp. 1767–1774, Jul. 2009.
- [112] M.-G. Kang, H. Joon Park, S. Hyun Ahn, and L. Jay Guo, "Transparent Cu nanowire mesh electrode on flexible substrates fabricated by transfer printing and its application in organic solar cells," 2010.
- [113] J.-H. Lee, K.-H. Ko, and B.-O. Park, "Electrical and optical properties of ZnO transparent conducting films by the sol–gel method," *J. Cryst. Growth*, vol. 247, no. 1, pp. 119–125, 2003.
- [114] C. Wang, J. Li, and J. Dho, "Post-deposition annealing effects on the transparent conducting properties of anatase Nb:TiO<sub>2</sub> films on glass substrates," 2014.
- [115] J. Nelson, *The Physics of Solar Cells*. World Scientific Publishing Company, 2003.
- [116] D. Kuang *et al.*, "Application of Highly Ordered TiO<sub>2</sub> Nanotube Arrays in Flexible Dye-Sensitized Solar Cells," *ACS Nano*, vol. 2, no. 6, pp. 1113–1116, 2008.
- [117] L.-C. Chen, J.-C. Chen, C.-C. Chen, and C.-G. Wu, "Fabrication and Properties of High-Efficiency Perovskite/PCBM Organic Solar Cells.," *Nanoscale Res. Lett.*, vol. 10, no. 1, p. 1020, 2015.
- [118] A. Katoch, H. Kim, T. Hwang, and S. S. Kim, "Preparation of highly stable TiO<sub>2</sub> sols and nanocrystalline TiO<sub>2</sub> films via a low temperature sol–gel route," *J. Sol-Gel Sci. Technol.*, vol. 61, no. 1, pp. 77–82, Jan. 2012.
- [119] H. Kim and T. Hwang, "Effect of titanium isopropoxide addition in low-temperature cured

- TiO<sub>2</sub> photoanode for a flexible DSSC,” *J. Sol-Gel Sci. Technol.*, vol. 72, no. 1, pp. 67–73, 2014.
- [120] J. H. Heo, H. J. Han, D. Kim, T. K. Ahn, and S. H. Im, “Hysteresis-less inverted CH<sub>3</sub>NH<sub>3</sub>PbI<sub>3</sub> planar perovskite hybrid solar cells with 18.1% power conversion efficiency,” *Energy Environ. Sci.*, vol. 8, no. 5, pp. 1602–1608, 2015.
- [121] Z. Zekry and G. Eldallal, “Effect of MS contact on the electrical behaviour of solar cells,” *Solid. State. Electron.*, vol. 31, no. 1, pp. 91–97, Jan. 1988.
- [122] “Guide To Interpreting I-V Curve Measurements of PV Arrays,” 2011.
- [123] B. Susrutha, L. Giribabu, and S. P. Singh, “Recent advances in flexible perovskite solar cells,” *Chem. Commun.*, vol. 51, no. 79, pp. 14696–14707, 2015.
- [124] A. Wakamiya *et al.*, “X-ray Crystallographical Studies on Reproducible Fabrication of Efficient Perovskite Solar Cells,” *Gd. Renew. Energy Conf.*, pp. 9–10, 2014.
- [125] D. B. Mitzi, C. A. Feild, Z. Schlesinger, and R. B. Laibowitz, “Transport, Optical, and Magnetic Properties of the Conducting Halide Perovskite CH<sub>3</sub>NH<sub>3</sub>SnI<sub>3</sub>,” *J. Solid State Chem.*, vol. 114, no. 1, pp. 159–163, Jan. 1995.
- [126] K. M. Boopathi *et al.*, “Preparation of metal halide perovskite solar cells through a liquid droplet assisted method,” *J. Mater. Chem. A*, vol. 3, pp. 9257–9263, 2015.
- [127] Z. Zhu *et al.*, “High-performance hole-extraction layer of sol-gel-processed niO nanocrystals for inverted planar perovskite solar cells,” *Angew. Chemie - Int. Ed.*, vol. 53, no. 46, pp. 12571–12575, 2014.
- [128] T. Song *et al.*, “Perovskite solar cells: film formation and properties,” *J. Mater. Chem. A*, vol. 3, no. 17, pp. 9032–9050, 2015.
- [129] H.-S. Kim *et al.*, “Lead iodide perovskite sensitized all-solid-state submicron thin film mesoscopic solar cell with efficiency exceeding 9%,” *Sci. Rep.*, vol. 2, p. 591, 2012.
- [130] S. Bai *et al.*, “High-performance planar heterojunction perovskite solar cells: Preserving long charge carrier diffusion lengths and interfacial engineering,” *Nano Res.*, vol. 7, no. 12, pp. 1749–1758, 2014.
- [131] S. Gamliel and L. Etgar, “Organo-metal perovskite based solar cells: sensitized versus planar architecture.”
- [132] A. D. Sheikh *et al.*, “Atmospheric effects on the photovoltaic performance of hybrid perovskite solar cells,” 2015.
- [133] B. Conings *et al.*, “An easy-to-fabricate low-temperature TiO<sub>2</sub> electron collection layer for high efficiency planar heterojunction perovskite solar cells,” *APL Mater.*, vol. 2, no. 8, p. 81505, Aug. 2014.
- [134] K.-W. Tsai, C.-C. Chueh, S. T. Williams, T.-C. Wen, and A. K. Y. Jen, “High-performance hole-transporting layer-free conventional perovskite/fullerene heterojunction thin-film solar cells,” *J. Mater. Chem. A*, vol. 3, no. 17, pp. 9128–9132, 2015.

- [135] G. S. Selopal, R. Milan, I. Concina, G. Sberveglieri, and A. Vomiero, “Effect of Blocking Layer to Boost Photoconversion Efficiency in ZnO Dye-Sensitized Solar Cells,” 2014.
- [136] I. Y. Y. Bu and M. T. Cole, “One-pot synthesis of intercalating ZnO nanoparticles for enhanced dye-sensitized solar cells,” *Mater. Lett.*, vol. 90, pp. 56–59, 2013.
- [137] D. Y. Liu and T. L. Kelly, “Perovskite solar cells with a planar heterojunction structure prepared using room-temperature solution processing techniques,” *Nat. Photonics*, vol. 8, no. 2, pp. 133–138, 2014.
- [138] Y. Zhao *et al.*, “Rapid and large-scale synthesis of Cu nanowires via a continuous flow solvothermal process and its application in dye-sensitized solar cells (DSSCs),” *RSC Adv.*, vol. 2, no. 30, p. 11544, 2012.
- [139] K. M. Lee, C. W. Hu, H. W. Chen, and K. C. Ho, “Incorporating carbon nanotube in a low-temperature fabrication process for dye-sensitized TiO<sub>2</sub> solar cells,” *Sol. Energy Mater. Sol. Cells*, vol. 92, no. 12, pp. 1628–1633, 2008.
- [140] J. Zhu *et al.*, “Film Fabricated At Room Temperature and Its Acoustic Properties,” *J. Phys. D. Appl. Phys.*, vol. 41, no. 16, p. 162001, 2008.
- [141] Y. Wang *et al.*, “Preparation of porous nanoparticle TiO<sub>2</sub> films for flexible dye-sensitized solar cells,” *Chinese Sci. Bull.*, vol. 56, no. 24, pp. 2649–2653, 2011.
- [142] J. Huang *et al.*, “Highly Transparent and Flexible Nanopaper Transistors,” *ACS Nano*, no. Xx, 2013.
- [143] M. Hershcovitz and I. E. Klein, “Dynamics of spin coating on very rough surfaces,” *Microelectron. Reliab.*, vol. 33, no. 6, pp. 869–880, May 1993.
- [144] S. Y. Qi *et al.*, “Showcasing the influences of pinholes in hole transport layers on the stability of perovskite solar cells by Prof. Yabing Qi at the Pinhole-free hole transport layers significantly improve the stability of MAPbI<sub>3</sub>-based perovskite solar cells under opera.”
- [145] C. Roldán-Carmona *et al.*, “High efficiency single-junction semitransparent perovskite solar cells,” *Energy Environ. Sci.*, vol. 7, no. 9, p. 2968, Jul. 2014.
- [146] G. E. Eperon, V. M. Burlakov, A. Goriely, and H. J. Snaith, “Neutral Color Semitransparent Microstructured Perovskite Solar Cells,” *ACS Nano*, vol. 8, no. 1, pp. 591–598, Jan. 2014.
- [147] Z. Li *et al.*, “Laminated Carbon Nanotube Networks for Metal Electrode-Free Efficient Perovskite Solar Cells,” *ACS Nano*, vol. 8, no. 7, pp. 6797–6804, Jul. 2014.
- [148] T. J. Coutts, K. A. Emery, and J. Scott Ward, “Modeled performance of polycrystalline thin-film tandem solar cells,” *Prog. Photovoltaics Res. Appl.*, vol. 10, no. 3, pp. 195–203, May 2002.
- [149] “Corrosion Resistance Common Metals.” [Online]. Available: [http://www.roytech.co.uk/Useful\\_Tables/Corrosion/Corr\\_metals\\_1.html](http://www.roytech.co.uk/Useful_Tables/Corrosion/Corr_metals_1.html). [Accessed: 11-Apr-2017].
- [150] A. R. Rathmell, M. Nguyen, M. Chi, and B. J. Wiley, “Synthesis of oxidation-resistant cupronickel nanowires for transparent conducting nanowire networks,” *Nano Lett.*, vol. 12,

no. 6, pp. 3193–3199, 2012.

- [151] W. Zhang *et al.*, “Ultrasmooth organic-inorganic perovskite thin-film formation and crystallization for efficient planar heterojunction solar cells,” *Nat Commun*, vol. 6, p. 6142, 2015.
- [152] H. Park, W.-R. Kim, H.-T. Jeong, J.-J. Lee, H.-G. Kim, and W.-Y. Choi, “Fabrication of dye-sensitized solar cells by transplanting highly ordered TiO<sub>2</sub> nanotube arrays,” *Sol. Energy Mater. Sol. Cells*, vol. 95, no. 1, pp. 184–189, 2011.
- [153] J. T. Wang *et al.*, “Low-Temperature Processed Electron Collection Layers of Graphene/TiO<sub>2</sub> Nanocomposites in Thin Film Perovskite Solar Cells,” 2014.